Experimental Investigation into Localized Instabilities of Mixed Rayleigh-Bénard-Poiseuille Convection

THÈSE N°4144 (2008)

PRÉSENTÉE LE 24 JUILLET 2008

À LA FACULTE SCIENCES ET TECHNIQUES DE L'INGÉNIEUR
LABORATOIRE DE MÉCANIQUE DES FLUIDES
PROGRAMME DOCTORAL EN MÉCANIQUE

ÉCOLE POLYTECHNIQUE FÉDÉRALE DE LAUSANNE

POUR L'OBTENTION DU GRADE DE DOCTEUR ÈS SCIENCES

PAR

Emeric GRANDJEAN

ingénieur physicien diplômé EPF
de nationalité suisse et originaire de Juriens (VD)

acceptée sur proposition du jury:

Prof. C. Ancey, président du jury
Prof. P. Monkewitz, directeur de thèse
Prof. Ph. Carrière, rapporteur
Prof. P. Huerre, rapporteur
Dr Ph. Metzener, rapporteur

ÉCOLE POLYTECHNIQUE
FÉDÉRALE DE LAUSANNE

Suisse
2008

Remerciements

Je voudrais d'abord remercier mon directeur de thèse, Peter Monkewitz, pour m'avoir offert l'opportunité d'effectuer un doctorat au LMF. Son aide et son soutient ainsi que ses réponses à mes questions m'ont permis de venir à bout de ce travail. Je souhaiterais aussi remercier Navid Borhani pour l'aide qu'il m'a apportée ainsi que pour tout ce que j'ai pu apprendre à son contact. Je tiens également à exprimer ma gratitude aux membres du jury, Patrick Huerre, Philippe Carrière, Philippe Metzener et Christophe Ancey pour leurs remarques et leurs suggestions sur mon travail et sur mon manuscrit.

Ce travail de thèse n'aurait pas été possible sans l'aide et l'expertise de Trong–Vien Truong. Ses conseils avisés et sa faculté à toujours pouvoir sortir d'une armoire l'appareil dont j'avais besoins ont été d'un très grand secours à de nombreuses occasions. Un grand merci aussi à toute l'équipe de l'atelier et particulièrement à Bernard Savary et Marc Salle pour leur professionnalisme et leur patience à mon égard. Je tiens aussi à remercier Eva Gasser pour sa gentillesse et son soutient moral.

Mon travail n'aurait probablement pas abouti sans le soutient indéfectible de mes collègues, David et Chris d'abord puis Richard, Etienne, Flavio, Roland, Marc–Antoine, Benoit et Orestis avec qui j'ai partagé bon nombre de pauses plus ou moins longues à refaire le monde. Je souhaite aussi remercier tout particulièrement mon collègue de bureau, Radboud Nelissen qui a supporté mes crises de mauvaise humeur pendant quatre ans. Nos discussions endiablées ainsi que les parties de basket vont me manquer. Tu auras ta revanche quand je te verserai tes 49% !

Je souhaite remercier mes parents dont les encouragements, la confiance et le soutien m'ont permis de mener à bien cette grande aventure, merci Maman, merci Papa !

Plein d'autre gens méritent des remerciements, que ce soit des amis de l'école ou d'ailleurs; les nommer tous serait impossible mais qu'ils soient persuadés que je les remercierai personnellement tous un jour...

Abstract

An experimental study of the stability of the Rayleigh–Bénard–Poiseuille flow was performed in a large transverse aspect ratio channel. The onset for the transverse thermo-convective rolls was determined as a function of the Reynolds number for two different fluids (water: $\mathrm{Pr} = 6.5$ and mineral oil: $\mathrm{Pr} = 450$). Then, the system impulse response was studied and a good agreement with theory was found for the convective/absolute instability transition. Finally the response of the system to localized heating was observed and compared with analytical and numerical results by Martinand, Carrière and Monkewitz (2004 & 2006): experimental thermo-convective global modes are found to correspond to the saturated "steep" variety constructed by Pier, Huerre and Chomaz (2001).

Keywords: Rayleigh–Bénard–Poiseuille, thermal convection, absolute/convective instability, global mode, Schlieren.

Résumé

Une étude expérimentale sur la stabilité de l'écoulement de Rayleigh–Bénard–Poiseuille a été entreprise dans un canal possédant un grand rapport d'aspect transverse. Le démarrage des rouleaux thermo-convectifs d'orientation transversale a été déterminé en fonction du nombre de Reynolds pour deux fluides différents (de l'eau: $Pr = 6.5$ et de l'huile minérale: $Pr = 450$). Ensuite, la réponse impulsionnelle du système a été étudiée et présente un bon accord avec la transition entre les instabilités convectives et absolues. Enfin, la réponse du système à un chauffage localisé a été observée et comparée aux résultats analytiques et numériques obtenus par Martinand, Carrière et Monkewitz (2004 & 2006) : les structures thermo-convectives observées expérimentalement correspondent bien au mode global dit "raide" construit par Pier, Huerre et Chomaz (2001).

Mots clés: Rayleigh–Bénard–Poiseuille, convection thermique, instabilité convective/absolue, mode global, Schlieren.

Contents

List of Figures

Chapter 1

Introduction

The present experimental study of the Rayleigh–Bénard–Poiseuille convection has been carried out in a large transverse aspect ratio channel. Two working fluids have been used: white mineral oil (Pr of 450) and water (Pr of 6.5). This work consists firstly of the detection of the transverse rolls stability boundary for the convective/absolute transition and of a survey of the impulse response of the system. Secondly, a study of some slow varying heating effects is presented. These points will also be compared with previous analytical and numerical work on global modes by Carrière and Monkewitz [9] and Martinand *et al.* [36] and [37] in order to check the appearance of steep global mode (see Pier *et al.* [53]).

1.1 Thermal convection

Thermal convection is a common phenomenon that can be observed in everyday life, for example in a pot or in a frying pan on the stove, above a heater. It is also present in the mantle of stars and of certain planets like the earth. Thermal convection is a heat transport through diffusion and advection in a fluid. It can be separated into natural and forced convection:

- Natural convection, where a fluid heated by a source becomes less dense and moves thanks to gravity. The surrounding, colder fluid then moves to replace it. This colder fluid is then heated and the process becomes continuous, forming a convection current. The driving force for natural convection is buoyancy, a result of differences in fluid density when gravity or another body force is present.

- Forced convection, by contrast, occurs when pumps, fans or other means are used to move the fluid and create an artificially induced convection current.

In the base state (i.e. without thermo-convective flow phenomenons), heat transport occurs only through pure conduction (electrons diffusion or phonons propagation). Radiation or phase changes will not be considered in the following study and will be neglected in the experimental measurements.

In spite of several previously documented observations, the first systematic investigation of convective patterns is due to Henri Bénard published in two papers in 1900 [2] and in 1901 [3]. His experimental setup was composed of a thin (1 mm thick) whale oil layer heated from below by steam while the upper free surface was cooled by the atmosphere. Despite the lack of precision, he observed a steady regular pattern of hexagonal cells using aluminum and graphite powder (see figure 1.1). He also observed a local depression in the center of each cell. This thermo-convective instability was in fact mainly due to the Marangoni[1] convection. This effect had been modeled 50 years later by Pearson [51] and reproduced experimentally by Block [6].

[1]The Marangoni convection is due to small temperature variation on the free surface causing surface tension gradients that are responsible for the convection in this particular case.

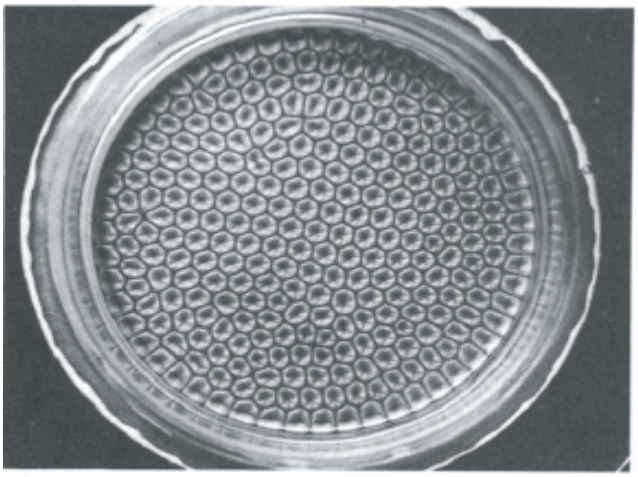

Figure 1.1: Experimental visualization of Bénard cells by Koschmieder *et al.* [31]

The first theoretical study of convection had been done by Lord Rayleigh (John William Strutt, 3rd Baron Rayleigh) in 1916. He attempted to explain Bénard's experiment through linear theory [56]. Although his work was inspired by the experiment of Bénard with buoyancy effects alone, it did not correspond to his experiments but to density driven convection. Using the Boussinesq approximation [7] (all fluid properties except density are assumed to be temperature independent) and neglecting nonlinear terms from the equation of motion and from the thermal equation, he laid down the basis of what we call today the Rayleigh–Bénard (RB) convection. The critical values characterizing the onset of this phenomenon were eventually calculated by Jeffreys ([26] and [27]). A full linear analysis can be found in the second chapter of the book by Chandrasekhar [12]. Modifications brought to the system by non-Boussinesq fluids will be described later.

1.2 Rayleigh–Bénard convection

Rayleigh–Bénard (RB) flow is the manifestation of convective structures appearing in a closed fluid layer heated from below and subject to gravity. These flow structures occur as soon as the temperature induced density differences are large enough for the pressure and the buoyancy forces to produce a flow strong enough to overcome the viscous forces and to move fluid before the heat diffusion can significantly reduce the density differences. One speaks then of an unstable state: any perturbation of infinitesimal strength will suffice to trigger the appearance of the convective flow. The present study will be restricted to classical RB flows of Newtonian fluids between horizontal, impermeable, and perfectly[2] conducting boundaries. Other cases such as with porous boundaries, unstable Poiseuille flows or other internal forces than gravity (Magneto-Hydro-Dynamic (MHD) for example) into play will not be considered into the following work.

Natural convection will only appear when viscous (tend to break fluid velocity) and thermal (tend to diffuse heat) dissipative deadening forces become smaller than the temperature dependant buoyancy forces. Convection, which is more effective than conduction in liquids, will then be initiated in the experiment by the "always present" real-life perturbations in conjunction with a big enough temperature gradient.

[2]The assumption of perfectly conducting boundaries can not be strictly observed in physical systems.

Given a sufficiently large temperature gradient oriented in the direction opposed to the gravity, some of the less dense fluid near the bottom surface experiences an upwards vertical movement. The continuity equation requires that this upward motion is compensated by a downwards motion elsewhere. The result is the formation of convection "cells" where the colder fluid is continuously replaced by the hotter fluid from the bottom. As shown qualitatively in figure 1.2, two adjacent convection cells are preferentially counter rotating.

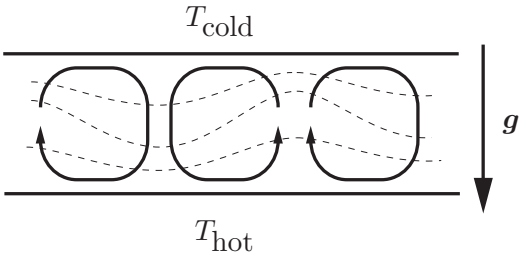

Figure 1.2: Simplified two-dimensional convective flow structures between horizontal plates [35]. The dashed lines are expected isothermal lines; they would have been strictly horizontal for a pure conductive case.

The competition between forces acting in convection is described by a dimensionless number called the Rayleigh number Ra. It is a non-dimensional measure of the vertical temperature difference applied to the fluid layer, defined by:

$$\mathrm{Ra} = \frac{g\beta(T_{\text{hot}} - T_{\text{cold}})d^3}{\nu\alpha} \tag{1.1}$$

where g is the gravitational acceleration, T_{hot} and T_{cold} are respectively the lower (hot) surface and the upper (cold) surface temperature inside the channel, d is the channel height, ν is the kinematic viscosity, and α is the thermal diffusivity defined using the thermal conductivity κ, the density ρ and the specific heat at constant pressure c_{p}:

$$\alpha \equiv \frac{\kappa}{\rho c_{\text{p}}}; \tag{1.2}$$

β is the volumetric thermal expansion:

$$\beta \equiv \frac{1}{V}\left(\frac{\partial V}{\partial T}\right)_p \tag{1.3}$$

$$= -\frac{1}{\rho}\left(\frac{\partial \rho}{\partial T}\right)_p, \tag{1.4}$$

defined at constant pressure for both the volume (V) and density (ρ) formulation.

According to Rayleigh's work, for a two dimensional case, heat transfer appears under the form of pure conduction for Ra smaller than the critical Rayleigh number Ra_{c}. When Ra_{c} value is reached, the system becomes unstable (the linearized behavior is described in section 1.5.1) and evolves to another state where convection becomes the main effect responsible for heat transfer. At this particular Ra value, the convective pattern appears with the most amplified wavenumber[3] a_{c}. The value of Ra_{c} is strongly dependent on the kind of horizontal boundaries enclosing the system; some values are presented in table 1.1 computed by Rayleigh [56] and Low [32].

[3]The wavenumber is defined as $a \equiv 2\pi/\gamma$ where γ is the wavelength of the considered wave.

Boundaries	$\mathrm{Ra_c}$	a_c
rigid-rigid	1707.8	3.117
rigid-free	1100.7	2.682
free-free	657.5	2.221

Table 1.1: Critical parameters in the pure RB system: $\mathrm{Ra_c}$ is the critical Rayleigh number, while a_c is the corresponding critical wavenumber. A rigid boundary is also considered impermeable and perfectly heat conducting.

For this first instability, i.e. for the first thermo-convective structures observed just above $\mathrm{Ra_c}$ the wavenumber is a compromise between viscous dissipation (stabilizing effect) and release of potential energy (destabilizing effect). Large wavenumber structures would dissipate a large amount of energy while small wavenumber structures would move fluid particles over long horizontal distances and would therefore not be efficient enough to release the potential energy from the hot to the cold surfaces. At the thermo-convective onset, the linear stability curve possesses a minimum corresponding to the experimentally observed wave length; however, poor conducting horizontal boundaries can be used to change this value, especially for fluid of high thermal diffusivity when the importance of temperature waves into the boundaries becomes more important: see the works by Chapman *et al.* [14], by Busse and Riahi [8] and by Hurle *et al.* [22].

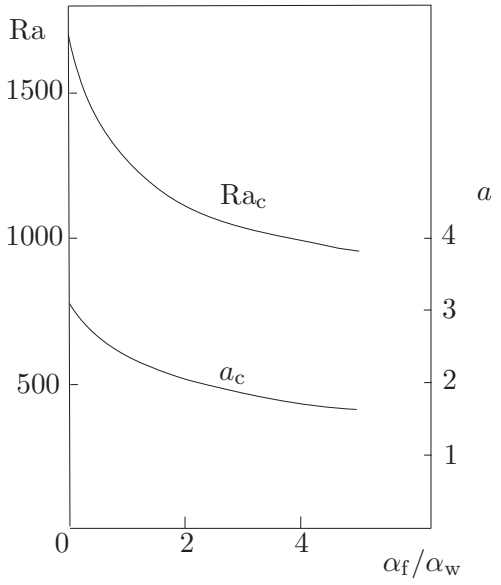

Figure 1.3: Dependence of $\mathrm{Ra_c}$ and $a_\mathrm{c}$versus the ratio between the thermal diffusivity α of the working fluid α_f and the one of the windows α_w (reproduced from [22]). The experimental value for $\alpha_\mathrm{f}/\alpha_\mathrm{w}$ in the following experiments is about 0.12 for oil and 0.21 for water

According to the work by Davis [16], under the Boussinesq approximation, the first instability observed in a rectangular box is always parallel rolls, which axis is oriented along to the shortest boundary of the box. But depending which symmetries are effectively respected, many other states can be observed in 3-D RB flow. For example, if the vertical symmetry is broken by the failure of the Boussinesq assumption (e.g. large viscosity variations with temperature) or in the surface tension driven flow (Rayleigh–Marangoni), hexagonal cells can be observed as presented in figure 1.4(a). Enok Palm [50] presented a theoretical explanation in 1960 for this experimental

observation: due to the variation of viscosity with temperature, a second-order term becomes non-zero in the system equations and destabilizes selected waves that will become dominant to form a stable cells pattern.

According to linear theory [30] depending on the symmetries, any pattern has to be a solution of a particular two-dimensional wave equation called the "membrane equation":

$$\nabla^2 e^{\mathrm{i}(a_x x + a_y y)} + \left(a_x^2 + a_y^2\right) e^{\mathrm{i}(a_x x + a_y y)} = 0, \tag{1.5}$$

where ∇^2 is the two-dimensional Laplace operator and a_x and a_y are the wavenumbers in both horizontal $\mathbf{e}_x$ and $\mathbf{e}_y$ directions respectively.

Theoretical solutions are among others: parallel rolls, equilateral triangular cells, rectangular cells of any ratio and hexagonal cells. Numerical simulations of several patterns can be found in [20]. Several experimental patterns have also been observed in-situ, see figure 1.4 where case (a) is a zero flow case (pure RB) while cases (b) and (c) are taken from Rayleigh–Bénard–Poiseuille flows.

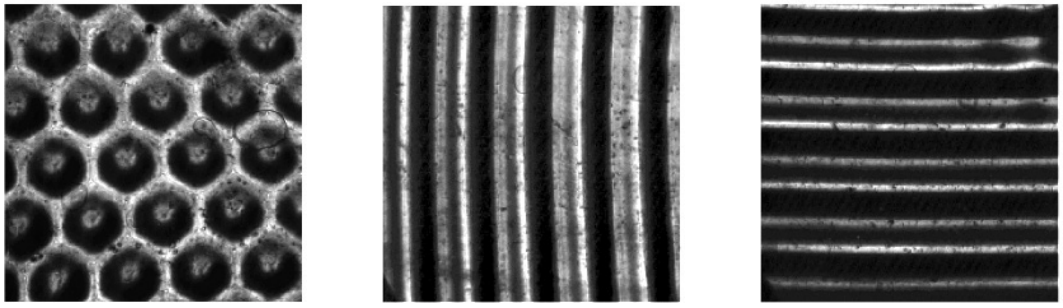

(a) (b) (c)

Figure 1.4: Fundamental modes observed in the actual channel: (a) Hexagonal cells mode, (b) transverse mode and (c) longitudinal mode. For the cases (b) and (c), the Poiseuille flow direction is from left to right.

The hexagonal cells shown in figure 1.4(a) have only been observed in a fluid with a large viscosity variation with temperature. Viscosity variation effects have been studied by Stengel *et al.* [63]: results for $\mathrm{Ra_c}$ and a_c are presented in figure (1.5). The viscosity variation in our channel is sufficient to break the symmetry and induce cells regime.

Rolls are a particular case because they exhibit a preferred direction as presented in the following section. These rolls are observed when non-symmetry boundaries force their direction or when the system symmetry is broken through for example the addition of forced convection (e.g. Poiseuille flow).

1.3 Rayleigh–Bénard–Poiseuille convection

The Rayleigh–Bénard–Poiseuille (RBP) system is an open Rayleigh–Bénard system composed of a laminar fluid flow enclosed between two horizontal surfaces where the top one is colder than the bottom one (see figure 1.6). As in the pure RB case, when the fluid in contact with the lower surface becomes hot enough, buoyancy forces win over viscous forces and thermal convection appears. Its pattern depends on the temperature gradient, on the flow rate due to forced convection, on external noise and on flow history: if a system was already in a convective state, the past pattern will have an influence on the future one. The application of a Poiseuille

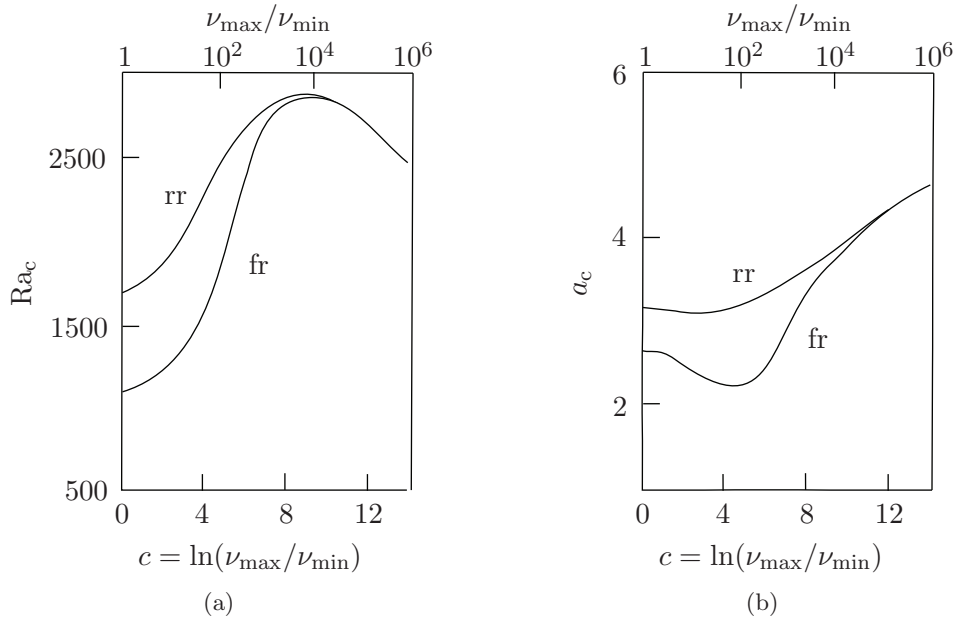

Figure 1.5: Critical Rayleigh number $\mathrm{Ra_c}$ and critical wavenumber $a_c$versus viscosity range inside the system. "rr" stands for rigid/rigid boundaries while "fr" stands for free/rigid boundaries. Even if the viscosity variations present in the actual channel are very small (~ 2), they are sufficient to break the vertical symmetry and induce the appearance of thermo-convective cells.

flow between the top and bottom plates suppresses the isotropy existing in the pure RB case; and the system behavior becomes more complicated. Two principal convective modes can be observed (figure 1.6):

- Longitudinal rolls called $\mathrm{R}_{\parallel}$: this convective pattern is composed of helicoidal thermo-convective rolls, which axis is parallel to the flow direction. They arrange themselves into a stationary chain of counter-rotating rolls (figure 1.4(c)), with all three velocity components being non-zero. They always appear in a convective mode in RBP. The Poiseuille homogeneity along the rolls axis imposes the same stability as for pure RB; but with a helicoidal trajectory for the fluid instead of a closed loop.

- Transverse rolls called $\mathrm{R}_{\perp}$: these rolls have their axis perpendicular to the flow direction and they also appear under the form of a chain of multiple counter-rotating rolls moved by the mean flow (figure 1.4(b)). These rolls are mainly two-dimensional structures without a transverse ($\mathbf{e}_y$) velocity, except close to the lateral edges. In a RBP system, depending on flow rate (i.e. Re defined later) and Ra, they can appear as a convective or as an absolute instability, see figure 1.9. The finite transverse aspect ratio ($\mathcal{R}_{\perp}$) also plays an important role on the mode observed in real channel (dependency presented in figure 1.10).

Experimental and theoretical studies have also shown more complex modes like modes superposition, periodic structures or oblique rolls. For example, wavy longitudinal rolls have been observed by Clever and Busse (1991) [15].

Rayleigh–Bénard–Poiseuille flow is the result of the superposition of forced (or advective) convection (i.e. Poiseuille flow) and a natural (or free) convection (thermal convection). One can encounter RBP flow in atmosphere where the forced convection is not strictly speaking

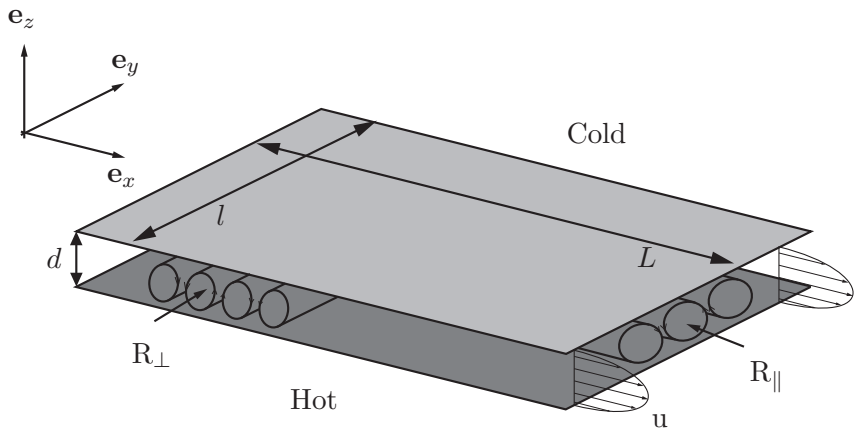

Figure 1.6: RBP schematic: a Poiseuille flow ($\mathbf{e}_x$ direction) is enclosed between two horizontal surfaces. Rolls structures with their axis parallel to the Poiseuille ($\mathbf{e}_x$) flow direction are called $\mathrm{R}_\parallel$ while rolls which axis are perpendicular to the Poiseuille flow direction are called $\mathrm{R}_\perp$

a Poiseuille flow; but as the atmosphere boundary conditions are difficult to reproduce in a laboratory, we will limit further studies to pure Poiseuille flow combined with free convection.

The numerous kinds of convective structures are mainly controlled by three dimensionless parameters based on the channel and on the thermo-physical properties of the fluid, besides the Rayleigh number Ra, one needs the Reynolds number Re and the Prandtl number Pr:

The Reynolds number Re The Reynolds number Re is based on the maximum Poiseuille flow velocity (we always assume a stationary, fully developed, Poiseuille flow for the velocity profile calculation based on the volumetric flow rate.)

$$\mathrm{Re} = \frac{U_{\max} d}{\nu} \tag{1.6}$$

where $U_{\max}$ is the maximal Poiseuille flow velocity, d the height of the channel and ν is the kinematic viscosity of the fluid.

The Prandtl number Pr The Prandtl number Pr is the ratio of viscous to thermal diffusion rate. It represents the competition between the evolution of the temperature profile and the velocity profile. Liquid metals have a Prandtl number smaller than one, so that the temperature boundary layer becomes fully developed before the velocity boundary layer. However, in mineral oil the Prandtl number Pr is very large which means that the flow velocity is established before the temperature one.

$$\mathrm{Pr} = \frac{\nu}{\alpha} \tag{1.7}$$

with α the thermal diffusivity.

Additional dimensionless numbers Other numbers and spatial parameters are necessary for the channel characterization:

- The longitudinal aspect ratio $Æ_\parallel$ (length L over height d of the channel). The value for the experimental channel is about 200.

- The transverse aspect ratio $Æ_\perp$ (width l over height d of the channel). The value for the experimental channel is 42.5.

- Péclet number $\mathrm{Pe} \equiv \mathrm{RePr}$ represents the ratio of inertial and thermal diffusion forces.

- Grashof number Gr is the ratio of the buoyancy to viscous force acting on the fluid, $\mathrm{GrPr} \equiv \mathrm{Ra}$.

For a no-flow case (i.e. $\mathrm{Re} = 0$), the system is reduced to pure Rayleigh–Bénard without preferred direction where the critical Ra number is given in the table 1.1. When a Poiseuille flow is added, the critical Ra values vary for the different patterns available depending on the following parameters Re, Pr and $Æ_\perp$, see Koschmieder (1993) [30]. However these patterns generally tend to align with the shorter vertical sides of the box. Details can be found in [16] and [17].

For $\mathrm{Re} > 0$, the state area between $\mathrm{Ra}_{c\parallel}$ (the critical Ra for the appearance of longitudinal rolls) and $\mathrm{Ra}_{c\perp}$ (the critical Ra for the appearance of longitudinal rolls) will exhibit longitudinal rolls $\mathrm{R}_\parallel$: these rolls have their axis parallel to the flow direction. And finally if you increase Ra above $\mathrm{Ra}_{c\perp}$, you will reach the transversal rolls $\mathrm{R}_\perp$ region where the standard state is only composed of rolls which axes are perpendicular to the flow. We will not present high Re flows in which viscous instabilities add Tollmien–Schlichting waves (details available in Schlichting and Gersten (2003) [57]).

The first experimental study on the full RBP problem is from Paul Idrac [23] in 1920, but he only observed longitudinal rolls. Eighteen years later, Bénard and Avsec [4] reported the detection of both longitudinal and transverse rolls.

1.3.1 Applications

Thermo-convective flows: RB, RBP but also Rayleigh-Marangoni (surface tension related convection) and Rayleigh-Soret (two phase flow convection) are some of the most studied topics in fundamental fluid mechanics because of their complexity. Most of the numerous scientific papers published every year on RB and RBP flows are motivated by fundamental research on hydrodynamic linear and non-linear stability. In addition, one should not forget all the more "exotic" Rayleigh–Bénard flows between porous media or where magnetic fields work alongside gravity field. In addition, RBP flows are also encountered in everyday life and industrial applications:

Atmospheric study The main motivation of the first experiments done by Bénard [2] at the beginning of the 20^{th} century was the comprehension of some meteorological phenomenon such as the alignment of clouds under the action of the wind.

Chemical Vapor Deposition Chemical Vapor Deposition is an industrial process for the fabrication of inorganic, very thin layers. This process is mainly used for the production of microelectronic circuits and for magnetic and optic data storage devices.

In a reactor, a mix of inert and reactive gazes is used to lay down a thin layer of material by pyrolysis on a heated substrate. The aim of this process is to achieve the most regular layer, at a certain requested thickness, using mixed convection flow. Depending on the mode of instability, thermo-convective patterns can improve or worsen the layer quality. Details can be found in [28] and [24] and a summary of different cases is available in [43].

Electronic devices cooling The miniaturization of electronic devices has increased the amount of heat generated per volume, which has become a limiting factor to the efficiency of the modern computers, especially for laptops. The cooling device (air or water in certain special cases) flowing between the chip and the printed circuit board (PCB) can be modeled by a plane flow with a temperature gradient between surfaces. Under certain conditions, the heat flux can be optimized using Rayleigh–Bénard–Poiseuille convection [43].

Magneto-hydrodynamics (MHD) Finally, magneto-hydrodynamics – the dynamics of electrically conducting fluids – in which phenomenon comparable to RB and RBP flows can be observed are of first importance in plasma research like plasma confinement (for nuclear fission), liquid-metal cooling for nuclear reactor or even boat propulsion (the "Yamato", a Mitsubishi boat using magneto-hydrodynamic drive can travel at 15 km/h).

1.4 Stability

1.4.1 Stability definition

A state (position, flow velocity profile, quantum state, etc.) of a dynamic system (pendulum, channel, atom, etc.) is called stable when, subject to a perturbation (a deviation from the initial state), it returns to its unperturbed state by itself.

(a) Stable position (b) Unstable position

Figure 1.7: A stable position subjected to a perturbation will return to its initial state.

From a mathematical point of view, stability is defined using a norm[4] $\|\cdot\|$ in a phase space of perturbation. The stability is defined as the evolution of $\|\cdot\|$ with respect to $\|\cdot\|$ of the base state.

Asymptotic stability: A state X_0 is said to be asymptotically stable if, for any other state $x = x(t)$:

$$\exists\ \epsilon > 0 \Leftrightarrow \|x(0) - X_0\| < \epsilon \Rightarrow \lim_{t\to\infty} \|x(t) - X_0\| = 0$$

Global stability: A state X_0 is said to be globally stable if it is asymptotically stable for any ϵ:

$$\forall x \ \lim_{t\to\infty} \|x(t) - X_0\| = 0$$

Marginal stability (neutral stability): One speaks of marginal stability when a finite amplitude perturbation will produce undamped everlasting bounded oscillations around the initial state.

[4] A norm is defined as a function satisfying homogeneity and subadditivity.

Generally the stability of a dynamical system is described by a set of nonlinear equations which cannot be solved analytically. An approximate solution can be obtained through the linearization of the problem around a reference state. For RBP, this base solution is the Poiseuille flow with vertical heat conduction and the linearization can be obtain with a perturbations analysis. This approximation is strictly correct when the system is exactly in the critical state (i.e. in a marginal state) and its accuracy decreases as Ra increases. For even larger Ra, this linear solution will eventually grow to the infinity while experimental systems exhibit only limited grow until a saturated state is reached, which requires non-linear components to be fully modeled.

1.4.2 Instability

Theoretically, any perturbation acting on a linearly modeled unstable state will grow indefinitely (however, real system evolutions are bounded). From a mathematical point of view, the set of linearized equations representing an unstable system has at least one of its roots with a real part greater than zero.

For closed systems, the concept of "absolute" instability completely describes any situation that could occur: a single perturbation will always grow indefinitely eventually filling the full system. In an open system, however both temporal and spatial evolutions of the perturbation have to be taken into account. These concepts were introduced in fluid mechanics by Huerre and Monkewitz (1985) [21].

In the RBP system the upstream phase velocity is in competition with the Poiseuille flow (the advection). The status of the instability is determined upon them.

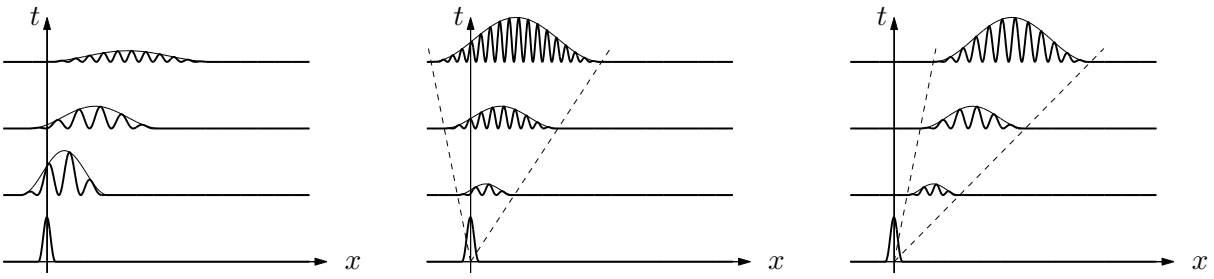

(a) Stability (b) Absolute instability (c) Convective instability

Figure 1.8: Absolutely and convectively linearly unstable states evolution with time. A convective instability will have its both edges moving in the flow direction while an absolute instability will have its edges moving in opposite directions, upstream and downstream.

Absolute instability

An absolute instability will, in any frame of reference, grow and propagate itself in any direction (figure 1.8(b)). In a real bounded system, it will completely fill the entire system until a saturation state.

Convective instability

A convective instability will grow and propagate only in a particular moving frame of reference which is attached to it (figure 1.8(c)). In a fixed frame of reference, this kind of instability will move away and will decrease for every fixed point of view. In a real bounded system, it will

therefor vanish. In a RBP system, a convective instability will be swept away by the Poiseuille flow and will eventually leave the channel.

Mathematically, these instabilities can be observed through the introduction of a Dirac function in the source term in the linearized perturbation equation; the solution in this particular case is given by a function (or a set of functions) called the Green function[5]. The calculation and the examination of the long time evolution of this function allow the characterization and the determination of nature of the instability.

A single perturbation on an absolutely unstable system is enough to produce, at least asymptotically, a coherent structure. In this configuration, only the "natural" modes (i.e. particular frequencies that are channel dependant) are amplified by the system. It is slightly sensitive to the rest of the noise spectrum (white noise). However in a convectively unstable system, a single perturbation is never sufficient to destabilize the system. To be able to observe a convective pattern, a perpetual excitation is necessary; but here the system acts as a full spectrum amplifier. The observed instability is the result of the spatial amplification of all frequencies.

In real systems, where absolutely unstable states are separated from rest state by the convectively unstable ones; the experimental setup has to be very quiet and subject a minimum level of noise to avoid the onset of longitudinal rolls during the journey through convective area.

1.5 Stability analysis applied to RBP

Depending on the initial and boundary conditions considered for the RBP system, several modes can be observed. Obviously, when the Re is equal to zero, the system is reduced to pure RB. In an unbounded infinite system, there is no preferred direction: in any case, the critical $\mathrm{Ra_c}$ value is unique and equal to 1708 for every mode. The lack of preferred direction prevents any distinctions between them. Then, when a Poiseuille flow is added, several convective structures presented previously can be observed among which one can have longitudinal $\mathrm{R}_{\parallel}$ and transverse $\mathrm{R}_{\perp}$ rolls.

The convective pattern existing in an infinite system does not behave as in a finite system where vertical edges limit the number of observable mode frequencies:

Infinite transverse aspect ratio $\text{Æ}_{\perp} = l/d \to \infty$ When the system is unbounded in both $\mathbf{e}_x$ and $\mathbf{e}_y$ directions, linear stability shows that the longitudinal rolls $\mathrm{R}_{\parallel}$ are always more unstable than the transverse rolls $\mathrm{R}_{\perp}$. The critical $\mathrm{Ra_{c\parallel}}$ is a constant and thus always smaller than the $\mathrm{Ra_{c\perp}} = \mathrm{Ra_{c\perp}(Re)}$. The Poiseuille flow is expected to stabilize the flow in the transverse direction; the longitudinal rolls will appear before the transverse ones.

Increase Ra from zero, for a fixed value of Re, the system will first leave the stable conduction area to reach the longitudinal rolls convection area $\mathrm{Ra_{c\parallel}}$; then it will access to the convectively unstable part of the state map defined by $\mathrm{Ra_{c\perp}^{conv}}$, and eventually another increase will bring the system to the absolutely unstable region defined by $\mathrm{Ra_{c\perp}^{abs}}$ (see figure 1.9).

The Rayleigh and the Reynolds number are linked together in a bijective relation; in the same way as Ra we can define $\mathrm{Re_c}$ the Reynolds number at which the system will become unstable (convectively or absolutely). $\mathrm{Re_c}$ can be obtained along a horizontal path in the Ra-Re state map (figure 1.9).

[5]Being a linear operator L, the Green function is the solution of the equation: $L\{G(x,s)\} = \delta(x-s)$ where δ is Dirac function

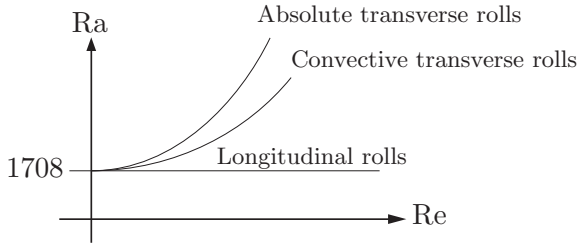

Figure 1.9: Infinite transverse aspect ratio state map: for every Ra smaller than 1708, heat transmission is achieved only through pure conduction; for higher Ra, all three lines represent the onset limit for different mode.

Finite transverse aspect ratio $\mathit{Ar}_\perp = l/d < \infty$ Lateral confinement has two distinct effects:

- it has a stabilizing effect on both rolls species; however, it increases $\mathrm{Ra}_{c\parallel}$ more, and so the convection onset defined by Ra_c becomes $\mathrm{Ra}_c = \min(\mathrm{Ra}_{c\perp},\mathrm{Ra}_{c\parallel})$.
- When $\mathrm{Re} < \mathrm{Re}_c$, the lateral confinement promotes the appearance of transverse rolls $\mathrm{R}_\perp$. However, when $\mathrm{Re} > \mathrm{Re}_c$ (i.e. when the shear exceeds some critical value), the flow becomes dominant and the vertical edges resume the easier appearance of the longitudinal rolls $\mathrm{R}_\parallel$ (see the small area enclosed between the transverse rolls curve and the longitudinal rolls line on figure 1.10).

As presented in figure 1.10, $\mathrm{Ra}_{c\perp} = \mathrm{Ra}_{c\perp}(\mathrm{Re},\mathit{Ar}_\perp,\mathrm{Pr})$; both the transverse aspect ratio $\mathit{Ar}_\perp$ and the Prandtl number Pr have a strong influence on the critical Rayleigh value for the transverse mode as opposed to the critical Ra for the longitudinal rolls which is independent of Pr.

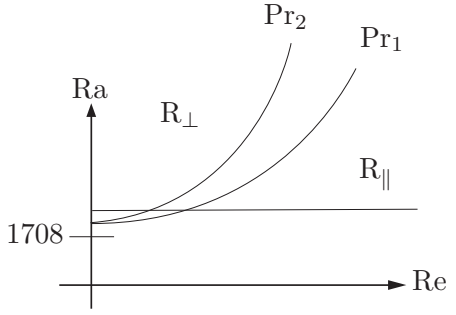

Figure 1.10: Finite transverse aspect ratio state map according to Luijkx *et al.* [34] for two different Prandtl numbers ($\mathrm{Pr}_1 < \mathrm{Pr}_2$). The missing scales are Pr and $\mathit{Ar}_\perp$ dependent. The horizontal line is the stability limit for the longitudinal rolls while the growing curves are the limits for transverse rolls. In fact, for every Pr, two separate curves for the absolute and for the convective state should be considered.

In the framework of the linear stability, the eigenvalue problem describing $\mathrm{R}_\parallel$ in a fully developed region is independent of Re and can be reduced to the 2D Rayleigh–Bénard problem independently of $\mathit{Ar}_\perp$ (except that for finite $\mathit{Ar}_\perp$ the spanwise wave length is quantized) considering a cross-section plane. For 3D perturbations, the linear stability analysis in an infinite $\mathit{Ar}_\perp$ system can be reduced to 2D perturbations in a 2D system (see Gage & Reid [19]) using a Squire-like transform: Squire (1933) [62] had demonstrated that a 3-D disturbance in an unbounded shear flow can be reduced to a 2-D disturbance with a smaller critical parameter value; while the full 3-D system with finite $\mathit{Ar}_\perp$ cannot be simplified (see [33], [44] and [29]).

1.5.1 Mathematical description of RBP flow

Landau's theory: after the onset

For a steady flow, linear theory of stability [18] describes the perturbation velocity $\boldsymbol{u}'(\boldsymbol{x},t)$ through a spectrum of independent modes under the form of:

$$\boldsymbol{u}'(\boldsymbol{x},t) = \boldsymbol{u}(\boldsymbol{x},t) - \boldsymbol{U}(\boldsymbol{x}) = A(t)\boldsymbol{f}(\boldsymbol{x}) + A^*(t)\boldsymbol{f}^*(\boldsymbol{x}) \tag{1.8}$$

where $A(t) \propto \mathrm{e}^{st}$ is a complex amplitude whose growth rate is given by $s \equiv \sigma + \mathrm{i}\omega$; $\boldsymbol{U}(\boldsymbol{x})$ is the unperturbed flow velocity, $\boldsymbol{u}(\boldsymbol{x},t)$ is the total flow velocity and "$*$" denotes the complex conjugate (cc).

When $\mathrm{Ra} < \mathrm{Ra_c}$, the system is stable. All disturbances have $\sigma < 0$; they will decrease with time. As soon as $\mathrm{Ra} = \mathrm{Ra_c}$ a unique normal mode becomes marginally stable, i.e. $\exists!\ s_1 = \sigma_1 + \mathrm{i}\omega_1$ with $\sigma_1 = 0$. And finally, as $\mathrm{Ra} > \mathrm{Ra_c}$, σ_1 will become larger than 0 while for all other modes, $\sigma < 0$. Other modes will eventually see their σ becoming positive when Ra becomes sufficiently large. One has:

$$\sigma_1 = K(\mathrm{Ra} - \mathrm{Ra_c}) + \mathcal{O}\{(\mathrm{Ra} - \mathrm{Ra_c})^2\} \text{ when } \mathrm{Ra} \to \mathrm{Ra_c} \tag{1.9}$$

with K a positive constant. Under linear theory [18], when the system is just slightly supercritical, only the most unstable mode can grow while all others are decaying. After enough time, non-linear effects will produce harmonics that will moderate the exponential growth of the fundamental unstable mode. According to Landau, the amplitude of the fundamental mode of the instability can be described by:

$$\frac{\mathrm{d}|A|^2}{\mathrm{d}t} = 2\sigma\,|A|^2 - \zeta\,|A|^4 \tag{1.10}$$

where ζ is the Landau constant. If ζ were equal to zero, one would recover the linear equation; but here the second term on the right hand-side is able to increase or moderate the exponential growth rate of perturbation depending on the signs of ζ and σ. Equation (1.10) can be written as a linear equation of $|A|^{-2}$:

$$\frac{\mathrm{d}\,|A|^{-2}}{\mathrm{d}t} + 2\sigma\,|A|^{-2} = \zeta. \tag{1.11}$$

Using the assumption that $\sigma \neq 0$, the general solution is given by:

$$|A|^{-2} = \frac{\zeta}{2\sigma} + \left(A_0^{-2} - \frac{\zeta}{2\sigma}\right)\mathrm{e}^{-2\sigma t} \quad \text{where} \quad A_0 = |A(t=0)|\,,$$

we can then rewrite the previous solution (with positive exponentials for $|A|$):

$$|A|^2 = A_0^2 \Big/ \left(\frac{\zeta}{2\sigma}A_0^2 + \left(1 - \frac{\zeta}{2\sigma}A_0^2\right)e^{-2\sigma t}.\right) \tag{1.12}$$

When $\mathrm{Ra} > \mathrm{Ra_c}$ (i.e. $\sigma > 0$ see eq. (1.9)) and $\zeta > 0$ ($\zeta < 0$ would lead in this case to a negative amplitude modulus); one has $\forall\ A_0$:

$$\lim_{t\to\infty} |A(t)| \equiv A_e = \left(\frac{2\sigma}{\zeta}\right)^{1/2}. \tag{1.13}$$

This new stable state which amplitude is A_e is called supercritical. The state is unstable for $\mathrm{Ra} > \mathrm{Ra_c}$ but will settle down to a new stable flow almost independent of the initial condition

A_0 (see figure 1.11(a)). Using equation (1.9) and neglecting higher order (Ra-$\mathrm{Ra_c}$) terms, one can write for the new stable state:

$$A_e \propto (2K(\mathrm{Ra} - \mathrm{Ra_c})/\zeta)^{1/2} \tag{1.14}$$

This result is of main importance: the amplitude of the fundamental mode A_e is proportional to the square root of the reduced Rayleigh number ($\mathrm{Ra} - \mathrm{Ra_c}$), see figure 1.11(b).

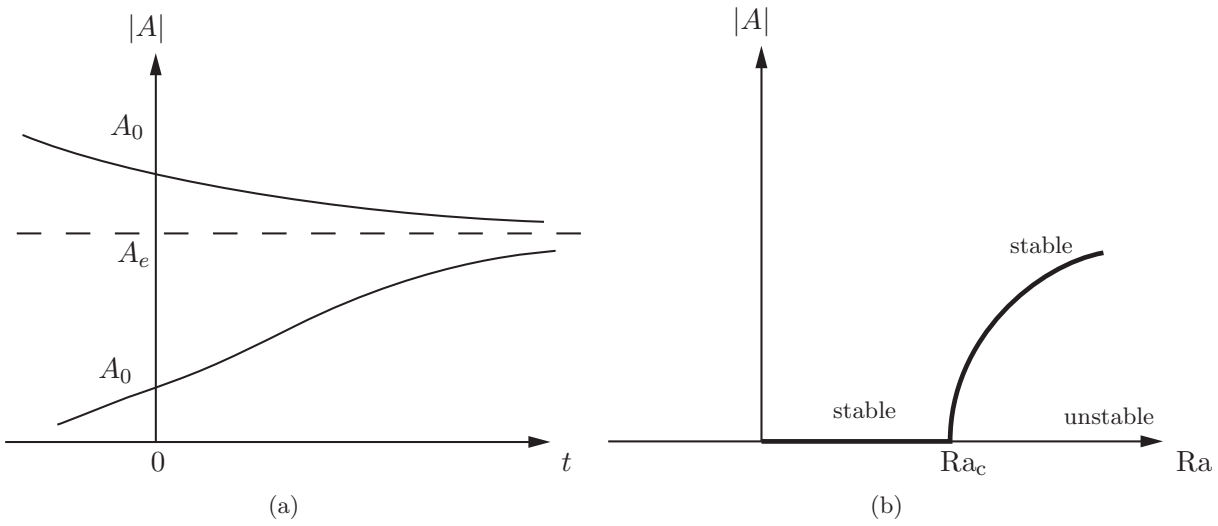

Figure 1.11: Supercritical stability according to Drazin and Reid (2004) [18]. (a) Two different initial conditions A_0 will eventually lead to the same supercritical state $A_e = A_e(\mathrm{Ra} > \mathrm{Ra_c})$. (b) Bifurcation curve: the amplitude $|A|$ is plotted as a function of Ra for $\zeta > 0$.

According to the Landau equation, for $\mathrm{Ra} < \mathrm{Ra_c}$ the steady basic flow is stable and becomes unstable only when $\mathrm{Ra} > \mathrm{Ra_c}$. Then the system will eventually reach a new stable state A_e. In addition, more complete models may exhibit further additional bifurcations from the solution $|A| = A_e$.

General modeling

For the general modeling of RBP flows, the necessary set of hydrodynamic equations (see [12]) consists of :

- The equation of continuity:
$$\frac{\partial \rho}{\partial t} + \frac{\partial}{\partial x_i}(\rho u_i) = 0 \tag{1.15}$$
where $\rho = \rho(\boldsymbol{x}, t)$ is the density, $u_i = u_i(\boldsymbol{x}, t)$ the velocity.

- The stress equation:
$$P_{ij} = -p\delta_{ij} + 2\mu e_{ij} - \frac{2}{3}\mu\delta_{ij}e_{kk} \tag{1.16}$$
where P_{ij} are the stress components, μ the viscosity and e the rate of increase of strain given by:
$$e_{ij} = \frac{1}{2}\left(\frac{\partial u_i}{\partial x_j} + \frac{\partial u_j}{\partial x_i}\right). \tag{1.17}$$

- The equation of motion:
$$\rho\frac{\partial u_i}{\partial t} + \rho u_j \frac{u_i}{x_j} = \rho X_i + \frac{\partial P_{ij}}{\partial x_j} \tag{1.18}$$
where X_i is the ith component of the the external force acting on the fluid.

- The rate of energy dissipated irreversibly by viscosity:
$$\Phi = 2\mu e_{ij}^2 - \frac{2}{3}\mu(e_{ij})^2 \tag{1.19}$$

- And finally the equation of heat conduction:
$$\rho\frac{\partial}{\partial t}\left(c_\mathrm{v}T\right) + \rho u_j \frac{\partial}{\partial x_j}\left(c_\mathrm{v}T\right) = \frac{\partial}{\partial x_j}\left(\kappa\frac{\partial T}{\partial x_j}\right) - p\frac{\partial u_j}{\partial x_j} + \Phi \tag{1.20}$$

This system must be supplemented by an equation of state, for the case of small temperature variations, we can use the 1-term Taylor expansion of $\rho(T)$:

$$\rho = \rho_0\left(1 - \alpha(T - T_0)\right), \tag{1.21}$$

where T_0 is a suitable defined mean temperature.

These equations are quite general, but they can then considerably simplified by the use of the *Boussinesq approximation* [7]: consistent with the assumption of small temperature variations underlying equation 1.21, the thermophysical properties of the fluid are assumed to remain constant. The only term where density variations need to be kept is the driving term ρX_i in the equation of motion (1.18) as the resulting acceleration can be quite large; larger than the acceleration due to the inertial term.

Unfortunately, even with the Boussinesq approximation, this set of equations cannot be solved directly. Only few boundary conditions will lead to a system with an analytical solution. Another way to study mathematically thermo-convective patterns in Rayleigh–Bénard–Poiseuille flows is to study only the amplitude A of the convective structures instead of the whole velocity field as summarized next.

Amplitude modeling

The time evolution, growth and saturation of convective rolls in pure RB have first been studied in 1969 by Newell *et al.* [42] and by Segel [59]. They showed that the amplitude of the dynamical field can be described by a complex Ginzburg–Landau (CGL) equation. Based on the work by Walton (see [66]) Martinand *et al.* [36] have used the following equation for the envelope equation:

$$\frac{\partial A}{\partial t} = (r - \rho^2)A - \rho(c + \eta)\frac{\partial A}{\partial x} + \mathrm{i}\rho\eta\frac{\partial^2 A}{\partial y^2} + (\frac{\partial}{\partial x} - \mathrm{i}\frac{\partial^2}{\partial y^2})^2 A - A^2\overline{A} \tag{1.22}$$

where t denotes time and x and y the streamwise and the transverse coordinates, respectively. The real control parameters r and ρ are the rescaled Rayleigh and Reynolds numbers, while c and η are two positive (real) function of the Prandtl number. This equation describes both linear and weakly non-linear dynamic aspect of the system and allows the description of the evolution of the system in the neighborhood of a bifurcation point determined by the linear stability.

This formalism has been extended to the full RBP flow by Müller, Lücke and Kamps [39] in 1989 with corresponding DNS[6] results published in [41]; and again extended in 1993 by Müller

[6] Direct numerical simulation (DNS) is a simulation in which the Navier-Stokes equations are numerically solved without any turbulence model.

et al. [40] to take both longitudinal and transverse rolls into account. For each parameter of the CGL, one has to calculate a series expansion based on Re, and use them to compute the curve separating the convectively and the absolutely unstable area for the transverse rolls $R_\perp$. These results present good agreement with the experimental work from Ouazzani *et al.* [47] and [48] for small Ra and small Pe.

1.6 Interests and Objectives of the present study

The first aim of this work is the experimental study of RBP flows in a large transverse aspect ratio channel and comparison with the linear analysis performed by Carrière and Monkewitz (1999) [9] on the onset of $R_\perp$ and on the transition between convective and absolute instabilities in RBP flows. The largest challenge of such an experimental measurement is to be able to observe transverse rolls without triggering longitudinal rolls, i.e. to be able to dive under the (most unstable) longitudinal rolls area. These results will also be confirmed by the observation of the impulse response of the system. Depending on several flow parameters, the transition between convective and absolute instability can be directly deduced from the upstream perturbation direction ([9]).

The second aim of this study is the examination of a localized island of supercritical state, which is more often encountered in real systems than perfect uniformly heated ones. We will compare experimental results with asymptotic and numeric studies in the case of a slow varying heating profile done by Martinand, Carrière and Monkewitz (2004) [36] and (2006) [37]. They study the influence of non-uniform heating of the lower wall on linear and nonlinear global modes of RBP flows using analytical computations and direct numerical simulations.

1.6.1 Appearance threshold and behavior of the transverse rolls $R_\perp$

Only few experiments have been performed on the observation of the transverse rolls, and the majority of them were done in a small transverse aspect ratio channel. Platten and Lefebvre (1971) [55] are the authors of the first experimental study of the influence of the flow velocity on the critical Ra, in particular on the increase of $Ra_{c\perp}$ with Re. Using a Schmidt–Milverton [58] type experiment with a transverse aspect ratio $\mathcal{A}_\perp$ of 80 and filled with water (Pr between 6.5 and 7), they observed an increase from 1708 to 2063 when Re is increased from 0 to 28. Unfortunately they understood later than the observed mode was not the transverse but the longitudinal rolls. The observed Ra_c increase is in fact the $Ra_{c\parallel}$ increase; at this large flow velocity, the predicted mode is $R_\parallel$ which onset is supposed to be independent of Re. The most plausible explanation is that they observed convective structures that are still not fully thermally developed in the observed location, and are therefore still Re dependant.

Ten years later Luijkx *et al.* (1981) [34] showed that onset location of transverse rolls was spatially moving with Re. Since the optical system could not detect longitudinal rolls, the authors only made the assumption of the presence of longitudinal rolls $R_\parallel$. Several qualitative comments can be extracted from this publication for a finite width channel using linear temporal stability:

- $Ra_{c\parallel} = Ra_{c\parallel}(\mathcal{A}_\perp)$; $Ra_{c\parallel}$ is independent of Re and Pr. The aspect ratio dependency is shown in figure 1.12.
- $Ra_{c\perp} = Ra_{c\perp}(Re,Pr,\mathcal{A}_\perp)$; $Ra_{c\perp}$ increases with Re, Pr or $1/\mathcal{A}_\perp$ (see figure 1.12).
- $Re_c = Re_c(Pr,\mathcal{A}_\perp)$; Re_c decreases with Pr increase for a fixed value of $\mathcal{A}_\perp$(see figure 1.13).

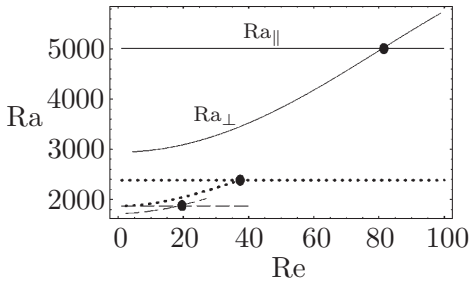

Figure 1.12: Critical Ra as a function of Re for several transverse aspect ratios $\mathcal{AR}_\perp$ computed with linear stability theory. Graph borrowed from Kato and Fujimura (2000) [29]. The solid lines are for $\mathcal{AR}_\perp = 1$, the dotted lines are for $\mathcal{AR}_\perp = 2$ and the dashed lines are for $\mathcal{AR}_\perp = 4$. Pr is 0.71 (air).

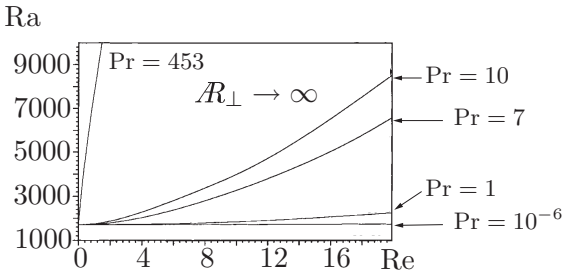

Figure 1.13: Critical Ra for different Pr values when $\mathcal{AR}_\perp \to \infty$. A large Pr tends to stabilize the flow. Graph is from Nicolas *et al.* (2000) [44] using linear stability analysis.

On the other hand, Müller [38] and Müller *et al.* [41] have studied the linear temporal stability of the 2D RBP using small-Re expansion. They solve the linearized perturbation equations and show with a Re power series development that the critical $\mathrm{Ra}_{c\perp}$ (transverse rolls onset) can be approximated by:

$$\mathrm{Ra}_{c\perp}(\mathrm{Re},\mathrm{Pr}) = 1707.762+ \\ \left(0.02156 + 0.02378\mathrm{Pr} + 2.194\mathrm{Pr}^2 + 0.3636\mathrm{Pr}^3 + 0.42\mathrm{Pr}^4\right)\cdot(0.5117+\mathrm{Pr})^{-2}\,\mathrm{Re}^2 + \mathcal{O}\left(\mathrm{Re}^4\right). \tag{1.23}$$

While the transition between the convective and the absolute state is given by:

$$\mathrm{Ra}_{c\perp}(\mathrm{Re},\mathrm{Pr}) = 1707.762+ \\ \left(0.8681 + 5.7927\mathrm{Pr} + 18.6829\mathrm{Pr}^2 + 23.0719\mathrm{Pr}^3 + 13.5426\mathrm{Pr}^4\right)\cdot(0.5117+\mathrm{Pr})^{-2}\,\mathrm{Re}^2+ \\ \mathcal{O}\left(\mathrm{Re}^4\right). \tag{1.24}$$

According to the authors, these analytical formulas are very accurate (1%) while Pe[7] is smaller than 26; these formulas are also in good agreement with the asymptotic results from Carrière and Monkewitz (1999) [9] who get an approximate critical Ra_c of 1749.98 for the pure RB flow using first order eigenfunctions expansion. Precise quantitative comparison will be presented in figure 3.2.

This study will present measurements of the onset of transverse rolls as a function of Re. Longitudinal rolls will be neglected.

[7] Pe in our experimental channel is always smaller than 15 for any experimental run.

1.6.2 Impulse response

The impulse response is of major importance in the study of dynamical systems. It is the answer of the system to a Dirac excitation. It has been linearly studied by Carrière and Monkewitz in 1999 [9] for a convectively unstable configuration. They observed a lack of symmetry in the wave packet between the streamwise part composed of transverse rolls and the spanwise part composed by more unstable longitudinal rolls. An example is presented in figure 1.14.

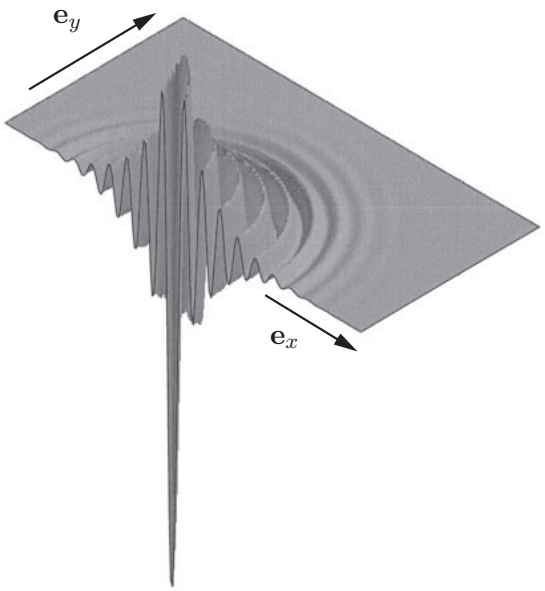

Figure 1.14: Linear computation of an impulse response by Carrière and Monkewitz [9] for a convectively unstable configuration. The lack of symmetry is observable especially in the center of the wave packet where one can observe lateral ears close to the center of the wave packet.

Only few experimental works were proposed on localized heating in RBP flow. An experimental study, covering partly the same experimental topics, should also be mentioned, using previous results by Müller *et al.*, and a Pr equal to 5.8, Trainoff (1997) [65] has studied the noise that drives the observed convection rolls in RBP flows. He uses a channel with a spiral-shape to achieve a long narrow channel $\mathit{Ar}_\perp = 2.2$ and $\mathit{Ar}_\parallel = 59$ with Boussinesq convection in a circular cell. This small aspect-ratio was chosen to ensure a transverse rolls $\mathrm{R}_\perp$ mode. Because of the spiral design, it was essential to match the thermal conductivity of the vertical walls (black parts on figure 1.15) to the working fluid. Therefore, they were created with a mix of two epoxies and aluminium particles that had the same thermal conductivity as the working fluid to avoid horizontal temperature gradients. In our "EPFL" design, this was not a problem because of the pure rectangular design (see figure 2.2); the sidewalls needed to be designed in order to minimize the generation of longitudinal rolls $\mathrm{R}_\parallel$. Their channel, which dimensions are $3.234 \times 7.260 \times 190.8$ mm (height $\times$ width $\times$ length), is enclosed between two circular sapphire plates with a diameter of 101.6 mm (4 inch) and a thickness of 9.78 mm.

Trainoff studied convective instability onset by applying a periodic temperature perturbation at a precise spatial channel location and by tuning the temperature difference until he obtained a neutrally stable state. It is the limit between an absolutely stable (decreasing perturbation) and a convectively unstable state (increasing perturbation, moving with the flow). He reports a convectively unstable boundary for the transverse rolls $\mathrm{R}_\perp$ as a function of the Reynolds number

Figure 1.15: Top view of the sidewalls of Trainoff's channel [65]: the white area is the open channel while the walls are in black. The fluid enters through a hole in the center of the bottom plate and exits through a hole on the periphery after having traveled through the inlet (the small width channel part located in the center), the nozzle and eventually the working section of the channel.

Re:

$$\epsilon_{\text{conv}} = (0.054 \pm 0.002)\text{Re}^2, \tag{1.25}$$

and an absolutely unstable transition given by:

$$\epsilon_{\text{abs}} = \epsilon_{\text{conv}} + 0.2918\text{Re}^2 - 0.0016\text{Re}^4 + \mathcal{O}(\text{Re}^6). \tag{1.26}$$

$\epsilon_{\text{conv}}(\text{Re})$ is defined by the ratio between the critical temperature difference for Re with the critical temperature difference for $\text{Re} = 0$:

$$\epsilon_{\text{conv}}(\text{Re}) = \frac{\Delta T_c(\text{Re}, t)}{\Delta T_c(\text{Re} = 0, t)} - 1. \tag{1.27}$$

In equation 1.27, the critical temperature differences are functions of time because of some channel gap thickness variations during a long time run. Unfortunately, Trainoff did not provide any temporal deviations for equation (1.25).

All the results presented by Trainoff are expressed through temperature differences in order to avoid the computation of Ra (see details in section 2.2.1). Under the Boussinesq assumption, the temperature ratio in (1.27) is equal to the corresponding Ra ratio (with the assumption that $\Delta T_c(\text{Re} = 0, t = 0)$ is corresponding to $\text{Ra}_\text{c} = 1708$):

$$\epsilon_{\text{conv}}(\text{Re}) \approx \frac{\text{Ra}_\text{c}(\text{Re})}{\text{Ra}_\text{c}(\text{Re} = 0)} - 1. \tag{1.28}$$

The second part of this PhD dissertation will present some experimental results on the transition between convective and absolute thermo-convective rolls using a short duration laser pulse in order to observe the system impulse response evolution.

1.6.3 Localized supercritical region

The second part of this thesis is the comparison with analytical and numerical results published by Martinand, Carrière and Monkewitz (2004) [36] and (2006) [37] on localized heating effects. The study observes the effects of a single 2-D non-uniform heating applied on the lower wall of an infinite RBP flow.

The considered single two-dimensional hot spot provides a localized Gaussian supercritical region where the envelope equation formalism is used to approximate the global mode (a localized

instability which frequency and temporal growth rate are coherent over the whole field). A slow varying temperature profile is assumed in order to use a Wentzel–Kramers–Brillouin–Jeffreys (WKBJ) asymptotic expansion (see Jammer [25] and Bender and Orszag [5]) around the two-dimensional double turning point (i.e. stationary point) located at the maximal value of the Ra field. Martinand *et al.* also made comparisons using direct numerical simulations of the effects of this 2-D temperature bump.

The first results are in the work proposed by Carrière and Monkewitz (2001) [10] in which a one-dimensional temperature profile is applied on a two-dimensional flow: only transverse rolls are studied. A global mode is obtained through WKBJ asymptotic expansions allowing the determination of the critical value $\mathrm{Ra_c}$ for global instability as a function of the Ra profile (see figure 1.16).

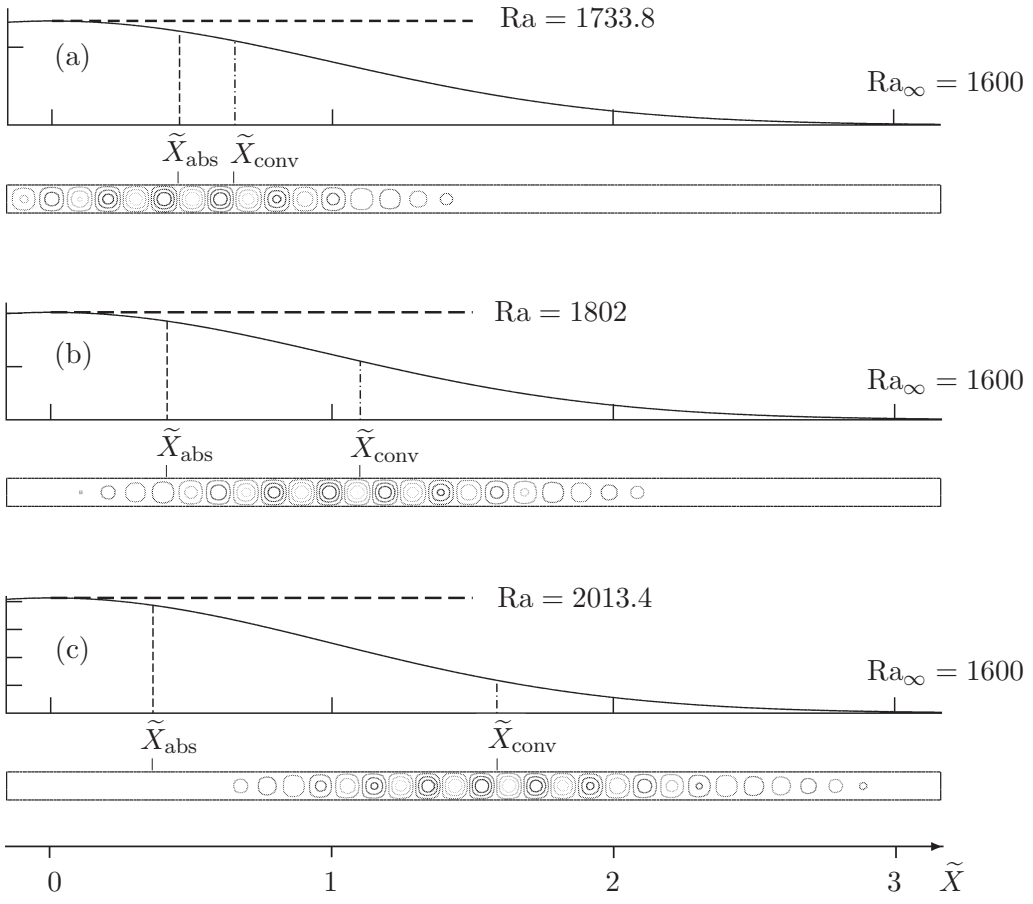

Figure 1.16: One-dimensional analytical analysis results by Carrière and Monkewitz [10]: (a) Re = 0.2; (b) Re = 0.5; (c) Re = 1. The lower part of each subfigure represents isocontours of the temperature perturbation corresponding to marginally stable global modes, while the upper part displays the variation of the Rayleigh number with $\widetilde{X}$ the non-dimensional spatial coordinate.

Thereafter, using envelope formalism previously developed in Carrière *et al.* (2004) [11] for the spatially homogeneous case, Martinand *et al.* [36] analyzed linear global modes for the 2-D slow varying heating profile. As in [10], the frequency is derived from the breakdown of the expansion occurring at the (presently double) turning point. This paper also presents comparisons with numerical simulations of the envelope equation, especially in the vicinity of the turning point where the asymptotic analysis is the most accurate (see figures 1.17 and 1.18).

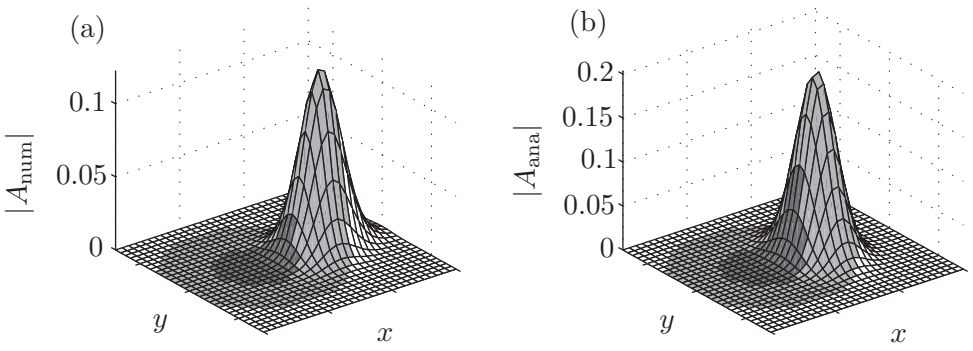

Figure 1.17: Comparison between numerical (a) and analytical (b) three-dimensional amplitude representation respectively for a circular symmetrical temperature spot. The darkest gray represents absolutely unstable areas while mid-dark gray areas are only convectively unstable. Figures are from Martinand *et al.* [36]

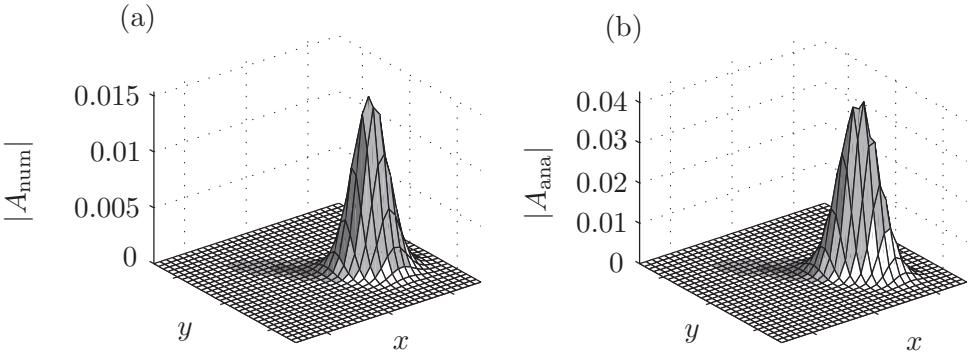

Figure 1.18: Comparison between numerical (a) and analytical (b) three-dimensional amplitude representation respectively for a swept elliptical temperature spot. The darkest gray areas represent absolutely unstable areas while mid-dark gray area are only convectively unstable. Figures are from Martinand *et al.* [36]

The second paper published by Martinand, Carrière and Monkewitz in 2006 [37] proposes a deeper investigation into global modes produced by a localized supercritical spot. As in the previous paper, the envelope formalism is used with WKBJ asymptotics to get a linear approximation of the global mode. Additional DNS results confirm that the analytical study yields the most amplified mode characterized by transverse orientation for the convective rolls aside of the shape of the localized extra-heated area.

In the same way, DNS results on the saturated global mode are discussed in the framework of soft/steep global modes. According to Pier, Huerre and Chomaz (2001) [53], two different classes of mutually exclusive self-sustained global modes can be solutions of the one-dimensional nonlinear evolution equations subject to a slowly varying parameter:

- Soft global modes [52] exhibit a smoothly varying envelope. This mode is due to a saddle point (X^{nl} in figure 1.19) of the local nonlinear dispersion relation.
- Steep global modes [54] are characterized by a sharp front at the upstream boundary of the absolutely unstable area (X^{ca} in figure 1.19). According to Pier *et al.* [53], this mode is the one observed in real physical systems.

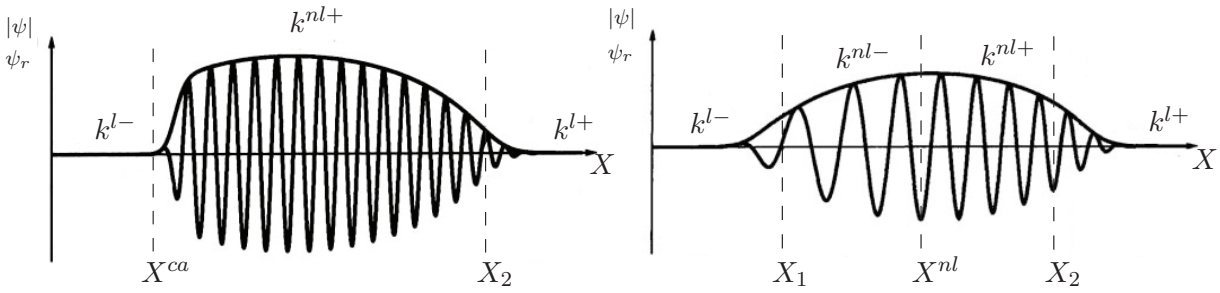

(a) Steep global mode (b) Soft global mode

Figure 1.19: One dimensional steep (a) and soft (b) global mode computed through DNS simulations of the complex Ginzburg–Landau equation by Pier *et al.* [53]. Each graph shows the envelope $|\psi|$ and the real part ψ_r of the CGL solution as functions of the downstream distance X. $k^{l\pm}$ and $k^{nl\pm}$ are corresponding to the analytically computed linear and nonlinear spatial branches in the complex k-plane, (see details in [53])

Preliminary results by Martinand *et al.* [37] tend to confirm these one-dimensional analytical results (see figure 1.20).

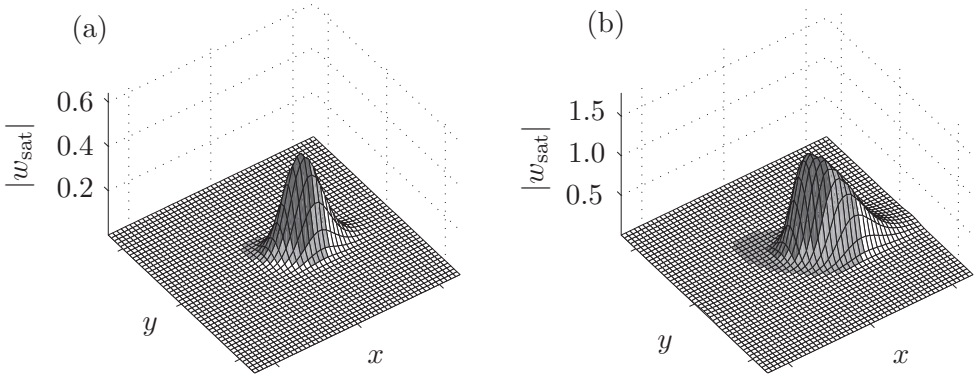

Figure 1.20: Vertical component w of the perturbation velocity of the non-linear saturated mode reproduced from Martinand *et al.* [37] for a swept elliptical temperature spot. (a) $\mathrm{Pr} = 7$, $\mathrm{Re} = 0.38$ and $\mathrm{Ra}_{\max} = 1800$ while $\mathrm{Ra}_{\infty} = 1500$; (b) $\mathrm{Pr} = 7$, $\mathrm{Re} = 0.85$ and $\mathrm{Ra}_{\max} = 2000$ while $\mathrm{Ra}_{\infty} = 1500$.

Experimental confirmations will be presented in chapter 3 of this work. A circular and a swept oblong rectangular temperature bumps will be used as slow varying temperature profiles. In an attempt to observe which mode (rolls orientation) is preferred, this profiles will be large enough to have both a convective and an absolute area. Finally, the amplitudes of the observed convective patterns will be studied in order to see if physical systems actually exhibit the steep nose predicted by nonlinear theory and direct numerical simulations.

Chapter 2

Experimental setup

2.1 Facility description

In this chapter, after a brief description of a small preliminary experiment, the channel used for the main experiments is described in detail in section 2.1.1, together with the temperature and the flow rate control systems. Then the optical setup is presented in section 2.1.2 and the hardware description closes with the techniques used to produce localized heating of the bottom plate (sections 2.1.3 and 2.1.4).

The second part of this chapter is devoted to the different experimental diagnostics. The experimental determination of both the Rayleigh and Reynolds numbers are detailed in sections 2.2.1 and 2.2.2 respectively. The non-invasive Schlieren method to observe the convection rolls is then described in section 2.2.4.

In the third part of the chapter the pure Poiseuille flow without thermo-convective structures (Ra = 0) is characterized in section 2.3.1 and the temperature field for two different spatially varying heating profiles of the lower channel surface is documented in section 2.3.2.

Finally, the last section presents the principal known sources of experimental error.

Pure Rayleigh–Bénard cell

To determine the best observation methods and material for the RBP channel, a small 10 cm diameter circular pure[1] RB cell has been designed with the same gap as the future RBP channel. Its main purpose was the selection of the most accurate, non-invasive technique useable during week long experimental runs. In addition to shadowgraphy and Schlieren [60] (see section 2.2.4, several other techniques have been tested in the RB cell but not retained. They are :

- Synthetic Schlieren [60]: the deformations of a pattern seen through a layer with refractive index variations are observed and the index of refraction field is deduced computationally. This method does not require a parallel light beam but, to be accurate for a large multi-cell pattern, a camera with a very high resolution which was not readily available is required.

- Sheet of Thermo-chromic Liquid Crystals (TLC) [13]: a thin layer of liquid crystal enclosed between polycarbonate sheets is glued on the lower surface of the channel. This method was found to provide a poor observation quality, as only the imprint of the convective structures on the lower boundary surface is observed. The second limitation is the temperature range of these crystal sheets (5°C) which prevents the use of the floating inlet tank temperature as reference. An example of this technique is shown in figure 2.1.

- Liquid crystal slurry: finally, liquid crystal particles encapsulated in polycarbonate spheres ($15-50$ μm diameter) have been dispersed into the working fluid to be used as temperature

[1] In this context, pure RB cell means a closed fluid volume heated from below as opposed to the open system of the RBP channel.

sensitive PIV particles. The density of these particles, slightly larger than that of water caused their sedimentation before they would reach the end of the channel. At the very low speeds in the RBP channel it proved impossible to meet the density matching requirements.

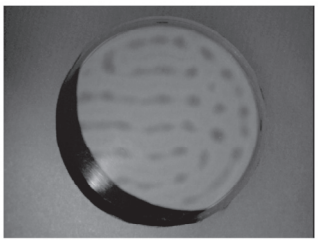

Figure 2.1: RB convective pattern observed with TLC sheet in water (Pr = 6.5) at Ra = 4'000.

2.1.1 Rayleigh–Bénard–Poiseuille channel

The final Rayleigh–Bénard–Poiseuille channel has a frame consisting of two brass plates (parts ⓒ and ⓔ on figure 2.2) with windows separated by a spacer. The resulting channel is 4 mm high, 170 mm wide and roughly 800 mm long. This provides a very large transverse aspect ratio $\mathcal{R}_\perp$ of 42.5 and a longitudinal aspect ratio $\mathcal{R}_\parallel$ of about 200. The manufacturing tolerances for the basic structure are 10 μm. Two cross-sections of the channel defined in figure 2.3 are presented in figures 2.4 and 2.5.

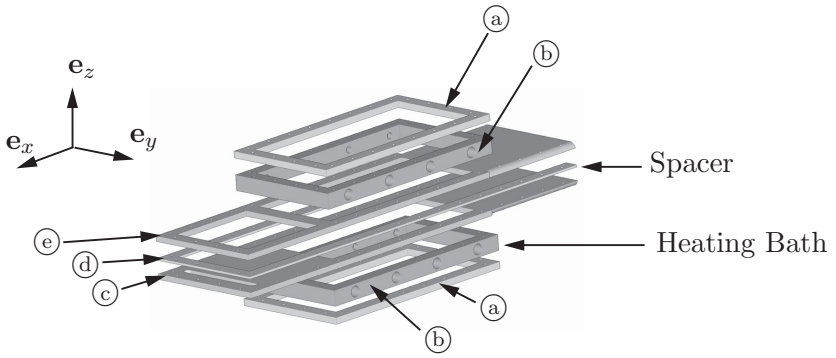

Figure 2.2: Rayleigh–Bénard–Poiseuille channel: Two pieces of brass ⓒ and ⓔ separated by a spacer ⓓ. ⓑ indicates the frames of the temperature controlled heating and cooling baths which are sealed with the transparent covers ⓐ. The origin of the coordinate system is located in the vertical plane where both heating and cooling surfaces start on the upstream side, at half-width and half-height of the channel. This reference frame is also shown in figure 1.6

Each brass structure is fitted with a 5.5 ± 0.2 mm thick transparent window made of floated borosilicate (Borofloat 33 from Schott AG). Floated materials (i.e. glass or borosilicate) are obtained by floating the molten material on a bed of molten tin. This method produces uniform thickness and very flat surfaces (nominal tolerances are 10 μm). In addition, the borosilicate has a smaller linear thermal expansion coefficient λ ($3.25 \cdot 10^{-6}$ K^{-1} instead of $10 \cdot 10^{-6}$ K^{-1}) and the same nominal thermal conductivity κ (1.2 W/(m·K)) as standard extra-white glass (Schott AG) for almost the same optical properties, which is essential for the observation method. Due to the large size of the channel, it was not possible to use windows with higher heat conductivity, such

as sapphire (around 40 W/(m·K) - as a reference copper has a heat conductivity of around 400 W/(m·K)). These windows are fitted into the brass frames with silicone joints. These are thick enough to let the windows expand due to temperature gradients without breaking (figure 2.35). The windows are wider than the gap to ensure that they rest against the spacer ⓓ which ensures a constant gap height. The largest error on the gap dimension is observed at mid-width near both the upstream and downstream edges of the windows subjected to the largest Ra corresponding to a temperature difference of 25 °C and 10 °C for oil and water respectively; under these conditions, errors of the gap height in the range of 15 to 40 μm, i.e. up to 1% of the nominal gap height, have been observed. They are principally due to the fact that the windows are only fixed with soft silicone - more rigid mounts have been tried but have all led to breakage of the windows.

On the outside of these windows, a PVC frame ⓑ and a glass cover ⓐ are attached to provide two heat transfer baths. We note that the large thickness of the windows (5.5 mm) is necessary to minimize the deformation caused by the difference between the channel pressure ($\sim$ 0.02 bar above ambient), the pressure within the heating/cooling baths (0.1 bar above ambient) and the ambient pressure.

The inlet of the channel is located in a Plexiglas supply tank of $600 \times 320 \times 320$ mm (length $\times$ width $\times$ height) behind a vertical 100 mm thick porous layer made of small plastic spheres of 4 mm of diameter (see figure 1.4). Its role is to reduce the turbulence created at the tank inlet to the lowest possible level in the RBP channel. The whole supply tank is covered with expanded polystyrene (EPS) panes to low-pass filter small laboratory temperature fluctuations. To avoid free surface waves inside the tank, it is also pressurized at about 0.08 bar with a gravity column system shown in figure 2.11. The pressure of the fluid recirculated into the supply tank is maintained constant by the hydrostatic pressure exerted by the fluid contained in a vertical column. The outlet of the channel consists of a spanwise slit in the bottom of the channel followed by a vertical channel of the same width as the RBP channel (see fig. 1.4). This vertical channel is filled with another 140 mm layer of small spheres, to a level 80 mm below the test section, before it contracts to a drain tube. This second porous layer ensures that the transverse pressure gradient in the test section is negligible all the way to its end and hence minimizes transverse variations of flow velocity in the RBP channel.

The fluid circulation is driven by a pulsation-free gear pump (Micropump® model GB-P35) in order to minimize the level of noise (flow unsteadiness and vibrations) in the system. The flow rate is measured with a self-made capillary flow meter (see section 2.1.1.2).

The whole channel, including the supply tank, is mounted on adjustable soft rubber feet to level the system and to absorb vibrations.

Over weeks of operation, the working fluid is contaminated by dust particles originating from the different devices in the setup. As the flow rate in the test section for all experiments was not high enough to avoid gravitational sedimentation, a “broom system” operated from the end of the channel was implemented to scrape these dust particles from the bottom wall because even minute deposits were found to nucleate undesirable roll patterns or even cause an early onset of instability.

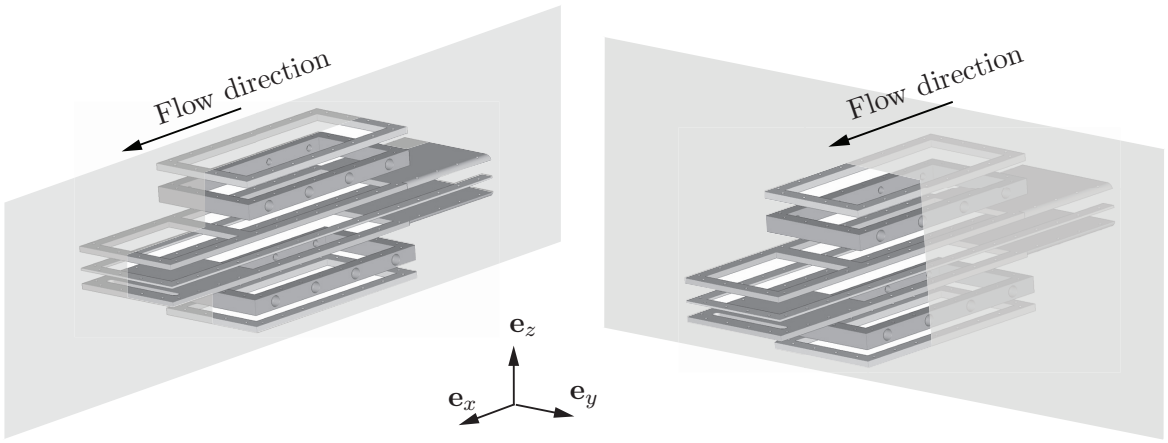

(a) Longitudinal plane (b) Transverse plane

Figure 2.3: (a) shows the position of the longitudinal section of figure 2.5 while (b) locates the transverse section of figure 2.4.

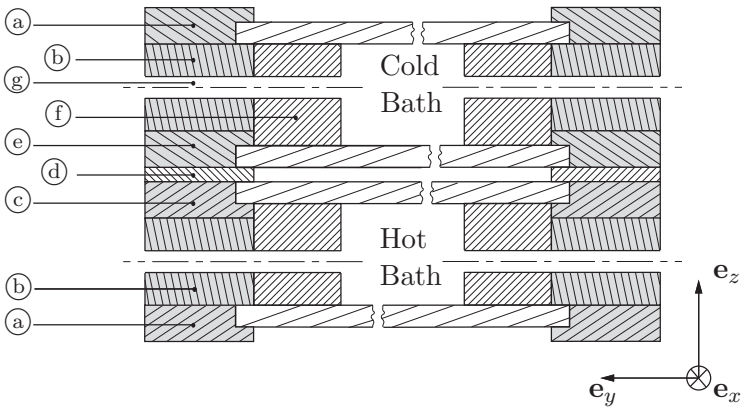

Figure 2.4: Transverse channel cross-section ($\mathbf{e}_y$ – $\mathbf{e}_z$ vertical span-wise plane). As in figure 2.2, ⓐ to ⓔ are the transparent covers and the frames of the heating and cooling baths, brass frames and spacer, respectively. ⓖ is an input/output hole for the temperature controlled circuits and ⓕ is an added Plexiglas frame within the heating and cooling baths to provide "soft" thermal boundary conditions on the periphery of the RBP channel.

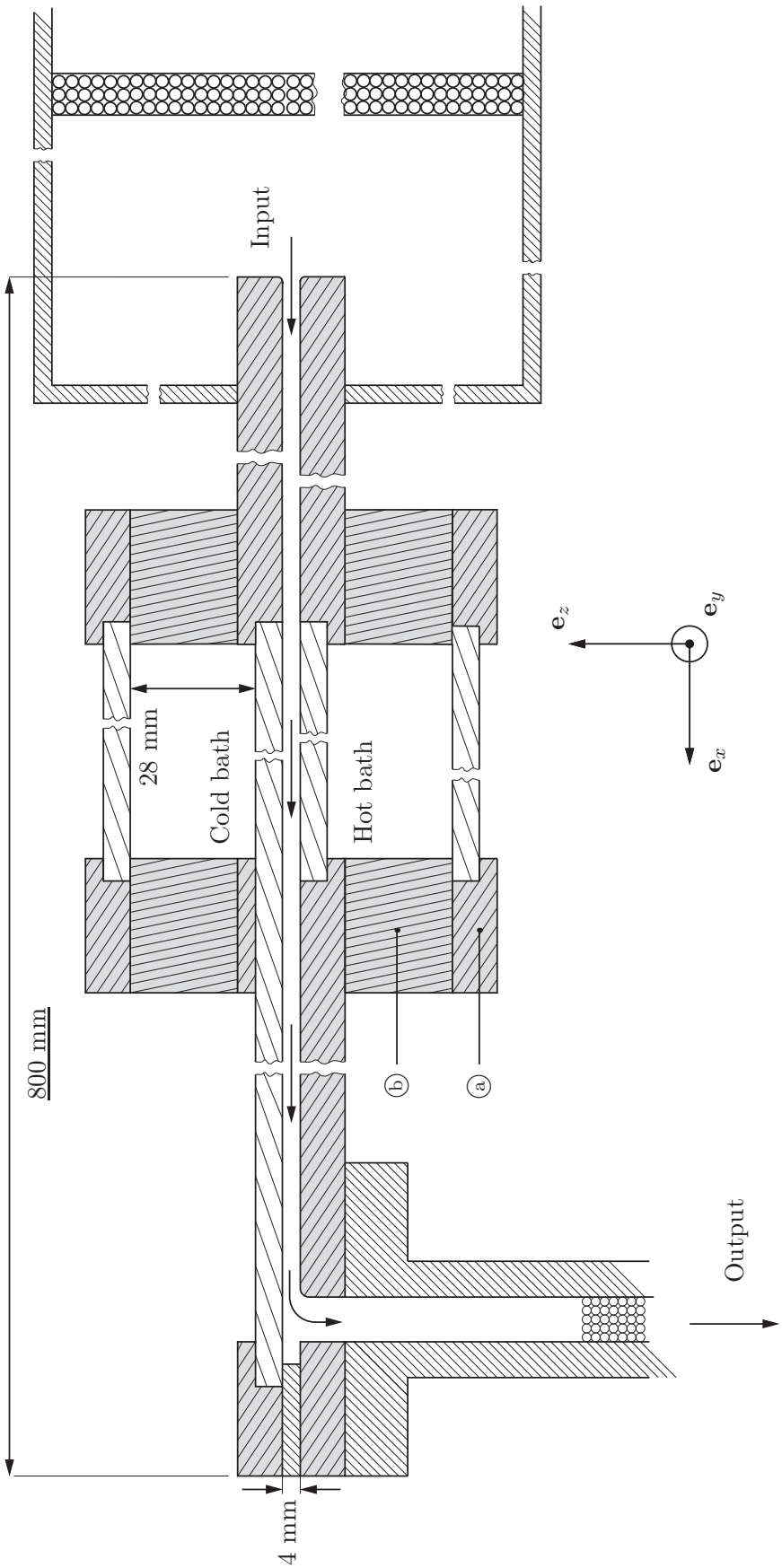

Figure 2.5: Longitudinal channel cross section ($\mathbf{e}_x - \mathbf{e}_z$ vertical stream-wise plane) at mid-span. The channel input protrudes 90 mm into the entrance tank.

Working fluids From analytical and numerical work (see section 1.6) it is known that the stability characteristics of transverse rolls to which this work is mainly devoted are strongly influenced by the Prandtl number. Specifically, the stability properties at high Pr vary very rapidly with Re while this variation is slower at moderate Pr. Hence, at high Pr only a very small interval of Re near zero is necessary to obtain large variations of the critical Ra for transverse rolls, for instance. At moderate Pr the Re-interval to obtain similar variations is correspondingly larger. This immediately implies that the relative importance of the precision on the flow rate (i.e. on the Reynolds number Re) and the precision on the temperature difference (i.e. on the Rayleigh number Ra) is strongly Pr-dependent: A large Pr fluid requires a large temperature difference to reach the critical Ra which reduces the importance of the (absolute) accuracy of the temperature measurement. At the same time, this large increase of the critical Ra is obtained already at very small Re (i.e. flow rate) inside the channel (see section 3.1) so that the uncertainty of Re is the main source of error at high Pr. Correspondingly, small Pr fluids present opposite problems: a small temperature difference is required to reach the critical Ra, while the required range of Re is significantly larger, therefore making the temperature difference in the working section the main source of error.

To test the strong Pr effect, a comparison between a high Pr fluid and a fluid with a Pr of $\mathcal{O}(1)$ was desired. To use an optical method to observe the convection rolls, the working fluids had to be also completely transparent and preferably have a strong variation of refractive index with temperature. Considering these requirements, two different working fluids were selected: distilled water with a Prandtl number Pr of 6.5-7 and white mineral oil with a Pr of about 450.

Distilled water This is a cheap, well documented fluid with a Prandtl number of about 6.5 to 7 and is easily available in the laboratory. For technical reasons, we added some ($< 0.5\%$) bleach to avoid bacterial proliferation. Unfortunately, many problems appear with water: evaporation, saturation with air generating bubbles, and a small refractive index gradient with temperature. Furthermore, oxidation prevents the use of steel or aluminum in the flow facility. Data are shown in figure 2.6; for simplicity, units are specified in the caption only.

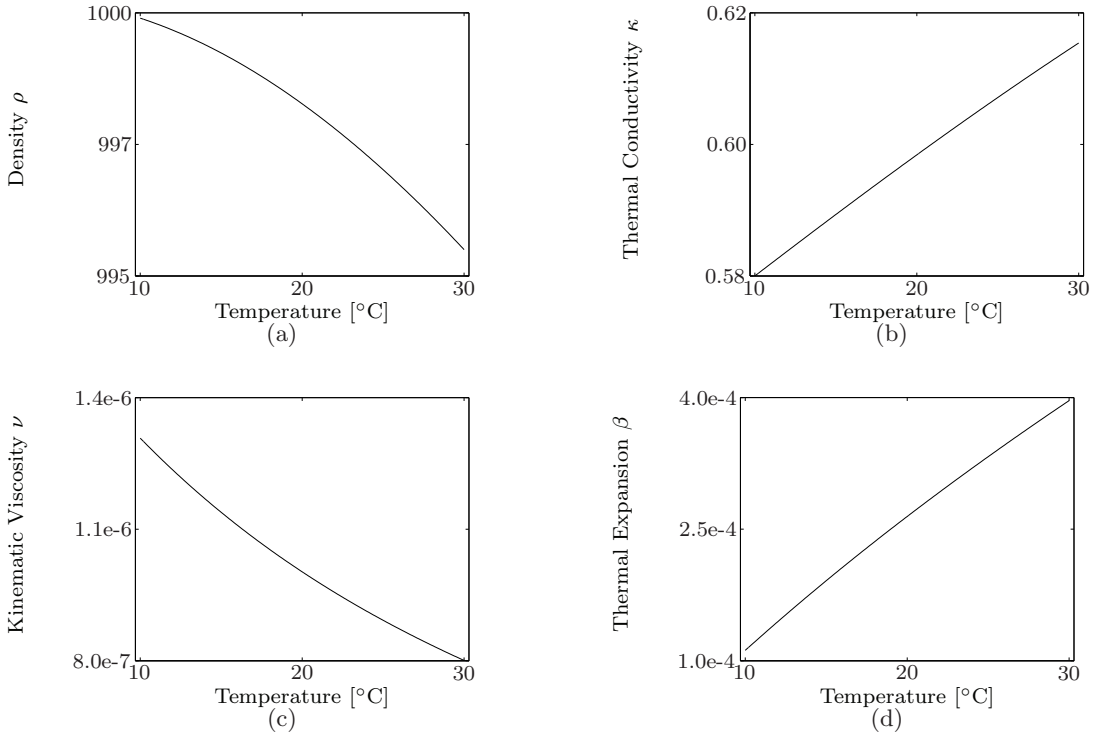

Figure 2.6: Least square fits of some measured thermo-physical properties of saturated distilled water versus temperature in °C. (a) density in kg/m^3 (b) thermal conductivity in W/(m·K) (c) kinematic viscosity in m^2/s (d) volumetric thermal expansion coefficient. Data from [1].

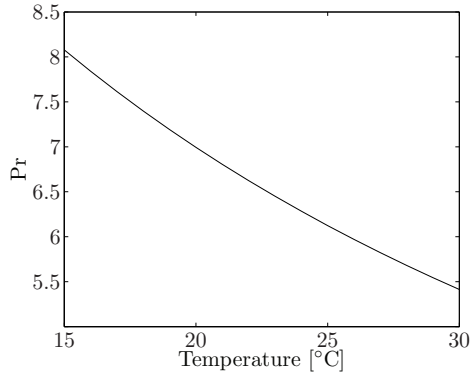

Figure 2.7: Pr vs. temperature for distilled water

White mineral oil The selected high Pr fluid was medical quality white oil from Shell (Ondina 917) which is a mix of several mineral oils and has a Prandtl number of about 450. To get a constant quality, a 200 liter barrel was bought and all experiments were done with this stock. This oil is transparent, non-toxic, non-corrosive, non-degradable, and has a large refractive index gradient with temperature. Data are shown in figure 2.8.

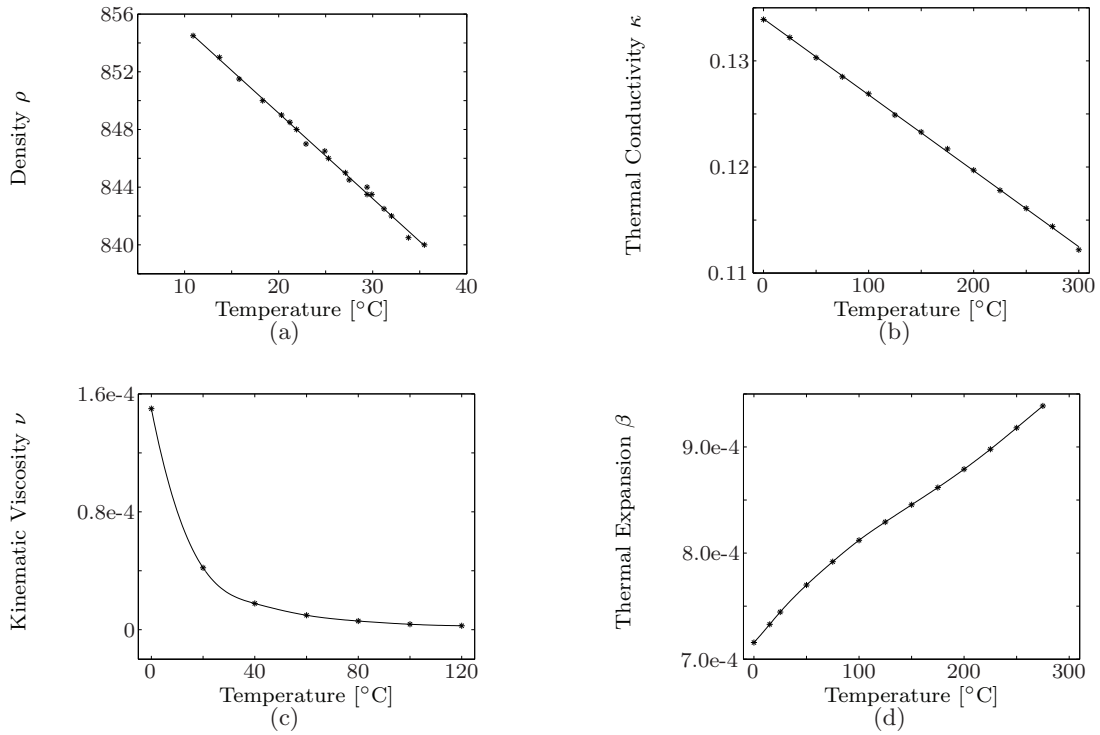

Figure 2.8: Least square fits of some measured thermo-physical properties of Shell Ondina 917 white mineral oil versus temperature in °C. (a) density in kg/m^3 (b) thermal conductivity in W/(m·K) (c) kinematic viscosity in m^2/s (d) volumetric thermal expansion coefficient. Data are a mix between in situ experimental measures and data provided by Shell. They are precise to within 5%.

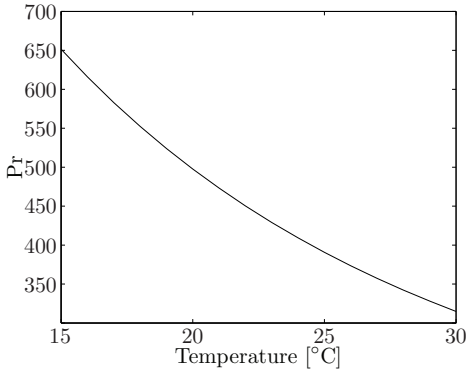

Figure 2.9: Pr vs. temperature for white mineral oil

2.1.1.1 Temperature control

The laboratory temperature and the floating working fluid temperature are subject to variations due to the daily cycle, the weather and the varying heat production of lab equipment. To minimize the heat fluxes into and out of the setup, the temperature of the working fluid in the supply tank was not forced to be constant, but was left floating, i.e. left to slowly respond to environmental forcing. The fastest temperature gradient in the supply tank ever recorded for the cases under consideration in this thesis was 2°C/day. The controlling computer used this floating inlet temperature as a reference and, to produce a desired Rayleigh number, set the temperature of the top and bottom temperature controlled baths symmetrically around this reference. Because of the finite heat conductivity of the borosilicate windows, the temperature difference between the top and bottom boundary of the test section is smaller than the difference between the corresponding temperature controlled baths. Hence, to obtain a desired temperature difference $T_\mathrm{b} - T_\mathrm{u}$ between bottom and top boundaries of the RBP channel, which could not be measured directly in the present setup, the temperature of the two baths was computed with a one-dimensional pure heat conduction model, given by equation (2.4), between the two baths. In addition, the Boussinesq approximation was used in the central fluid layer. Since thermal convection in the test section was neglected, the model is expected to be most accurate at, or near critical conditions. Further away from the onset of convection, this procedure generates a Ra which is systematically larger than the desired Ra (see details in section 2.2.1). At the highest Ra used in the present experiments, the error is estimated at 40%.

Temperature controlled bath To provide a spatially constant temperature difference between both external horizontal surfaces of the channel, water is pumped through the 2 heat exchange baths (ⓑ on figure 2.2) using two separated temperature controlled closed circuits. Each bath is fitted with four fluid inputs and four fluid outputs to minimize head loss and to obtain a more uniform heat transfer over the entire surface.

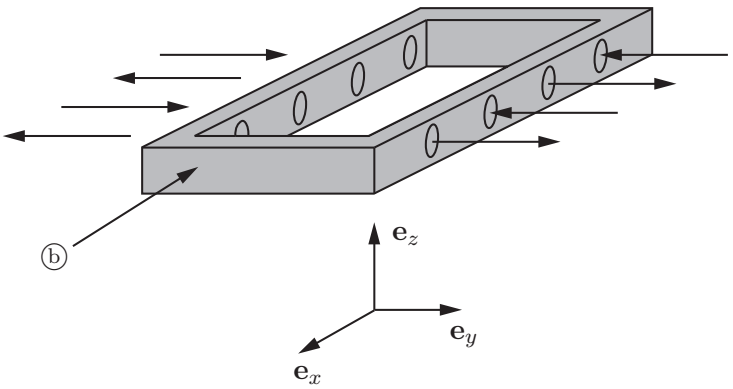

Figure 2.10: Temperature controlled bath, labelled ⓑ in figure 2.4. Each input is fitted with a water column damping system detailed in figure 2.11.

Low frequency pressure pulses from the incoming temperature controlled water circuits are damped by vertical water columns open to the air before every input of both baths. In addition, these water columns were used to equalize the flow rates in the four inlet tubes of each bath. Before implementing these dampers, the pressure pulses from the the Lauda's (see next subsection) were found to be responsible for additional noise in the form of unsteady window deflections. The system is shown in figure 2.11.

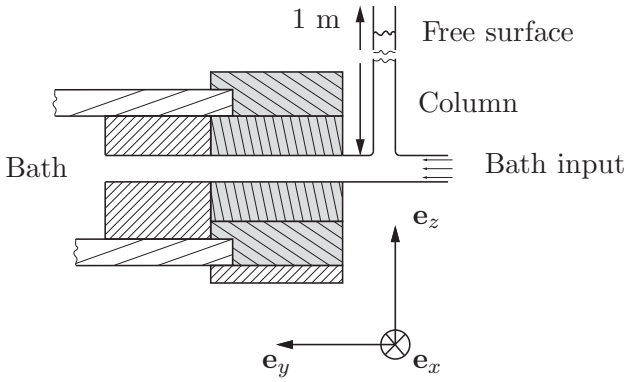

Figure 2.11: Detail of the heating/cooling bath inlets. A 1 m vertical column with an open end is added in series to each bath input to damp low frequency pressure pulses.

"Soft" lateral boundary conditions In early experiments, as soon as thermal convection was initiated anywhere in the test section, the lateral side walls were found to immediately become a source of undesirable longitudinal rolls, presumably in response to the pressure field generated by the growing convection pattern under study. To reduce this effect, "soft" lateral boundary conditions, i.e. a gradual reduction of Ra to subcritical conditions in a narrow strip adjacent to the side walls of the test section as well as its inlet and outlet, were found to be most effective. This was realized by a 20 mm wide plexiglass insert (see ⓕ in figure 2.4 and figure 2.12) around the periphery of both heat transfer baths, which reduces the area of constant temperature in the baths relative to the area of the test section.

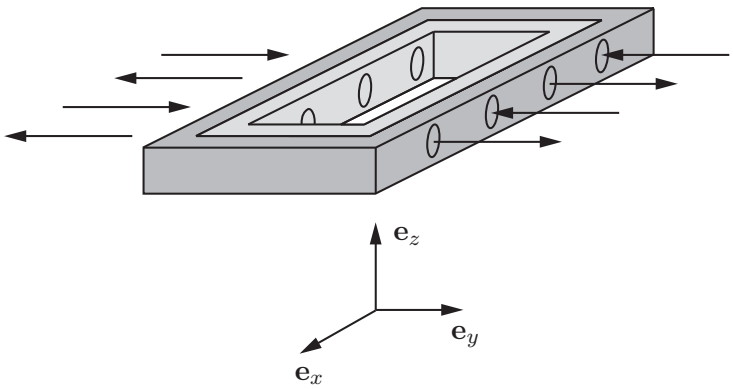

Figure 2.12: The width of the temperature controlled bath ⓑ in figure 2.4) is reduced to produce "soft" temperature boundary conditions.

Lauda thermo regulated water circuit The constant temperature in each circuit is obtained through the use of two Lauda® RK8KP water thermostats. Each circuit consists of a temperature controlled tank containing eight liters of degassed demineralized water. Water circulation is achieved by a double action pump to get a large flow rate of 15 liters per minute at a low relative pressure (~ 0.1 bar just before the heat transfer baths) in the external circuit (see figure 2.13). All external connections are made with 13 mm I.D. hoses to minimize pressure losses and thus to maintain a large flow rate inside the heat transfer baths.

The temperature is internally controlled using a Proportional Integral Derivative controller (PID), which is able to use both heating and cooling power at the same time for maximum

precision. These PIDs are driven by external Resistance Temperature Detectors (RTDs, details are in the following section) fixed at the entrance of each channel bath. The time constant of the regulation is 10 s, which is much less than the smallest time constant for the variation of the reference temperature in the inlet tank of the RBP channel. To check the precision of the temperature measurement, additional temperature probes were mounted at several outflows of the baths in order to verify the set temperatures.

Because of the large flow rate through the heat exchange baths, the temperature difference between the input and the output of both heating and cooling bath was observed to be less than the resolution of the temperature measuring system, i.e. less than 0.2°C.

Heating power max [W]	2000
Cooling power max [W]	800
Maximum flow rate [lpm]	20

Table 2.1: Technical data of the RK8KP Lauda water circulating device. The cooling power is strongly temperature dependant, decreasing with decreasing temperature.

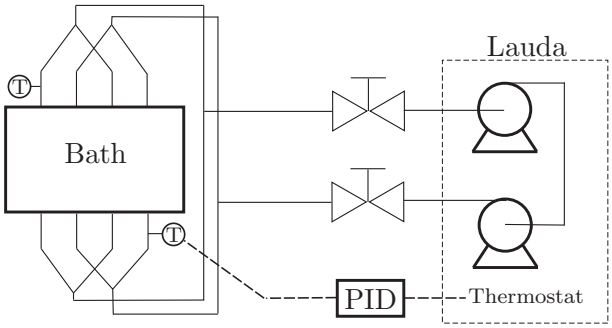

Figure 2.13: Schematic of the temperature control circuit, composed of a Lauda that is regulated using a PID controller.

Temperature probes The temperatures are measured with high precision RTD platinum 3-wire resistance probes, (RTD-NPT-72-E from Omega Engineering Inc.), positioned at several inputs and outputs of the temperature controlled baths. Every probe is encapsulated in a stainless steel fitted mount. Their nominal absolute precision is ± 0.1 K and their nominal repeatability is 0.05 K. Copper extension wires and removable connectors, required for channel disassembly, did reduce this absolute precision to between 0.2 and 0.3 K. We checked the response of the probes inside a melting ice bath and in boiling water at atmospheric pressure. The measurements were compared with the known melting and boiling temperatures at the measured atmospheric pressure and with the temperature measured using a standard mercury thermometer. Results of these comparisons are presented in figure 2.14. Both cooling and heating circuit probes are linked to the Lauda's probe readers, which have a larger sampling than the three other controllers; but are subject to the same measurement errors.

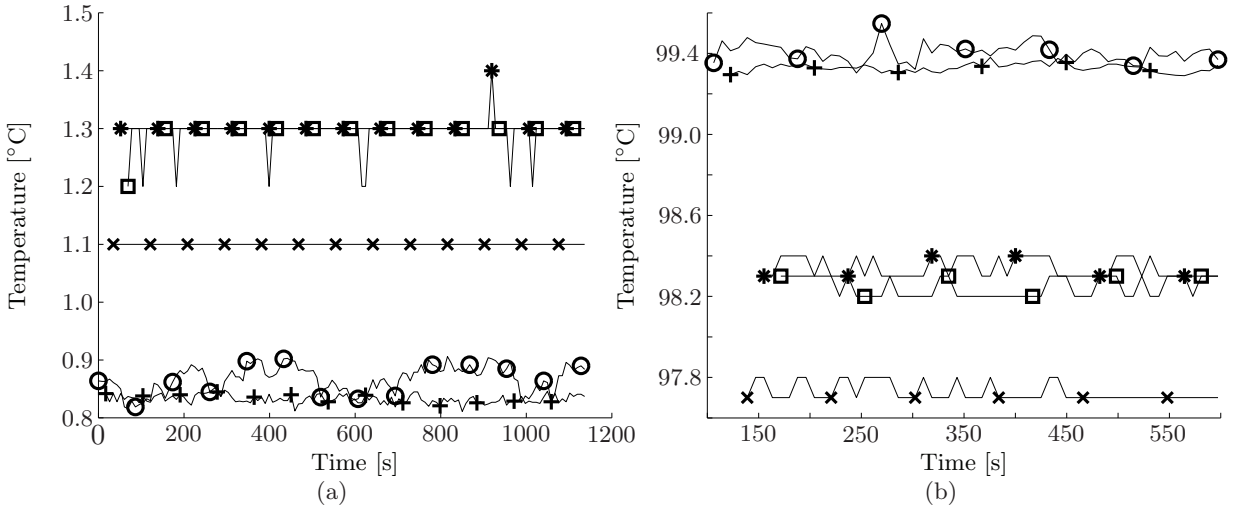

Figure 2.14: Additional temperature probe calibration using (a) melting ice ($\sim 0.5°C$) and (b) boiling water ($\sim 98.8°C$). On both graphs: ($\circ$) is the cooling circuit probe; ($+$) is the heating circuit probe; ($\times$) the input fluid probe and ($*$) and ($\square$) are the output probes positioned at the output of the cooling and heating bath respectively. ($\times$), ($*$) and ($\square$) are obtained from an Omega CNi32 controller with an output resolution of 0.1°C. Each probe is subject to the same error range of $\pm 0.2°C$.

2.1.1.2 Flow system

The Poiseuille flow is generated by a multi-gear pump placed at the output of the channel. Its outflow is connected to a capillary flow meter through a computer controlled continuous electro-valve (model 6022 from Burkert). From the flow meter the working fluid is recirculated into the inlet tank.

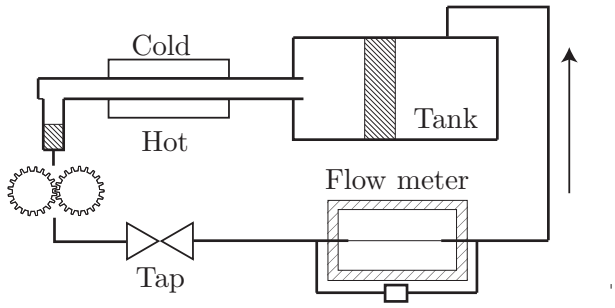

Figure 2.15: Schematic of the working fluid circuit: a feed-back loop coupled with an analog electro-valve is used to control the Reynolds number inside the channel while the Rayleigh number is set through the temperature difference between the heating and the cooling systems.

Pump The pump used to produce the Poiseuille flow was a 3-gear[2] pump manufactured by Micropump® (model GB-P35) and powered by a DC motor. It is complemented with a bypass loop to allow a high operational velocity even for small flow rates in the test section. This high rotational velocity is necessary to avoid pulsations in the flow.

[2]Each gear is manufactured with 8 teeth to get a "pseudo-continuous" flow

All the tubes used for the working fluid circuit are flexible PVC tubes. They are transparent to allow the detection of bubbles in the circuits. Their internal diameter is 10 mm.

Flow meter For precise flow rate measurements, we measure the pressure drop of a Poiseuille flow between both ends of a capillary tube (figure 2.16). The diameter and length of this tube can be adapted to the working fluid viscosity and the desired range of flow rate. The extremities of the tube are linked to a differential diaphragm pressure transducer (model DPI5TL manufactured by Validyne). The capillary tube and its mounts were placed in a temperature controlled water tank.

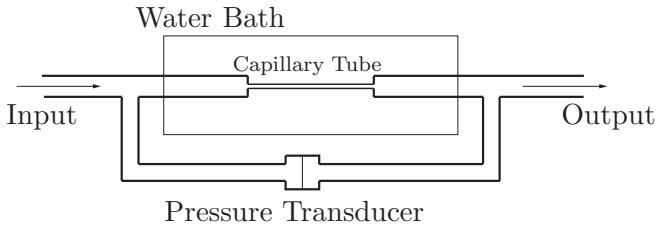

Figure 2.16: Poiseuille flow meter: a differential pressure transducer measures a pressure drop in a capillary tube which is proportional to the flow rate.

Because the inner capillary tube diameter is not accurately known and because of an imprecise transducer calibration provided by the manufacturer the pressure transducer output (analog voltage) has been measured directly as a function of the flow rate which was measured with a digital scale featuring a numerical output. The calibration was done for several temperatures to take viscosity dependency into account. During about 20 minutes the mass of fluid flowing out from the flow meter was sampled five hundred times. The constant slope of the measured mass (i.e. the flow rate trough the flow meter) was calculated for different fixed pressure transducer output voltages and different temperatures in order to obtain the black dots on the calibration graph (2.17). The least square fit for oil is given by equation 2.1 where F, V and T stand for flow rate, voltage and capillary tube temperature respectively.

$$F = 4.8987 \cdot 10^{-3} V - 3.8289 \cdot 10^{-4} T + 1.4573 \cdot 10^{-3} V \cdot T + 1.1738 \cdot 10^{-4} V^2 + 1.5257 \cdot 10^{-5} T^2 \quad (2.1)$$

At the normal flow meter temperature of 22 degrees, the calibration points deviate at most by $2.0 \cdot 10^{-3}$ g/s from the least square fit. Over the entire temperature range, the maximum deviation is increased to $4.0 \cdot 10^{-3}$ g/s. The precision of the flow meter system is better than 5% for slowly varying flow (time constant $> \mathcal{O}$(minute)).

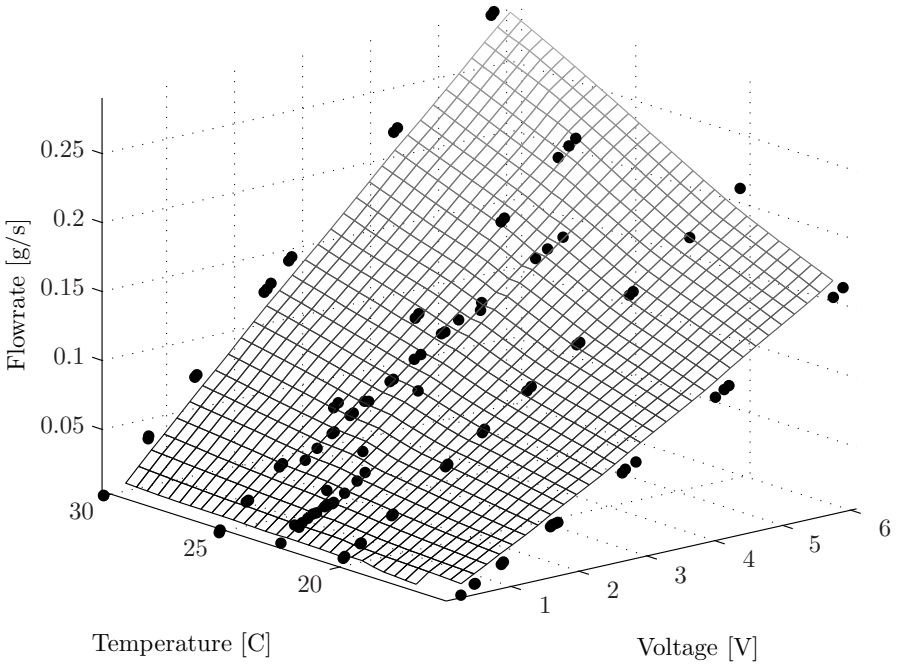

Figure 2.17: Least square fit calibration surface used to deduce the flow rate from the temperature of the flow meter and the analog differential pressure transducer signal. The black dots are measured average flow rates

Active Flow rate control To obtain a constant Reynolds number Re in the channel, an active control system is used: the flow rate and the channel entrance temperature are used to control a continuous electro-valve using a PID scheme. This system is necessary to compensate for the laboratory temperature variations during experiments (day/night/weather). The resulting total uncertainty of Re is estimated to vary according to table 2.2.

	Oil	Water
Low Re	0.001 ± 10 %	0.1 ± 10 %
Medium Re	0.01 ± 5 %	1 ± 5 %
Low Re	0.1 ± 2 %	3 ± 2 %

Table 2.2: Estimated precision on Re for oil and water

2.1.2 Optical Schlieren setup

The whole Schlieren setup is completely decoupled from the channel: the channel is neither attached nor touching the optical setup. This separation not only avoids any vibration transmission but also allows to check the vibration level of the channel.

Light source The light source (manufactured by Spindler & Hoyer) used in our experiment is composed by a short arc (0.6×2.2 mm) mercury vapor bulb (HBO 200 W/4), a two-lens optical condenser (f75/f100), and a parabolic mirror. This lamp is powered by an AC power-supply providing a 100 Hz illumination[3].

At the focal point of the condenser, a diaphragm is used to remove residual aberrations from the condenser lens. The diaphragm serves as the reference point for the alignment of the large parabolic mirror (main parabolic mirror on figure 2.18).

Light path To produce the required parallel beam, the virtual image of the light source is positioned at the focal point of a 300 mm diameter parabolic mirror. This beam is then reflected with a "first surface" mirror into the channel. A second mirror then directs the output beam into the camera through the collection lens (see figure 2.18). To obtain a Schlieren picture (a complete description is given in section 2.2.4), perturbed parts of the beam that do not focus at the same spatial location have to be stopped with a "cutoff" device. Its choice depends on what one wants to visualize:

- The diaphragm of the camera lens can be used as cutoff device. It is perfectly aligned with the camera and allows the observation of convective structures oriented both longitudinally and transversely. Unfortunately, the minimal diameter is limited by the objective design and the resulting contrast is therefore limited. This requires that the focal point of the lens be exactly at the position of the diaphragm of the camera lens.

- A circular pinhole can be mounted before the camera; the main advantage is that the pinhole can have smaller diameter ($\rightarrow$ 200 μm) and still allows the observation of multi-directional gradients.

- When the perturbations due to convective structures are weak, i.e. of the same order as the system noise, a circular blocking device is inefficient. A razor blade is used instead as a single direction cutoff device.

These modifications of the standard Z–type Schlieren assembly [60] were necessary because the channel has to be observed with a vertical beam; a Z–type assembly is designed for a single plane system. This 3-D assembly also allows the lamp to be positioned far enough to avoid it heating the system, or sending a plume of hot air through the optical path.

Camera A standard 8-bit CCD camera (model A301 manufactured by Basler®)was used. This fire-wire camera is able to provide 80 uninterpolated 654×494 pixel frames per second. To get constant illumination, the camera is externally trigged by the power network through a pulse delay generator. The latter is used for fine tuning the electronic shutter timing. A C-mount to F-mount adapter permitted the use of a high quality 24 mm Nikor® objective.

[3] the 50 Hz standard power network provides a 100 Hz illumination through two symmetric power pulses per period.

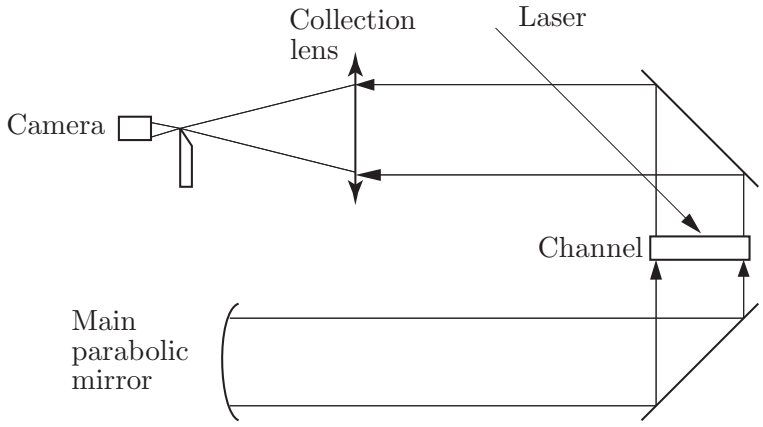

Figure 2.18: Light path used in the RBP experiment. On this schematic, the light source is not shown for clarity. The arrow called "Laser" is the last segment of the trajectory of the pulse used to produce the hot spot, see section 2.1.3.

2.1.3 Hot spot for the experimental determination of the impulse response

To produce an experimental temporally and spatially localized hot pulse[4] on the bottom surface of the test section, a continuous Ar-ion laser was aimed via two mirrors at a black target on the bottom channel wall during 15 to 30 seconds. This pulse contained all laser wavelengths and the total power output of the laser ranged between 0.8 and 2.6 W. The pulse target was a 5 mm diameter black dot painted on the lower surface of the channel. This dot was obtained using a stencil technique with heat resistant paint in order to get a "pseudo-Gaussian" distribution of the paint thickness with a maximum thickness of 10 to 15 μm. The cubic dependency of the Rayleigh number on the channel height implies a local increase of the Ra of about 20 to 50 at the dot center, depending on the maximum dot thickness.

[4] A temporally and spatially localized hot pulse is an experimental approximation of a Dirac function.

2.1.4 Differential heating

Differential heating is produced with a spatially non-uniform thermal resistance placed against the external side of the lower glass plate bounding the channel. Practically, a 4 mm thick Plexiglas plate (called ⓗ in figure 2.19) with a cutout is added in the hot bath and held against the bottom window of the RBP channel by grooved soft walls. During the assembly, a couple of water drops were deposited one the Plexiglas prior to its application against the channel window in order to obtain a good optical contact even in the case of heating water infiltration. At every assembly, we use the Plexiglass plate flatness imperfection as a spring to increase the contact quality against the channel window.

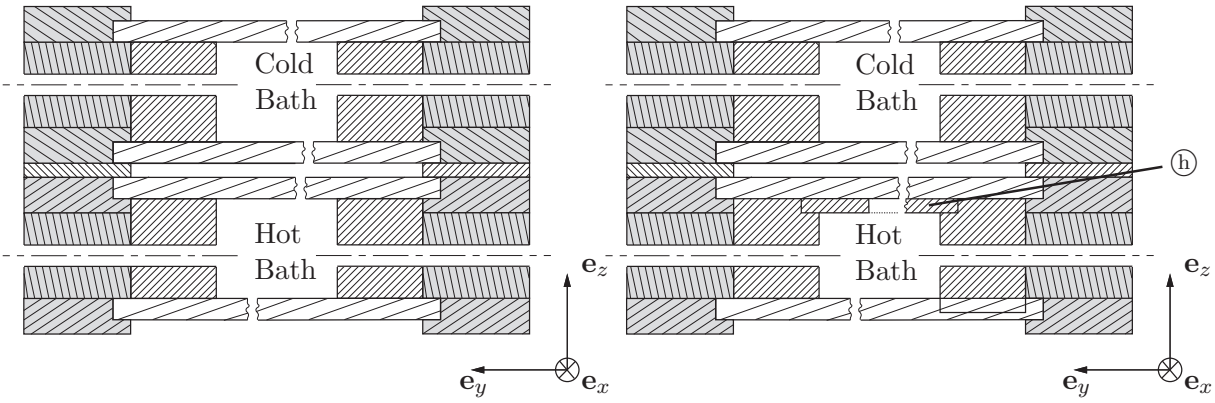

(a) Channel without additional thermal resistance

(b) Channel with additional thermal resistance ⓗ with screen covered hole for locally increased heat transfer

Figure 2.19: Transverse channel cross-section ($\mathbf{e}_y$ - $\mathbf{e}_z$ vertical spanwise plane). ⓗ is the thermal resistance plate

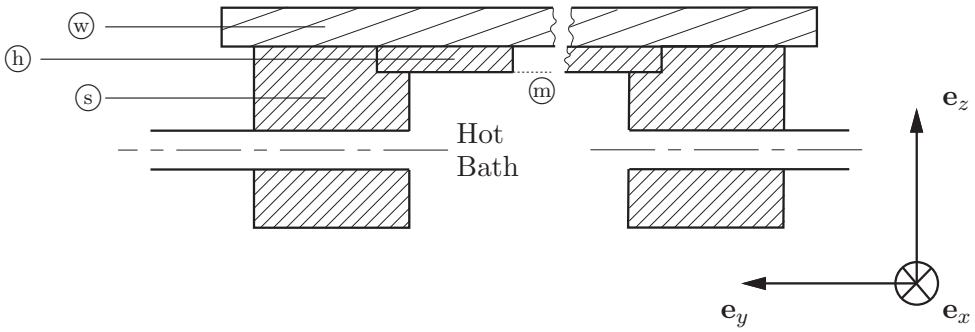

Figure 2.20: Detailed view of the lower part of the channel; ⓦ: lower channel window, ⓢ: soft wall, ⓗ: additional thermal resistance and ⓜ: mosquito net to avoid flow in the cutout of ⓗ.

To obtain the desired temperature profiles in the shape of a hot spot, appropriately shaped cutouts were provided in this plexiglass plate where hot water could enter into direct contact with the bottom glass window of the channel. Motivated by the theoretical studies of Martinand *et al.* [36] and [37], two different shapes were used:

- A circular hole of 40 mm of diameter,
- A rectangle of 15×50 mm with short edges rounded, tilted by 45° with respect to $\mathbf{e}_x$.

To avoid water flow and in particular flow separation within the cutouts of the Plexiglas plate, a thin mosquito net was stretched across the cutout of the Plexiglas plate (on the heating bath side). This screen was found to be effective in creating a layer of essentially stagnant fluid within the cutout so that the shape of the resulting hot spot corresponded well with the geometric shape of the cutout.

2.2 Experimental procedure

2.2.1 Determination of Rayleigh number

Since the flow channel requires full optical access for the observation of roll patterns (see section 2.1.2), the top and bottom of the channel are made from borosilicate glass which has a relatively low thermal conductivity. Therefore, the temperature difference T_u - T_b applied to the fluid layer has to be computed from the applied bath temperatures T_hot and T_cold.

In our experiment, the Rayleigh number Ra is always defined assuming a non-thermo-convective state. It is based on the temperature difference between the channel upper surface temperature T_u and the channel lower surface temperature T_b. The thermo-physical properties of the working fluid are based on the mean temperature T_mean which is maintained close to the working fluid temperature at the entrance of the channel (details on temperature control can be found in 2.1.1.1).

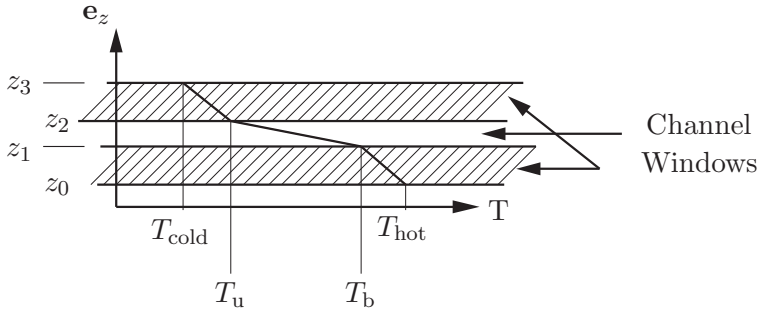

Figure 2.21: Temperature profile in the channel for a no-convection case; the upper and lower boundaries are subjected to perfect cooling and heating conditions, respectively. (Gravity $\boldsymbol{g}$ is in $-\mathbf{e}_z$ direction).

To get the temperatures T_b and T_u inside the channel, we use the energy flux equation per surface unit; the energy flux through the system q_z is constant, (no heat production inside the channel):

$$q_z = \left(\frac{T_\mathrm{hot} - T_\mathrm{b}}{z_1 - z_0}\right)\kappa_\mathrm{w} = \left(\frac{T_\mathrm{b} - T_\mathrm{u}}{z_2 - z_1}\right)\kappa_\mathrm{f} = \left(\frac{T_\mathrm{u} - T_\mathrm{cold}}{z_3 - z_2}\right)\kappa_\mathrm{w} \tag{2.2}$$

where κ is the thermal conductivity of the medium (the subscript w stands for window and f for fluid).

$$T_\mathrm{b} = \frac{T_\mathrm{hot}(\kappa_\mathrm{w}(z_1 - z_2) + \kappa_\mathrm{f}(z_2 - z_3)) + T_\mathrm{cold}\kappa_\mathrm{f}(-z_1 + z_0)}{\kappa_\mathrm{f}(z_0 + z_2 - z_1 - z_3) + \kappa_\mathrm{w}(z_1 - z_2)} \tag{2.3}$$

$$T_\mathrm{u} = \frac{T_\mathrm{cold}(\kappa_\mathrm{w}(z_1 - z_2) + \kappa_\mathrm{f}(z_0 - z_1)) + T_\mathrm{hot}\kappa_\mathrm{f}(z_2 - z_3)}{\kappa_\mathrm{f}(z_0 + z_2 - z_1 - z_3) + \kappa_\mathrm{w}(z_1 - z_2)} \tag{2.4}$$

Using equation 1.1, the experimental definition of Ra is given by:

$$\mathrm{Ra} = \frac{g\beta(T_{\mathrm{mean}})(T_{\mathrm{u}} - T_{\mathrm{b}})d^3}{\nu(T_{\mathrm{mean}})\alpha(T_{\mathrm{mean}})} \tag{2.5}$$

The temporal evolution of the system subjected to a sudden Ra increase is presented in figure 2.22 for the two working fluids used in the channel. These results were computed with a finite element commercial code for a 2D case with periodic boundaries applied on each lateral side. After a hundred seconds, the final steady state profiles are almost established. Therefore, a temperature control with a time constant faster than $5 \cdot 10^{-3}$ Hz is clearly useless where the (long) time constant of the Lauda's is not even taken into account. For this reason only the temperature difference, and not Ra, is kept constant relative to the inlet tank temperature. Trying to keep Ra constant in the channel with a PID controller using such a slow response was deemed too sensitive to controller instabilities.

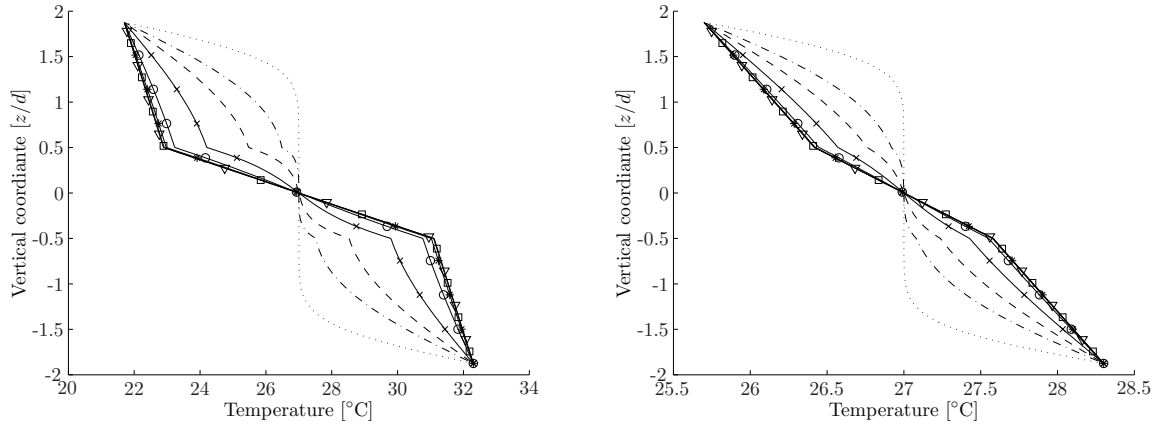

(a) Working fluid: Oil (b) Working fluid: Water

Figure 2.22: Simulated temporal evolution of the temperature profile for oil (a) and for water (b) between infinite perfect cooling and heating boundaries (water baths) subject to a sudden Ra step from 0 to about 1400 with no-thermo-convection regime assumptions : "." after 1 s, ".-" after 5 s "- -" after 10 s, "×" after 20 s, "○" after 40 s, "∗" after 60 s, "□" after 80 s and "▽" after 100 s.

Rayleigh number corrected for convection The previous Ra computation does not take convection into account in the working fluid heat conductivity: a pure conductive state is always assumed, even for supercritical state. However, when Ra is larger than $\mathrm{Ra_c}$, the fluid heat conductivity increased is given by the Nusselt number Nu:

$$\mathrm{Nu} = \frac{\text{Convective heat transfer}}{\text{Conductive heat transfer}} \tag{2.6}$$

Nu is equal to one while Ra is smaller than $\mathrm{Ra_c}$; then it is increasing with $\mathrm{Ra} - \mathrm{Ra_c}$. Because the heat flux through the present channel cannot be measured, the deviation is computed using the Nu measurement by Silveston (1958) [61] for water (see figure 2.23).

Using the data of figure 2.23, one can deduce a corrected heat conductivity coefficient $\widetilde{\kappa_{\mathrm{f}}} = \widetilde{\kappa_{\mathrm{f}}}(T_{\mathrm{b}} - T_{\mathrm{u}})$:

$$\widetilde{\kappa_{\mathrm{f}}} \equiv \kappa_{\mathrm{f}} \cdot \mathrm{Nu}$$

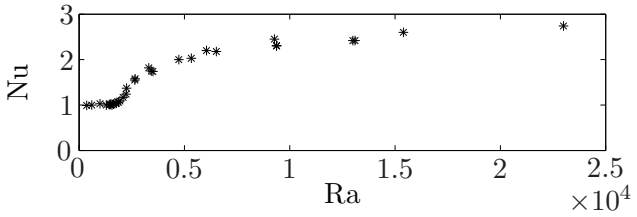

Figure 2.23: Experimental Nusselt number for water measured by Silveston [61]. The author estimates the errors to be ±50 on Ra.

where Nu can be approximated for Ra slightly above $\mathrm{Ra_c}$ by:

$$\mathrm{Nu} \approx 2.144 \exp\{1.193 \cdot 10^{-5}(\mathrm{Ra} - \mathrm{Ra_c})\} - 1.181 \exp\{-0.0006076(\mathrm{Ra} - \mathrm{Ra_c})\}$$

This new heat conductivity $\widetilde{\kappa_\mathrm{f}}$ is introduced into the heat flux equation 2.2:

$$q_z = \left(\frac{T_\mathrm{hot} - T_\mathrm{b}}{z_1 - z_0}\right)\kappa_\mathrm{w} = \left(\frac{T_\mathrm{b} - T_\mathrm{u}}{z_2 - z_1}\right)\widetilde{\kappa_\mathrm{f}} = \left(\frac{T_\mathrm{u} - T_\mathrm{cold}}{z_3 - z_2}\right)\kappa_\mathrm{w} \tag{2.7}$$

This system is solved numerically for out channel dimensions and thermal parameters. The results are presented in figure 2.24:

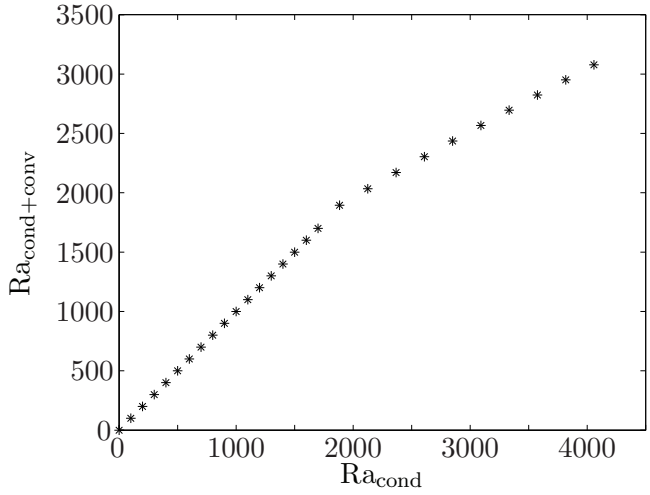

Figure 2.24: Thermal conduction effects on Ra observed with water for a pure RB case: on the x-axis we have Ra computed without convection (equation 2.2) and on the y-axis we have Ra computed considering both conduction and convection (equation 2.7). The non perfect matching at the critical point ($\mathrm{Ra_c} = 1708$) is due to the errors on the experimental Nusselt measurements.

In spite of the precision increase, this method for computing the temperature difference needed to calculate a certain Ra cannot be applied in a general way in the present work because of the lack of a known Nusselt number as soon as Re becomes larger than zero. Moreover it is not absolutely necessary while we are interested in the onset of the thermo-convection (i.e. the first appearance of thermo-convective structures, corresponding to results in section 3.1.1) and in system states close to onset, where the difference between $\mathrm{Ra_{cond}}$ and $\mathrm{Ra_{cond+conv}}$ stays small.

2.2.2 Determination of Reynolds number

For the experimental determination of the Reynolds number Re we use the mean speed of the Poiseuille flow U_{mean} deduced from the flow rate Q and the dimensions of the channel. As for Ra, we use the mean temperature T_{mean} as the reference temperature for the fluid viscosity.

In a horizontal channel of rectangular section ($-l/2 \leq y \leq l/2, -d/2 \leq z \leq d/2$) the flowrate Q and the velocity profile u of a Poiseuille flow are given by (details are available in [67]):

$$Q = \frac{(d/2)(l/2)^3}{6\mu}\left(-\frac{\mathrm{d}p}{\mathrm{d}x}\right)\left[1 - \frac{192(l/2)}{\pi^5(d/2)}\sum_{i=1,3,5,\ldots}^{\infty}\frac{\tanh(i\pi(d/2)/l)}{i^5}\right] \tag{2.8}$$

$$\Rightarrow U_{\text{mean}} = \frac{Q}{\text{Channel section}}$$

$$u\,(y,z) = \frac{16(l/2)^2}{\mu\pi^3}\left(-\frac{\mathrm{d}p}{\mathrm{d}x}\right)\sum_{i=1,3,5,\ldots}^{\infty}(-1)^{(i-1)/2}\left[1 - \frac{\cosh(i\pi z/l)}{\cosh(i\pi(d/2)/l)}\right]\frac{\cos(i\pi y/l)}{i^3}, \tag{2.9}$$

where μ is the dynamic viscosity of the working fluid which is taken at the inlet tank temperature. Equation (2.9) provides a ratio of about 1.52 between $U_{\max}$ and U_{mean} for the present transverse aspect ratio of 42.5. For comparison, the ratio between $U_{\max}$ and U_{mean} is equal to 2 in a circular pipe.

$$\text{Re} = \frac{U_{\max}d}{\nu} = \frac{1.52U_{\text{mean}}d}{\nu(T_{\text{mean}})} \tag{2.10}$$

Using oil as the working fluid, a Re of 0.02 corresponds to an average speed of 0.2 mm/s; while for water the same velocity corresponds to a Re of 1.

2.2.3 Determination of Prandtl number

To be consistent with the Boussinesq approximation used elsewhere, the experimental Prandtl number Pr is evaluated with the kinematic viscosity ν and thermal diffusivity α at the mean fluid temperature T_{mean}.

$$\text{Pr} = \frac{\nu(T_{\text{mean}})}{\alpha(T_{\text{mean}})} \tag{2.11}$$

2.2.4 Shadowgraph and Schlieren observation methods

Two observation methods have been used: the shadowgraph and the Schlieren method [60] illustrated in figure 2.25 by images of the same sample convection pattern. They were obtained in the actual RBP channel with the modified "Z-type" Schlieren system described in section 2.1.2.

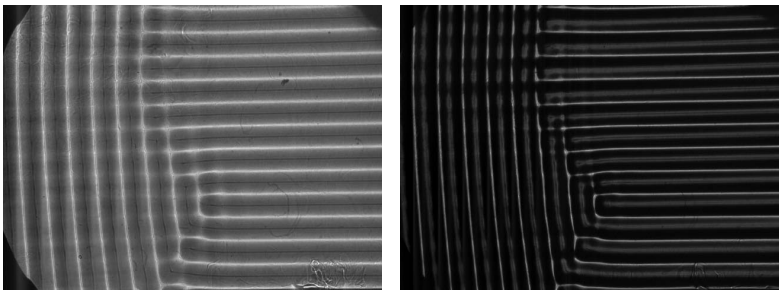

(a) Shadowgraph (b) Schlieren

Figure 2.25: Visualization of a sample convection pattern by (a) the shadowgraph method, showing the second derivative of the refractive index, and (b) the Schlieren method, showing the first derivative of the refractive index. A high Ra number (at least $1.5\mathrm{Ra_c}$ in oil) is necessary to get such well defined results.

Both methods rely on the same physical fluid property, the variation of the refractive index n with temperature. For our working fluids, the temperature variation of the refractive index is shown in figure 2.26. In the following, n is assumed independent of the wavelength of the light and well approximated by:

$$n_{wa}(T) = -1.154 \cdot 10^{-4}\, T + 1.3353 \quad \text{for water,} \tag{2.12}$$

$$n_{oi}(T) = -4.085 \cdot 10^{-4}\, T + 1.4756 \quad \text{for oil.} \tag{2.13}$$

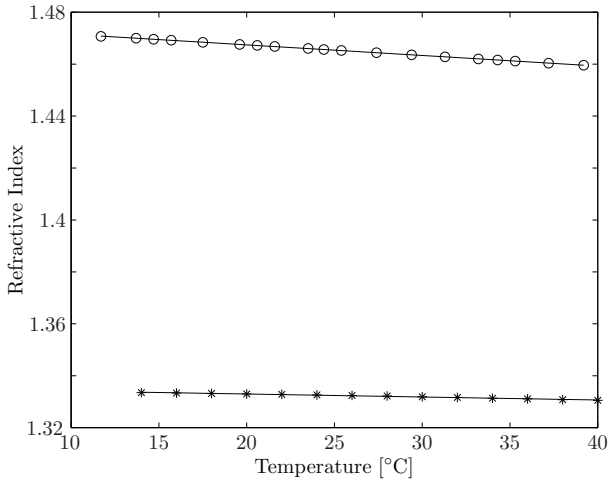

Figure 2.26: Refractive index of water "$*$" and of Shell Ondina 917 "$\circ$"; both measured for $\lambda = 589.3$ nanometers. The refractive index variation with temperature (i.e. the slope of the least-square linear fits) for the oil is about 4 times larger than that of water.

The two methods differ by the quantity visualized: while the shadowgraph image shows the second derivative of the refractive index variation, the Schlieren image corresponds to its first derivative (see section 2 of [60]). To better illustrate this, the deviation of parallel light rays traversing an idealized 2-D pair of convection rolls, represented by its index of refraction field, has been computed with the finite element commercial code Comsol. An example is shown in figure 2.27. Note that on this figure, the density of the light rays exiting the convection layer on top corresponds to the light intensity recorded on a shadowgram. By adding a beam cutting device at the focal point of the output lens, one removes the perturbed fraction of the output rays which amounts to observing only the derivative of the shadowgraph image, called a Schlieren image.

For all the experiments with oil, the beam cutting device was a circular pinhole to detect both the longitudinal and the transverse rolls. As the refractive index variations with temperature are significantly smaller in water, the pinhole diameter had to be so small to obtain a sufficient contrast that it blocked not only the perturbed part of the beam but also intrinsic beam deviations due to system imprecision. To circumvent this difficulty, a razor blade edge was used as beam cutting device for the water experiments, which restricted the observation to rolls parallel to the blade edge, i.e. index of refraction gradients normal to the edge.

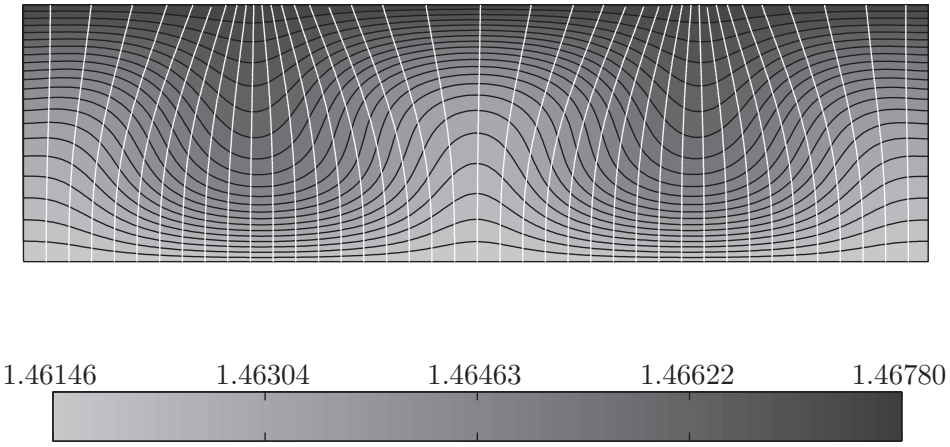

Figure 2.27: Simulated light rays (gray lines) through a pair of 2D RB convection rolls. The working fluid is mineral oil with $T_\mathrm{b} = 34.7°\mathrm{C}$ and $T_\mathrm{u} = 19.0°\mathrm{C}$ (Ra = 2300). The gray scale indicates the variation of the refractive index. The light beam deformation had been computed based on a refractive index variation 150 times larger for visualization purpose. The difference between the rising (light plume) and the falling (dark plume) allows the identification of roll pairs (one wavelength of the roll pattern) in figure 2.25(b).

2.2.5 Acquisition program

The Ra, Re, and camera are controlled by several Labview® codes running in multithread[5] mode. All these codes are included in the main control program for the experiment. Even though the fire wire bus allows asynchronous data transfer, the precision on the timing of image acquisition is of the order of one second in the present code, which is sufficient, and saves CPU resources for other tasks. In case the acquired pictures are too noisy, the code also allows to acquire 5 consecutive pictures at a rate of 50Hz which are then averaged.

2.3 Validation of the base flow and boundary conditions

2.3.1 Poiseuille flow

In order to check the quality of the Poiseuille flow in the channel Particle Image Velocimetry (PIV) measurements were performed at $\mathrm{Ra} = 0$, i.e. without thermo-convective structures. The working fluid was seeded with particles of 5 μm average diameter. A laser sheet was aimed into the channel (without heating/cooling baths) in such a way to obtain a light sheet in the working section that was parallel to $\mathbf{e}_x$ and inclined 45° with respect to $\mathbf{e}_z$[6]. The camera was positioned with the same method to observe this sheet under an angle of $-45°$ with respect to $\mathbf{e}_z$ as shown in figure 2.28.

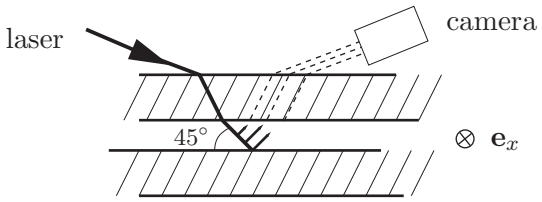

Figure 2.28: PIV measurement setup. The solid and broken lines indicate the laser sheet and the recording light path, respectively.

Data processing was done with the open source MatPIV code [64] using multi pass mode and interrogation windows of 16 × 16 px. A mapping function was used to correct for the optical distortion of the images. Results are presented in figure 2.29(a) for the velocity profile in the vertical plane and 2.29(b) for the horizontal plane. Both profiles are measured at mid channel, i.e. mid-span, for the vertical and mid height for the horizontal profile. These experimental measurements were non-dimensionalized with the maximum value of the theoretical velocity profile obtained from the flow rate and the channel cross section. The results are found to be in excellent agreement with the theoretical Poiseuille profile.

[5]Multi-thread mode is a pseudo time-simultaneous way of running multiple programs through time-slices.

[6]The laser was aimed at the channel at a computed external angle in order to compensate for the refraction through the upper window

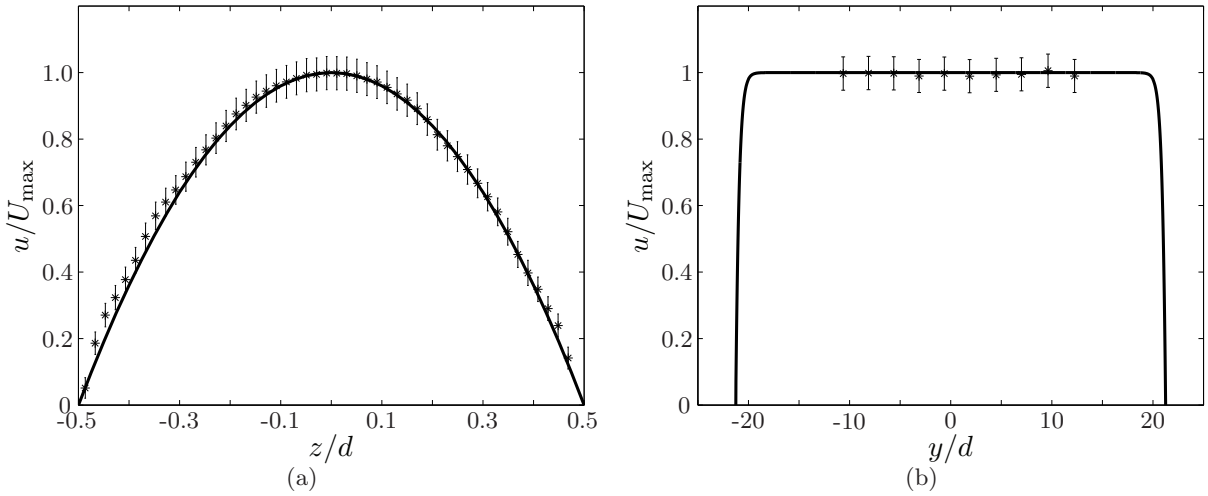

Figure 2.29: (a) Stream wise vertical and (b) spanwise horizontal velocity profiles at mid channel. The solid lines are the theoretical profiles obtained from the measured flow rate, while the stars are PIV measurements.

2.3.2 Characterization of the slowly varying temperature profiles

The temperature distribution of the lower surface of the test section was investigated with Thermo-Chromic Liquid Crystal (TLC) sheets for both "hot spot" shapes presented in section 2.1.4. Uniform illumination was obtained with 4 portable neon lights longer than the channel windows and placed in pairs on each side of a color CCD camera. The calibration was completed by taking pictures of the TLC sheet with both heating and cooling baths set at the same temperature. The calibrated temperature range covers 18 to 30 °C by step of 0.5 °C. The calibration was performed independently for each of the 3 CCD colors which allowed us to extend the range of the TLC sheet relative to its nominal temperature range.

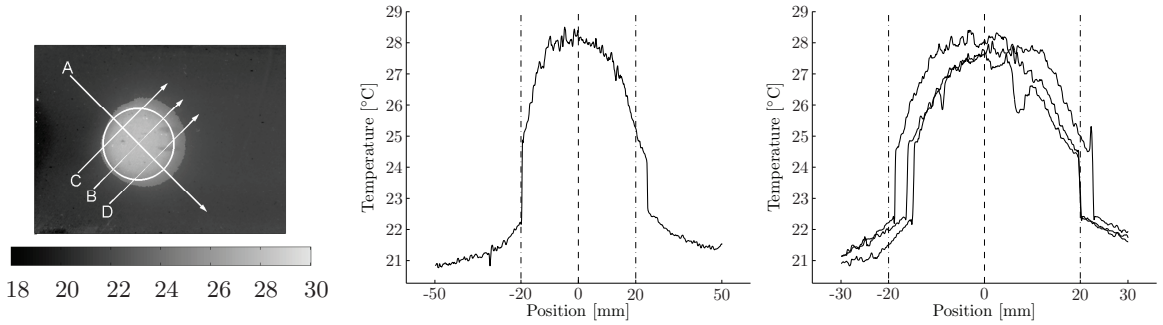

(a) Re = 0 Ra = 1658 (b) Profile along the A vector (c) Profile along the B, C and D vectors

Figure 2.30: Experimental analysis of the temperature profile produced by the 40 mm circular hole in the Plexiglas plate using TLC. (a) Temperature map computed pixel-by-pixel from TLC calibration curve; (b) and (c) are temperature profiles above the hole along the vectors indicated in part (a) of the figure.

Several temperature profiles along different directions are presented in figures 2.30 and 2.31. The difference in background color between figures 2.30(a) and 2.31(a) is due to a change of

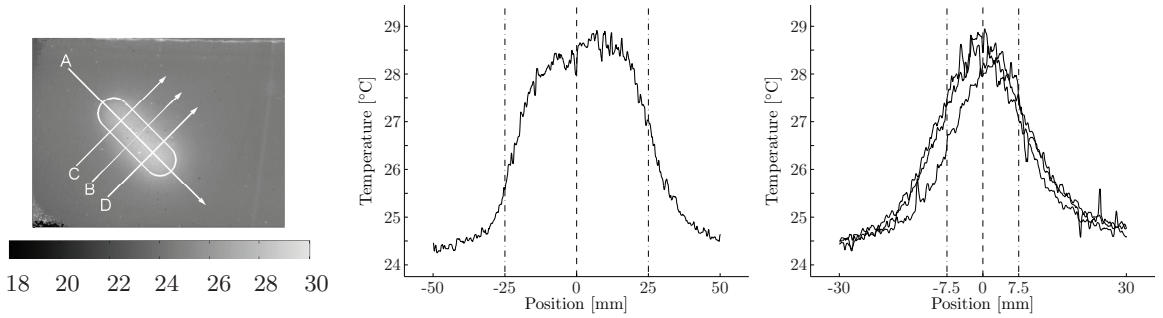

(a) Re = 0 Ra = 1690 (b) Profile along the A vector (c) Profile along the B, C and D vectors

Figure 2.31: Experimental analysis of the temperature profile produced by the 15×50 mm slanted oblong cutout in the Plexiglas plate using TLC.(a) Temperature map computed pixel-by-pixel from TLC calibration curve; (b) and (c) are temperature profiles in various directions above the hollow cavity.

reference (i.e. laboratory) temperature between these two measurements. On these figures, dash-dotted lines represent the geometry of the cutout in the thermal resistance plate. The shapes of these localized heated areas are comparable with the ones used in the computations of Martinand *et al.* in [36] and [37] (see also section 1.6).

Figure 2.32, finally, documents the influence of the the flow rate on the wall temperature distributions of figures 2.30 and 2.31 obtained for oil at no flow. To prepare the comparison with previous theoretical and numerical work, the locally absolutely unstable region where $\mathrm{Ra} > \mathrm{Ra}_{conv-abso,theory}$ in the experimental "hot spots" has been evaluated from the TLC data at different Re for both working fluids. These regions are collected in figure 2.33.

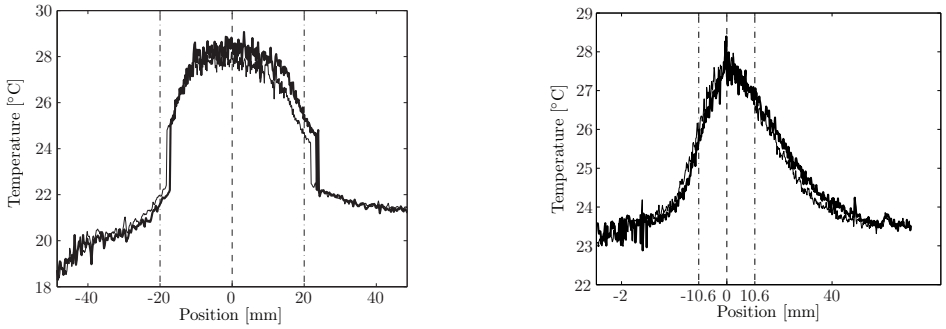

(a) Circular hole (b) Rectangular hole

Figure 2.32: Temperature profile along line "A" of figures 2.30 and 2.31 for two different Re in oil (Pr ≈ 450 and Ra ≈ 1680). (a) circular hole: the slender line is for Re = 0 while the bold line is for Re = 0.01. The upstream (left) shift is about 0.97 mm while the downstream (right) shift is about 2.33 mm; (b) rectangular hole: the slender line is for Re = 0.001 while the bold line is for Re = 0.023. The upstream (left) shift is about 1.8 mm while the downstream (right) shift is about 2.0 mm.

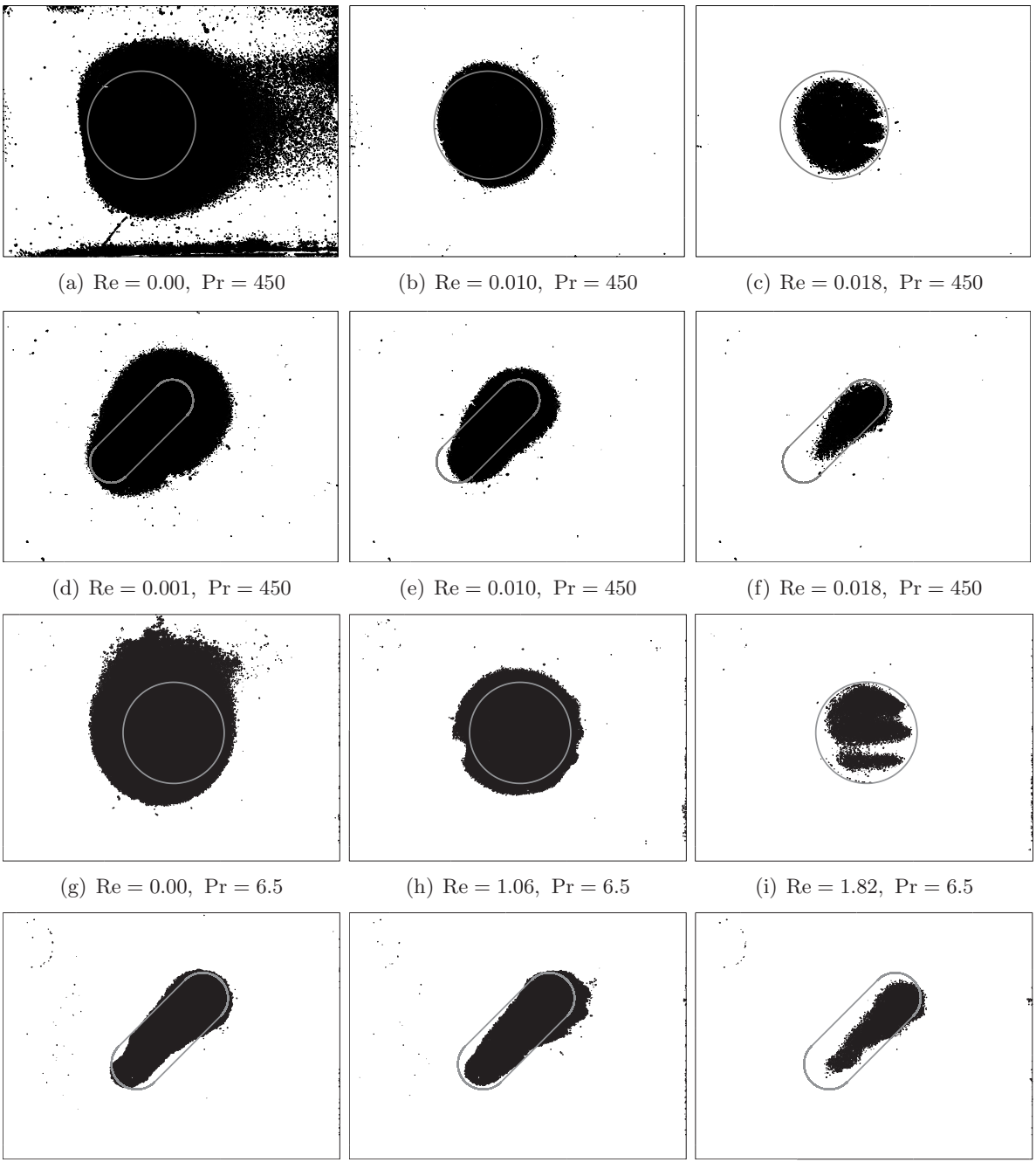

(a) Re = 0.00, Pr = 450 (b) Re = 0.010, Pr = 450 (c) Re = 0.018, Pr = 450

(d) Re = 0.001, Pr = 450 (e) Re = 0.010, Pr = 450 (f) Re = 0.018, Pr = 450

(g) Re = 0.00, Pr = 6.5 (h) Re = 1.06, Pr = 6.5 (i) Re = 1.82, Pr = 6.5

(j) Re = 0.00, Pr = 6.5 (k) Re = 1.06, Pr = 6.5 (l) Re = 1.82, Pr = 6.5

Figure 2.33: Absolutely unstable area for several localized heating configurations.

2.3.3 Sources of errors

As in any experimental system, the control parameters (Ra, Re, Pr) and the geometry are only known with limited precision, while external "noise" is mostly unknown. In the following some of the uncertainties are discussed in more detail.

Heat transfer perturbations by dust As already mentioned, some dust deposits on the lower heated channel wall was unavoidable as the present system could not be completely sealed. It was observed that dust particles could lead to the premature formation of local convection, especially at subcritical conditions. An example is shown in figure 2.34 on which the black painted target used for the impulse response experiment is also seen to act as a trigger of thermo-convective structures. In critical experiments, these dust-induced structures can however, for a non-zero flow velocity, be separated from the moving structures of interest and be eliminated because they are tied to the stationary dust particles (indicated by the arrows in figure 2.34).

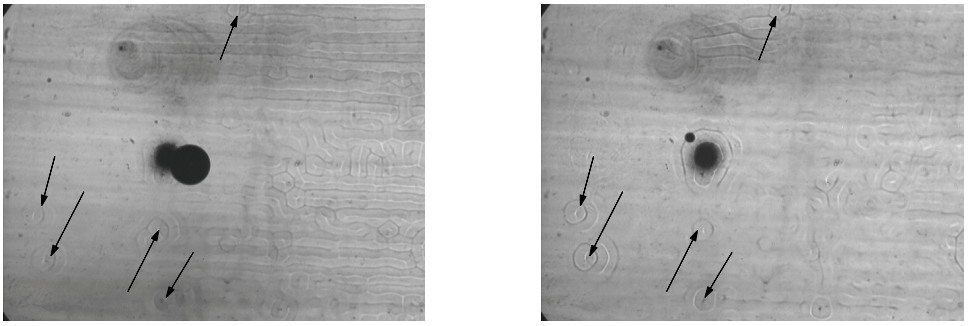

Figure 2.34: Dust destabilization effects: On two different runs, subcritical local thermo-convective structures appear at the same position due to dust particles deposited on the bottom channel wall. On both pictures, the arrows are at the same positions

Vibrations Everything has been done to minimize the level of vibrations in the system. Unfortunately vibrations transmitted to the channel by the pumping system and by the heating/cooling water circulation system cannot be completely suppressed and is thought to be mainly responsible for the generation of convective longitudinal rolls.

Spatial dimensions In order to allow the borosilicate windows to deform in response to varying temperature they are fixed in the brass frame with soft silicone joints. While the thickness variation of the windows due to thermal expansion is negligible, the channel height d can vary due to bending deformations as there is no guarantee that both windows deform in the same way. Taking a temperature difference of 2°C between inlet and outlet, which is typical for our experiments, and assuming the worst case where the four corners of the glass plate cannot move in the brass frame, the window deformation has been computed with a standard finite element code. The result is shown in figure 2.35. The maximum deformation for this example is about 13 μm, which produces a 0.65% variation in d if both windows deform in opposite directions and hence a 2% change in Ra. This example is thought to provide a realistic (rather conservative) estimate of the uncertainty of Ra due to deformations of the channel geometry.

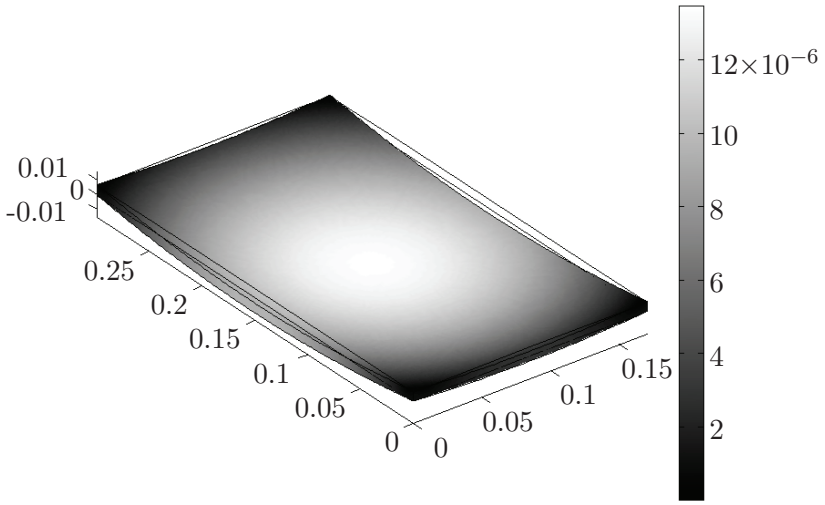

Figure 2.35: Finite element simulation of window deformation due to a temperature difference of 2°C between the inlet and outlet end of the brass frame (this value is typical for our experimental cases) with all four lower corners fixed (dimensions are in [m]). The plotted deformed window amplitude is multiplied by 1000 for visualization purposes.

Temperature The temperature inside the channel is one of the key control parameters of the experiment: a variation of 1°C in the baths (±0.5°C in each bath) represents a Ra variation of about 100 for the present experiments.

Several thermal effects contribute to errors of Ra:

- The calculation of Ra is based on a continuous temperature profile, thermal contact conductance between windows and fluid has been neglected.
- Each heating/cooling surface is assumed to be maintained at the same temperatures, except in the experiments with "hot spot".
- The calculation of Ra according to equation 2.5 assumes pure conduction which generates a systematic error already discussed in section 2.2.1.

Finally, the comparison with theoretical work using the "standard" condition of vanishing temperature perturbations on both lower and upper boundaries is complicated by their finite thermal conductivity in the present setup. With the finite thermal conductivity of the borosilicate glass the thermo-convective structures in the fluid induce thermal boundary layers in the windows and modify the stability properties [8, 14]. Redoing all the theory for our specific setup was beyond the scope of this thesis and hence comparisons will be made with the "standard" theory. However, the influence of the finite window conductivity will be observed at several occasions and commented on at least qualitatively.

Chapter 3

Results

In this chapter the present experimental results pertaining to the stability characteristics of the RBP system are presented. The first two sections are dedicated to the results obtained with uniformly heated and cooled bottom and top walls of the RBP channel and low Re of the Poiseuille flow. In this configuration transverse rolls ($R_\perp$) are observed beyond the theoretically predicted convective-absolute transition for $R_\perp$. The findings are confirmed by impulse response experiments.

The third section investigates thermo-convective patterns due to localized heating of the bottom plate, i.e. to a local patch of super-criticality in an otherwise stable channel. The resulting global modes are in most cases clearly of the steep kind. This is further confirmed by quantitative comparison of experimental saturation amplitudes with available numerical results.

3.1 Observation of transverse rolls

3.1.1 Detection of the appearance of the transverse rolls as a function of Re

The spontaneous appearance of $R_\perp$ without specific forcing in a channel with large transverse aspect ratio is only possible when the $R_\perp$ are absolutely unstable. This is because any facility perturbation that is *not* in the form of pure $R_\perp$ excites convectively unstable longitudinal rolls ($R_\parallel$), which are more unstable than the $R_\perp$ for all $Re > 0$. This is in fact the great difficulty of this experiment, as one has to "dive under" the region of instability of $R_\parallel$ without exciting them in order to study the convective absolute transition of $R_\perp$ (see the stability diagram 1.9). In other words, to avoid the appearance of the convectively most unstable transverse rolls the system needs to be excessively quiet (see e.g. [49]). This requirement can only be relaxed if the transverse aspect ratio is reduced as in the experiments of Trainoff [65] to the point of making $R_\perp$ more unstable than $R_\parallel$ at low Re.

Experimental procedure For the determination of the critical Rayleigh number $Ra_{c\perp}^{abs}$ for the convective-absolute transition of $R_\perp$, the Reynolds number is kept constant for the whole run and the Rayleigh number is increased in steps by increasing the temperature difference between the cooling and the heating baths. The maximum rate of increase is 2°C per hour ensures an adiabatic path through phase space and is sufficiently small to a avoid degassing of the hot water (bubble formation) while at the same time sufficiently quick to inhibit the $R_\parallel$ to grow to an observable amplitude from unavoidable minute upstream perturbations. The starting state is a completely settled system at the laboratory temperature. Then the temperature difference is increased typically to $Ra \approx 3000$ to 6000 (corresponding to an increase of temperature difference to 25°C for oil and 10°C for water). A typical experimental run lasts about twelve hours and is performed during the night to minimize environmental noise, vibrations in particular. After each slow temperature increase of typically 1°C the system is left to settle for 40 minutes, during which temperature and thermo-convective flow can reach equilibrium, before images of

the roll pattern are taken and the next temperature increase is started. This equilibration time corresponds to 12 and 20 thermal diffusion times (d^2/α) for the mineral oil and water, respectively. To further minimize the undesirable appearance of $R_{\parallel}$, steps were chosen whenever possible to avoid a settling period in the region where $R_{\perp}$ are unstable and $R_{\parallel}$ are still stable.

For the runs with oil, it was possible to use the diaphragm of the objective as the cutoff device (section 2.1.2) because of the large refractive index variation of this fluid with temperature. On the other hand, the smaller variations encountered with water required a single orientation cutoff device (here a razor blade) the position of which can be controlled more accurately. However, this allows the observation of only a single direction of thermo-convective rolls at a time.

Data processing First, a two-dimensional digital Fourier transform (2-D DFT) is taken of the entire Schlieren image. Taking the entire image acts as a low-pass filter to reduce the signal associated with any local subcritical onset of convection due to dust and to imperfections in the heating-cooling process. On each DFT of 320×320 points, the lowest wavenumber peak for $R_{\perp}$ was detected[1] and the integral over 5×5 amplitudes centered on this peak was taken to be *the* amplitude of the $R_{\perp}$. To extract the Ra of the convective-absolute transition (at constant Re) for $R_{\perp}$, which is a standard super-critical Hopf bifurcation, Landau's theory [18] is used. This theory holds that, after the bifurcation, the fundamental saturation amplitude squared is proportional to the parameter of super-criticality, i.e. in this case proportional to the difference between Rayleigh number and $Ra_{c\perp}^{abs}$ of the convective-absolute transition (3.1).

$$|A_0|^2_{sat} \propto (Ra - Ra_{c\perp}^{abs}) \tag{3.1}$$

The bifurcation is detected using a linear interpolation of the evolution of the amplitude squared of the fundamental mode for $R_{\perp}$ as a function of $(Ra - Ra_{c\perp}^{abs})$. A typical detection of $Ra_{c\perp}^{abs}$ is presented in figure 3.1 which is the experimental equivalent of the graph provided by Landau's theory in figure 1.11(b). This linear fitting of the amplitude squared on figure 3.1 poses two problems: first one has to decide up to which Ra one wants to fit the Landau equation which is only valid "near" the bifurcation. In most cases it was found that the quality of the linear fit starts to degrade beyond 1.5 to 2 times $Ra_{c\perp}^{abs}$. As previously stated in section 2.2.1, large Ra values are also overestimated and are therefore given a smaller weight in the fitting process. Second, the points near the bifurcation have to be associated either with the horizontal fit in figure 3.1 (theoretically the line of zero amplitude) or the fit of equation 3.1. In practice, this has been decided by an iterative process in which the goodness of the horizontal (constant) and the oblique (linear) least-square fits are optimized simultaneously.

[1] as shown in section 2.2.4 the Schlieren signature of the rising and falling fluid is different so that the lowest DFT wavenumber corresponds to the actual wavenumber of the roll.

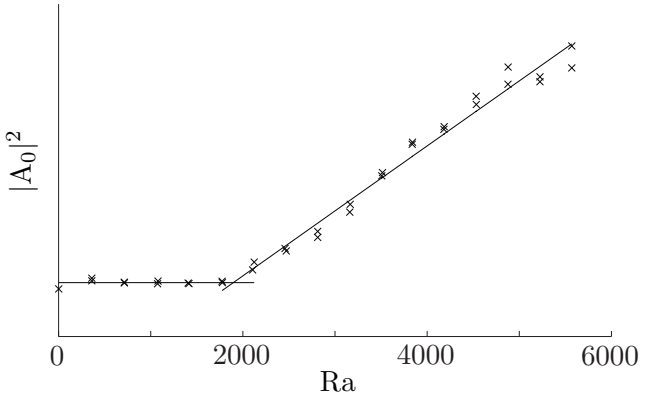

Figure 3.1: "×" Amplitude squared of the (saturated) $R_\perp$ at constant Re with "-" linear fit. The bifurcation value (i.e. the value of $Ra_{c\perp}^{abs}$) is deduced from the intersection of these two fits.

Results Several measurements for different Re numbers are collected in figures 3.2(a) and 3.2(b) for oil and water, respectively. The circles are the present experimental measurements corresponding to figure 1.9. In both graphs, the continuous line is a least-square quadratic fit of the data given by equations 3.2a and 3.2b :

$$Ra_{c\perp}^{abs}(\text{Oil}) = 7.197 \cdot 10^5 Re^2 + 2.010 \cdot 10^3 Re + 1.687 \cdot 10^3 \quad (3.2a)$$

$$Ra_{c\perp}^{abs}(\text{Water}) = 1.199 \cdot 10^2 Re^2 - 1.010 \cdot 10^1 Re + 1.640 \cdot 10^3 \quad (3.2b)$$

On figure 3.2, the dashed line is a 2-D DNS of Müller [41], given by equation 1.24. The dash-dotted line was numerically computed by Carrière and Monkewitz [9]. Finally, the two dotted curves on graph (b) are Trainoff's [65] experimental curves for the convective "△" and absolute "□" instability boundaries. The large difference between Trainoff's and all the other absolute instability boundaries is due to the very small transverse aspect ratio ($\mathcal{A}_\perp = 2$) used in his channel which produces a stabilizing effect. Details can be found in the study by Kato and Fujimura [29] and in the corresponding figure 1.12 in the introductory section.

Here it must be noted immediately that all the theoretical and DNS results assume perfectly heat conducting boundaries, while for the present experiments one has to take the thermal diffusivity difference between the fluid and the walls into account. The fitted critical Ra values in the experiment (see equation 3.2) for the no flow case are 1687 for the oil (Pr = 450) and 1640 for the water (Pr = 6.5). They should be compared with the values of $Ra_c(Re = 0) = 1631$ and $Ra_c(Re = 0) = 1587$ for oil and water, respectively, predicted by Hurle [22] for the thermal diffusivity ratio between fluid and our glass windows (figure 1.3). These values are seen to be inside the error bars of our experimental Ra. The thermal diffusivity ratio is of course also responsible for systematic errors at $Re > 0$, but here no theoretical results are available. Hence, only qualitative speculation is possible, for instance on the expected "slowing down" of the $R_\perp$ phase velocity.

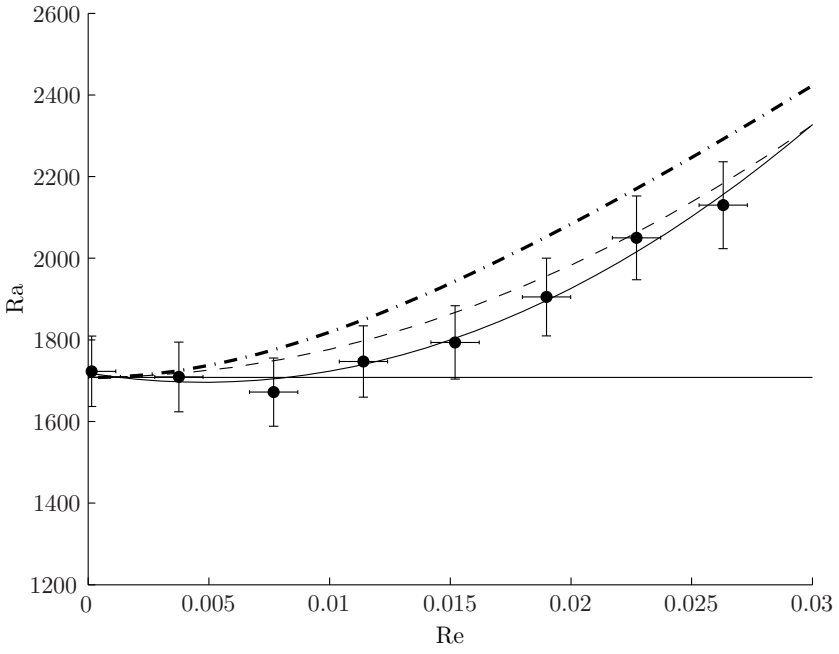

(a) Working fluid : Oil, Pr ≈ 450

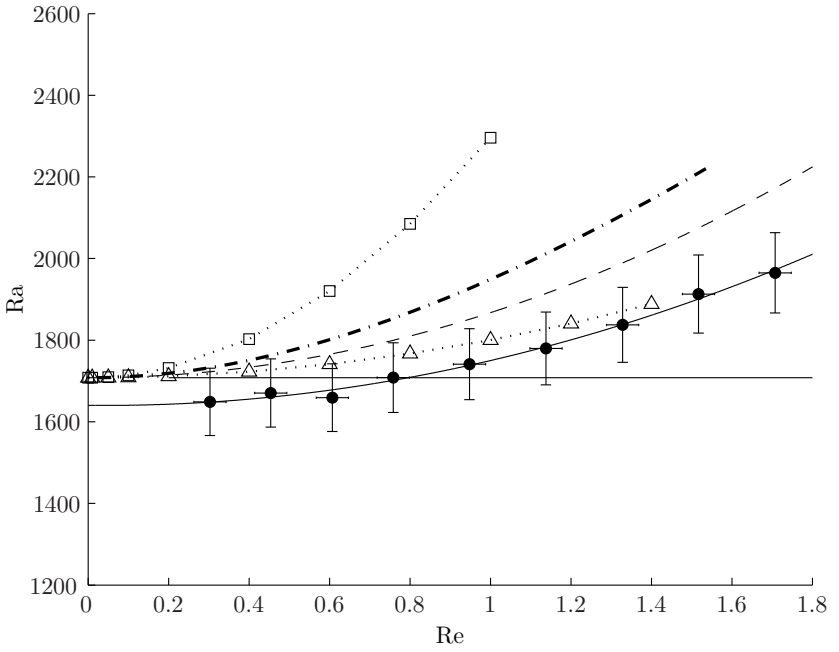

(b) Working fluid : Water, Pr ≈ 6.5

Figure 3.2: Stability boundaries in the Rayleigh-Reynolds number plane for two different Prandtl number fluids. The continuous lines are the least-square quadratic fits (3.2) of the present experimental onset of $R_\perp$ (○). The dash-dotted curve is the convective-absolute transition of $R_\perp$ evaluated numerically in [9], while the dashed line is from DNS [41]. The dotted lines marked by "△" and "□" are Trainoff's [65] measurements of $Ra_{c\perp}^{conv}$ and $Ra_{c\perp}^{abs}$, respectively, for water. The horizontal continuous line provides the reference Ra = 1708.

One can immediately notice the different quality of agreement between between DNS, theory and experiment in the two cases of figure 3.2. It is due to, among other things, the following experimental limitations: the refractive index variations of water are not large enough to provide the same accuracy of amplitude measurements as with oil. Another reason is the Prandtl number difference: a smaller value corresponds to the thermal boundary layer developing faster than the velocity boundary layer which, for a given level of noise in the system, promotes the earlier appearance of the most unstable $R_{\parallel}$ in water.

Despite all the limitations and systematic errors, the qualitative agreement between the present data and theoretical as well as numerically determined $Ra_{c\perp}^{abs}$ must be considered good.

3.1.2 Phase velocity of transverse rolls

Experimental procedure In this set of runs, the Rayleigh number was fixed once and for all at Ra = 4000. For each run, Re was fixed and the system was allowed to settle down for one hour. Then Schlieren pictures were taken periodically for at least one hour at a frequency of 0.1 to 5 Hz, depending on the roll velocity. The light cutoff used for these runs was a razor blade aligned in the transverse flow direction.

Data processing The phase velocity of $R_{\perp}$ is determined from the peak of the correlation of corresponding longitudinal pixel lines (perpendicular to the axes of $R_{\perp}$) on two consecutive images. Knowing the image acquisition frequency, the velocity is computed from the position of the correlation peak. This provides the $R_{\perp}$ phase velocity as a function of time. The observed time variation during a run at nominally constant conditions provides an indication of the experimental error.

Results The Results for water are presented in figure 3.3. In this figure, transverse rolls velocities have been non-dimensionalized by the corresponding mean Poiseuille flow velocity based on flow rate.

These results appear to contradict the experimental and numerical study by Ouazzani *et al.* [46], who observe for Ra = 4000 phase velocities of 1.8 (finite difference computation for a small aspect ratio $Æ_{\perp}$ of 1) and of 1.4 (experimental observation for a $Æ_{\perp}$ of 19) times the mean Poiseuille flow velocity for air, and the linear stability analysis by Nicolas *et al.* [44] who predicted a velocity of 1.46 times the mean Poiseuille flow velocity for water and a transverse aspect ratio of 5.4. Several factors may explain this difference: Firstly, neither the width nor the length of the present channel is infinite. Secondly, the horizontal heating and cooling boundaries are not perfect heat conductors, and therefore tend to slow down the rolls motion. This is because the rolls must drag along an associated temperature distribution in the wall. Based on the the thermal diffusivity ($\alpha = 6.57 \cdot 10^{-7} m^2/s$ for the borofloat) of our wall and the wavelength of $R_{\perp}$ ($\approx 2d$), the heat velocity in the wall is similar to the flow velocity at a Re of 0.013. For any larger value, the walls thermal diffusivity immediately slows down the rolls. This effect can be observed in figure 3.3 which shows a decrease in the phase velocity for larger Re. For small Re the phase veloctiy tends towards the values obtained by the other studies. Finally, the experiments done by Ouazzani *et al.* were conducted in a channel of smaller transverse aspect ratio with air (Pr $\approx$ 0.7) as the working fluid.

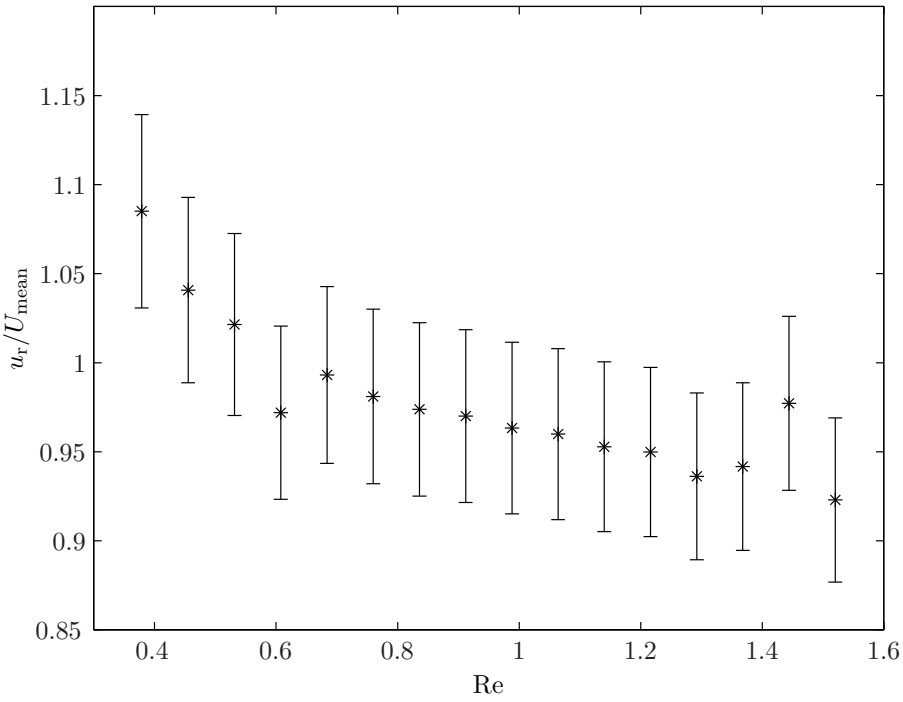

Figure 3.3: Ratio of the phase velocities u_r of the $R_\perp$ to the mean Poiseuille velocity U_{mean} for water ($Pr = 6.5$) at $Ra = 4000$.

3.2 Transition between convective to absolute regime

3.2.1 Impulse response observation

In the previous section it has been argued that the onset of $R_\perp$ in our experiment is observed at the convective-absolute instability boundary and *not* at the traditional (convective) instability boundary. To support this, the impulse response of the present system has been studied experimentally in the same spirit as the theoretical study of the impulse response by Carrière and Monkewitz [9]. As shown by these authors, the convective or absolute nature of the instability is directly determined by the propagation direction of the upstream edge of the wave packet.

Experimental procedure To determine the impulse response of the system, we first let the system equilibrate at the supercritical Rayleigh number chosen for the experiment. Then the channel is "cleaned" of thermo-convective rolls with a fast flow. As soon as all rolls are swept out of the test section (typically after 5 to 10 seconds), the flow rate is rapidly reduced to the desired Re in order to obtain a convection-free yet supercritical system and the system is allowed to settle during one or two minutes depending on the Pr value in order to reach a stationary state.

At this time, a laser pulse (15 – 30 seconds duration at 0.8 – 1.5 W) is sent onto a black 5 mm diameter target painted on the bottom surface of the channel (see section 2.1.3) to experimentally mimic a Dirac heat input. The evolution of the resulting wave packet is then captured with the same optical system (Schlieren) as before.

The reader is reminded that with water as working fluid the refractive index variations with temperature are too small for using the camera lens diaphragm as the cutoff device and a cutoff by razor blade had to be used with an orientation allowing only the observation of $R_\perp$. This limitation is obvious in figure 3.6(a) where the upper and lower parts of the wave packet (i.e. the longitudinally oriented parts) are not visible. Furthermore, at the larger Re values even the upstream edge of the wave packet becomes difficult to locate as seen in figure 3.8(a), here the image contrast has to be digitally enhanced and filtered in order to obtain reliable results.

Data processing The extraction of the velocities of the center and and of the upstream and downstream edges of the wave packet are carried out by hand because of the difficulties of writing a robust code. The contour of the wave packet is not well defined and an edge is clearly observable only when the roll next to the packet boundary is sufficiently developed, i.e. when the associated refractive index variation presents sufficient variations to produce a Schliere. Theoretically, the edge is defined as the contour on which the spatio-temporal growth rate is zero. This contour could in principle be approximated by a contour of (low) amplitude of the wave packet, but this would require a reliable determination of wave packet envelope, which proved to be unfeasible for the quality of the present Schlieren images. Therefore, the edge velocity had to be defined as the velocity of the outermost thermo-convective roll in the wave packet. Since new thermo-convective rolls at the edge of the wave packet only show up when they are sufficiently established to produce a Schliere, i.e. not continuously. This discontinuity is responsible for the "steps" of the observed edges positions in figures 3.5, 3.6, 3.7 and 3.8. Hence, the continuous parts of the graph of edge position versus time yield in fact the phase velocity of the outermost roll until a new external roll becomes observable. At this point the edge location defined in this fashion jumps and only the *envelope* of the edge position can be associated with the edge velocity of the wave packet.

Results The results of the impulse response experiments are compared in this section with the absolute/convective boundaries presented in the previous section and with the linear impulse response computations in an infinite channel by Carrière and Monkewitz [9]. A convective example of their computations is reproduced in figure 3.4. Asymmetries on the circular structures, especially close to the center of the pulse, can be observed: the parts of the essentially circular rolls forming the wave packet which are aligned with the flow, i.e. have locally the direction of $R_{\parallel}$, have a higher growth rate than the front and aft transverse parts of the circular rolls. This asymmetry is particularly visible in figure 3.7.

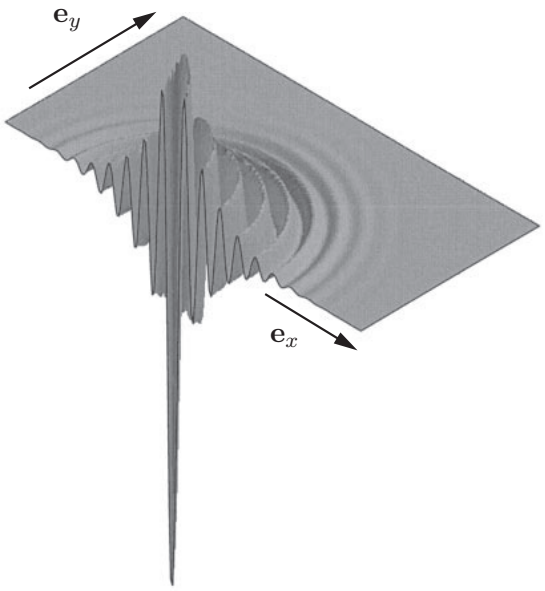

Figure 3.4: Computed linear impulse response by Carrière and Monkewitz [9] for a convectively unstable configuration. Note the lateral "ears" of the circular rolls.

An absolutely and a convectively unstable case is presented for both oil and water to illustrate the determination of wave packet edge velocities. In all four examples, the time of capture of the Schlieren image is indicated by the vertical arrow on the lower graph of edges position versus time. For consistency, all Schlieren pictures are shown with the same orientation: the Poiseuille flow is always from left to right in the direction $\mathbf{e}_x$ and $\mathbf{e}_y$ points up (see figure 1.6).

Impulse response in the absolutely unstable case (figures: 3.5 (oil) and 3.6 (water)) In the case of absolute instability, the edges of the wave packet travel in opposite directions. In a perfect channel of infinite aspect ratio, this wave packet would keep spreading endlessly in the horizontal plane $\mathbf{e}_x - \mathbf{e}_y$ somewhat like the wave pattern of a stone thrown into a lake. In a channel of finite transverse aspect ratio, even if it is very large as in the present setup, the lateral edges limit the spread of the wave packet. Furthermore, the imperfect thermal boundary conditions as well as pressure wave refections at these boundaries lead to the appearance of parasitic $R_{\parallel}$ which usually stop the spatial growth of the pulse even before its diameter reaches the full channel width. Furthermore, for conditions at which $R_{\perp}$ are absolutely unstable, transverse rolls appear eventually from the upstream end of the channel and "destroy" the wave packet generated by the laser pulse.

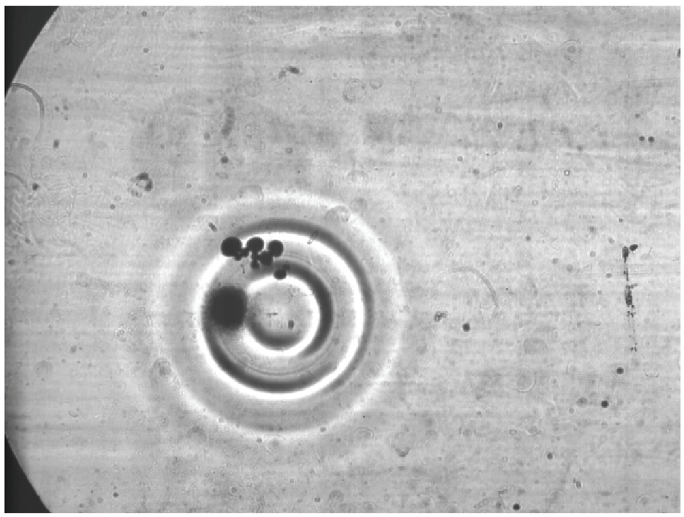

(a) Schlieren Image : the large black dot is the laser target of 5 mm diameter

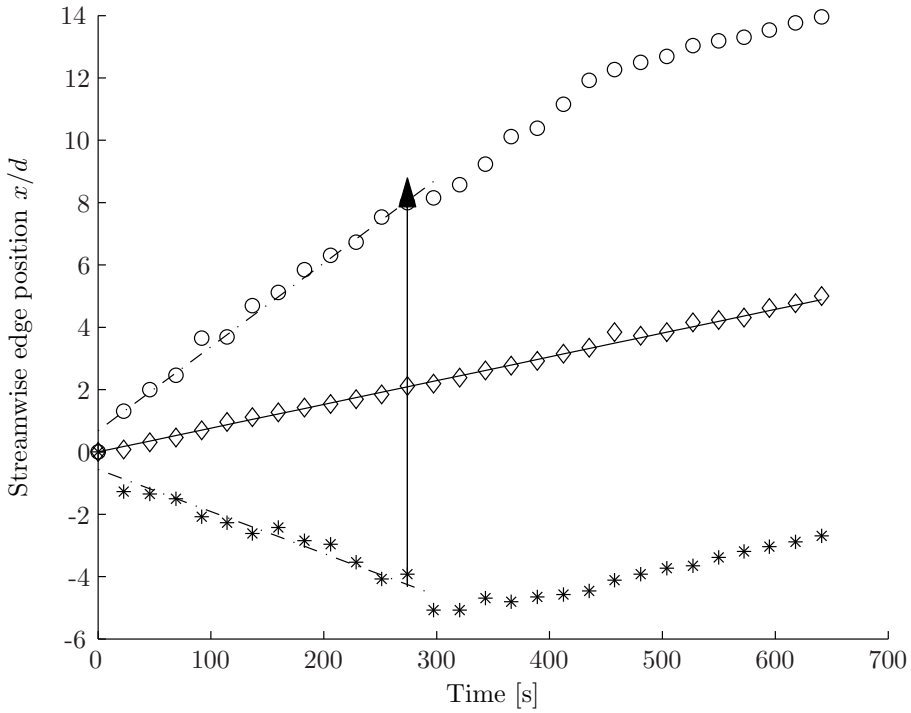

(b) Edge positions versus time

Figure 3.5: Impulse response in oil at Pr = 450, Re = 0.0064 and Ra = 1970. "$*$": position of upstream edge. "$\circ$": position of downstream edge. "$\diamond$": position of pulse center. The continuous line is the mean Poiseuille flow velocity while the dash-dotted lines are least-square linear fits based on edges velocities. The errors on these measurements is of the order of the symbol size. The arrow indicates the time at which the upper picture was captured.

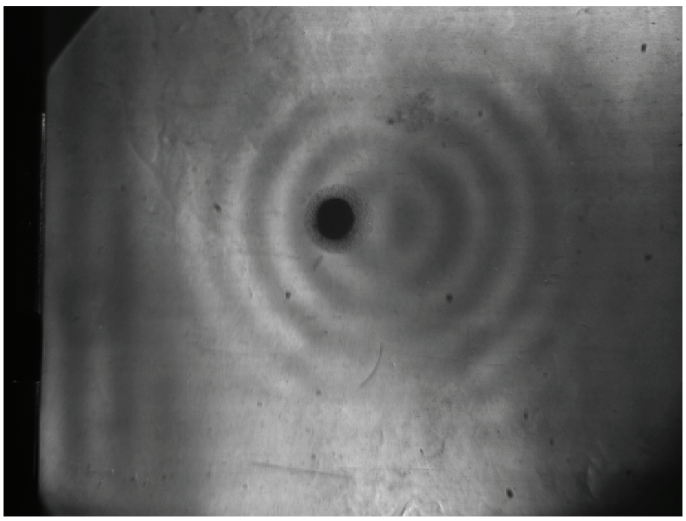

(a) Schlieren Image : the large black dot is the laser target of 5 mm diameter

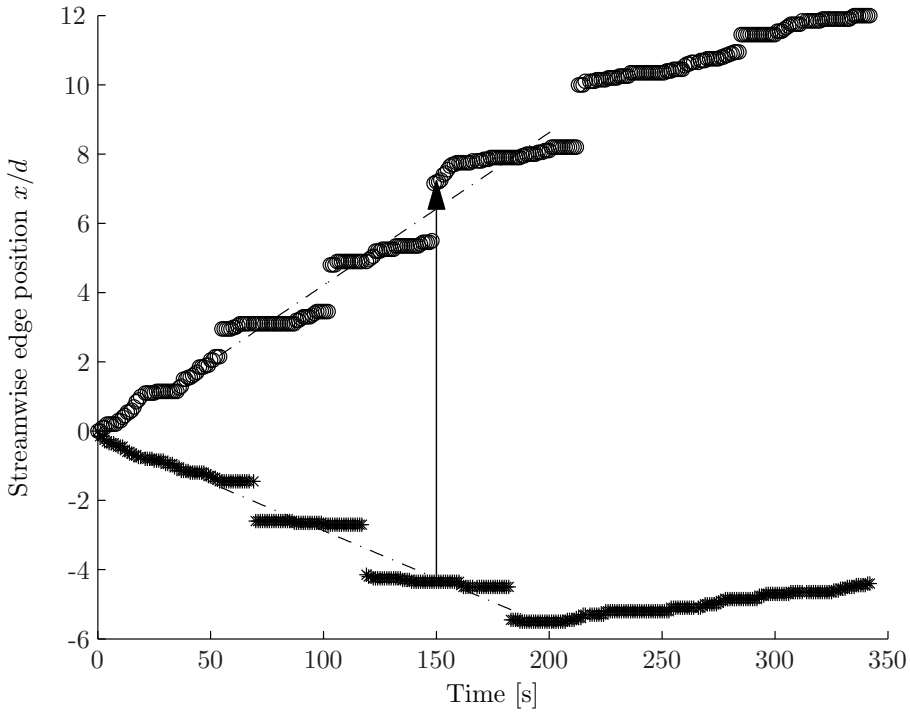

(b) Edge positions versus time

Figure 3.6: Impulse response in water at Pr = 6.5, Re = 0.22 and Ra = 2000. "$*$": position of upstream edge. "$\circ$": position of downstream edge. The dash-dotted lines are least-square linear fits based on edges velocities. The arrow indicates the time at which the upper picture was captured.

Impulse response in the convectively unstable case (figures: 3.7 (oil) and 3.8 (water)) Contrary to the previous case, both edges of the wave packet are seen to move in the flow direction. As the system is unstable, the downstream edge moves faster than the upstream edge, i.e. the wave packet grows while being swept downstream. This statement depends of course on the velocity of the reference frame. However, in the present case the relevant frame of reference for initial disturbances is clearly the frame attached to the facility.

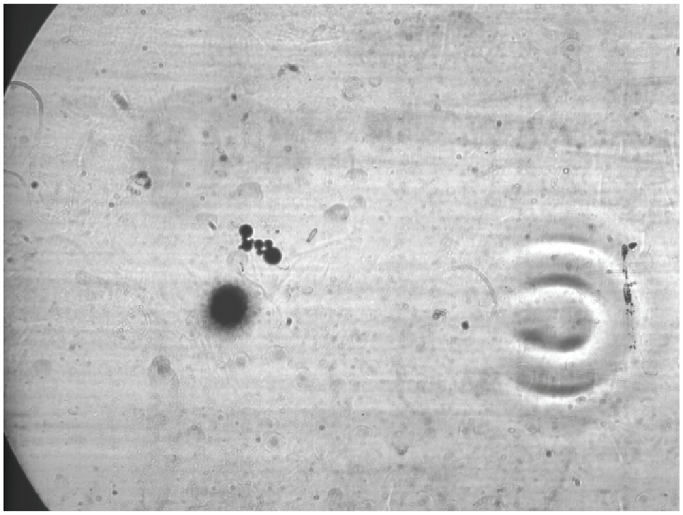

(a) Schlieren Image : the large black dot is the laser target of 5 mm diameter

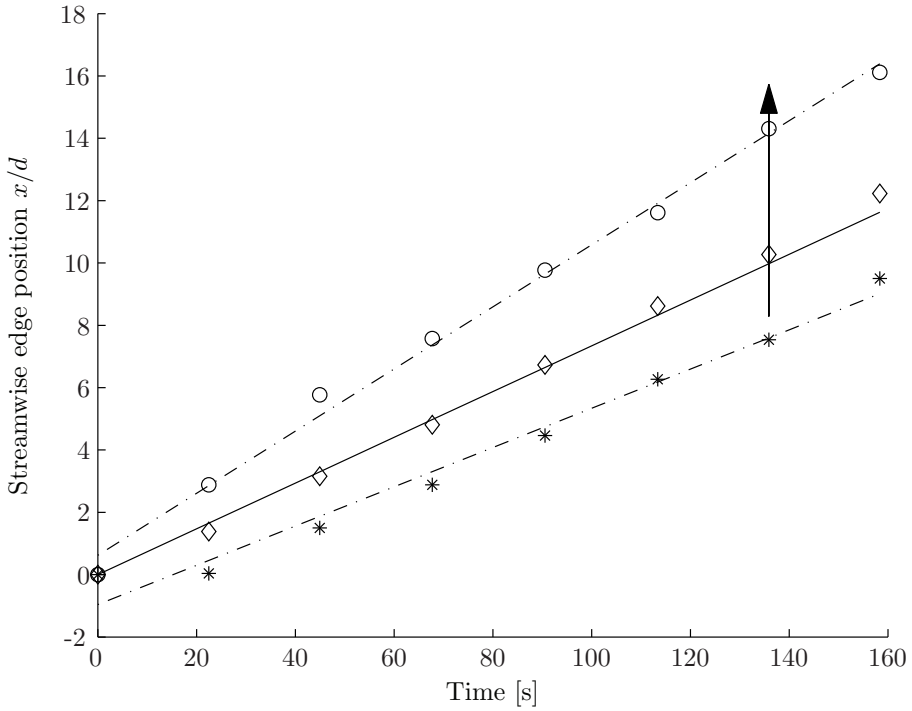

(b) Edge positions versus time

Figure 3.7: Impulse response in oil at Pr = 450, Re = 0.064 and Ra = 2060. "∗": position of upstream edge. "○": position of downstream edge. "◇": position of pulse center. The continuous line is the mean Poiseuille flow velocity while the dash-dotted lines are least-square linear fits based on edges velocities. The arrow indicates the time at which the upper picture was captured.

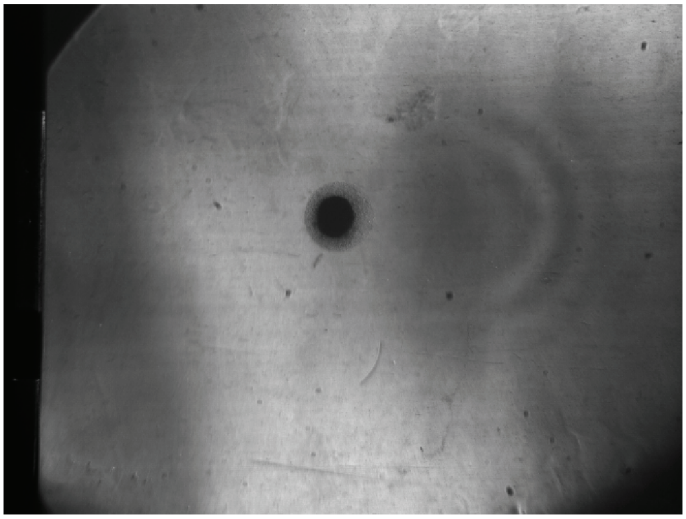

(a) Schlieren Image : the large black dot is the laser target of 5 mm diameter

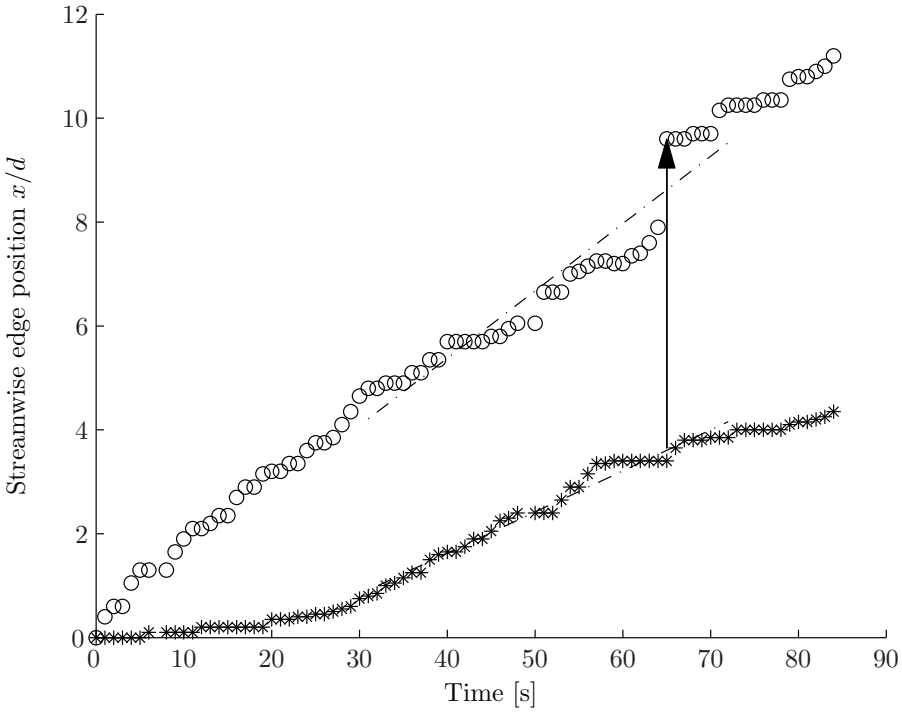

(b) Edge positions versus time

Figure 3.8: Impulse response in water at Pr = 6.5, Re = 2.84 and Ra = 2100. "∗": position of upstream edge. "∘": position of downstream edge. The dash-dotted lines are least-square linear fits based on edges velocities. The arrow indicates the time at which the upper picture was captured.

3.2.2 Transition between convective and absolute instability from the impulse response

Figures 3.9(a) (for oil) and 3.9(b) (for water) summarize the measurements of wave packet edge velocities as a function of Reynolds number Re. As soon as the upstream edge velocity (stars on the graphs) becomes positive, the entire impulse response moves in the flow direction: i.e. the perturbation is convectively unstable. Since Ra has been held as constant as possible at Ra $\approx$ 2000 for all measurements of edge velocities, it is possible to compare directly with the previous results of section 3.2: on both graphs the transition obtained from the measured amplitude of $R_\perp$ together with the Landau theory applied is indicated by a vertical arrow. Uncertainties are difficult to quantify, but the agreement between the two very different approaches must be considered as surprisingly good.

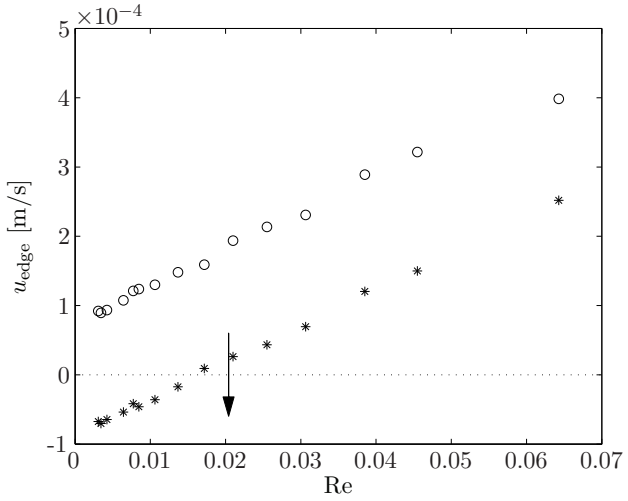

(a) Oil, (Pr $\approx$ 450)

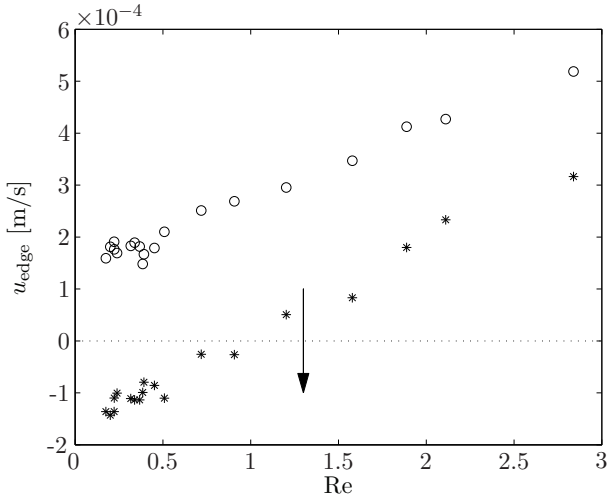

(b) Water, (Pr $\approx$ 6.5)

Figure 3.9: Edge velocities of the impulse response versus Re for Ra $\approx$ 2000. "$*$": upstream edge. "$\circ$": downstream edge.

3.3 The response to localized heating

The last phenomenon studied in the present facility is the response of the system to a single "island" of localized supercritical heating in the middle of a subcritical "sea". The hot islands are obtained by a hole in an additional thermal resistance added on the heating bath side of the lower channel wall, as described in section 2.1.4. Both shapes of hot spot (circle and swept rectangle) are studied for oil and water. The resulting temperature fields of the lower surface are documented in section 2.3.2.

The main goal of this experiment is to observe the thermo-convective pattern, i.e. the saturated global mode produced by these supercritical bumps, and to compare them with previous analytical and numerical work. Before presenting the results, both the experimental procedure and the data processing needed to extract the global mode amplitude from experiments are briefly described.

Experimental procedure The experimental procedure is the same as the one used for the detection of the transverse roll onset (section 3.1.1): a step-by-step Ra increase is imposed on the system while Re is kept constant and the system is left to settle the entire night *after* the final value for $\mathrm{Ra}_{\mathrm{max}}$ (maximal Rayleigh number inside the localized heating area) is reached. Only then a Schlieren image of the final stationary saturated global mode is recorded. $\mathrm{Ra}_{\mathrm{max}}$ is chosen to be the largest value allowing Ra_∞ (Rayleigh number far from the localized heating area) to stay in the subcritical range. Since Ra_c is an increasing function of Re, a large value for $\mathrm{Ra}_{\mathrm{max}}$ is necessary to compare global modes at constant Ra and different Re.

Hilbert transform To extract the envelope of the roll pattern from a standard Schlieren picture, the Hilbert transform $\mathcal{H}\{s(t)\}$ has been used which, for any continuous signal $s(t)$, is defined by:

$$\mathcal{H}\{s(t)\} \equiv h(t) * s(t) = \int_{-\infty}^{\infty} h(\tau)s(t-\tau)d\tau, \tag{3.3}$$

where $h(t) \equiv 1/(\pi t)$ is the impulse response of the Hilbert filter. This transform shifts the negative frequencies by $+\pi/2$ while the positive frequencies are shifted by $-\pi/2$. This transforms for instance a cosine into a sine. More generally, the Hilbert transform allows to construct a complex signal with $s(t)$ as real part and the Hilbert transform of $s(t)$ as imaginary part. Hence, the absolute value of this complex signal

$$E(t) = \sqrt{s(t)^2 + \mathcal{H}\{s(t)\}^2} \tag{3.4}$$

represents the envelope of the signal $s(t)$. As an example, the envelope of a signal generated by multiplication of a cosine and a sine with different frequencies (an "idealized" wave packet) is perfectly detected as shown in figure 3.10.

This transform is easily implemented on a discrete signal (in one or two dimensions) using a "fast" algorithm described for instance by Oppenheim and Schafer (1989) [45].

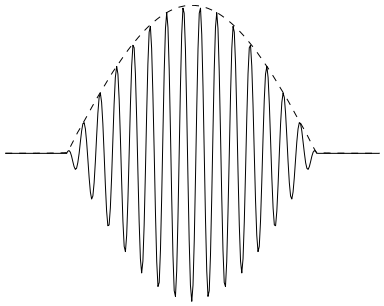

Figure 3.10: Example of the envelope (dashed line) detection of a compound sine/cosine signal (continuous line) using the Hilbert transform.

Data processing To be able to extract the amplitude of the localized convection pattern several operations have to be applied to the source pictures:

1. Offset subtraction: an image of the system in a stable state without thermo-convective pattern is subtracted from every picture in order to remove the mosquito net image as well as (stationary) optical defects that disturb the spectrum if left in.

2. Image filtering I: the images are low-pass filtered to eliminate the high frequency noise induced by the offset operation.

3. Image filtering II: every image is passed through a band pass filter in order to keep only the wavenumber of the rolls. This operation is necessary to be able to detect the amplitude via the Hilbert transform. Practically, we used a dual band pass filter to keep also the first harmonic of the roll wavenumber as it allows better envelope detection, but it is given a smaller weight. Both filters (low and band-pass) are standard 2-D windows-based finite impulse response filters.

4. Hilbert transform: Unfortunately a 2-D Hilbert transform does not provide good detection because of the nearly transverse rolls in the wave packet which provide only a single half period in the span-wise direction. Therefore, only a 1-D version is applied in the flow direction $\mathbf{e}_x$ on the filtered signal.

5. The resulting amplitude is smoothed with 2-D spline interpolation.

6. To relate the global mode envelopes to the local stability characteristics, the absolutely unstable area is computed from the flow parameters and the measured shape of the surface temperature distribution (see section 2.3.2 and especially figure 2.33). The area of local absolute instability is displayed with a different color (dark gray) on figure 3.13. Its surface is seen to decrease and moves in the downstream direction as Re increases.

As the Schlieren system has to be realigned after every modification of the channel, it is not possible to reposition every optical component exactly in the same position. Specifically, a very small modification on the cutoff device position can produce large differences of contrast on the observed picture.

Therefore, the amplitude of the Schlieren cannot be directly compared between different cases and the following results are presented without numerical scale for the amplitude. However, the scale is the same for all pictures in a given figure. For an attempt to quantify the global mode amplitude from Schlieren images, see section 3.3.2.

Results Figure 3.11 presents roll patterns in oil (Pr = 450) at increasing flow rates and fixed Rayleigh number for both shapes of the hot spot. In the absence of flow (i.e. Re = 0), one can see in figures 3.11(a) and 3.11(d) the pure Rayleigh–Bénard flow; the rolls are arranged as expected with their "ends" preferentially at right angles to the boundary of the localized heated area. The application of a Poiseuille flow (flowing from left to right on every image of figure 3.11) orients the rolls essentially perpendicular to the flow direction, i.e. produces a packet of $R_\perp$. As the critical Rayleigh Ra_c is an increasing function of Re (figure 3.2), the upstream edge of the roll packet is progressively pushed towards the center of the hot spot where the temperature is the highest as Re is increased.

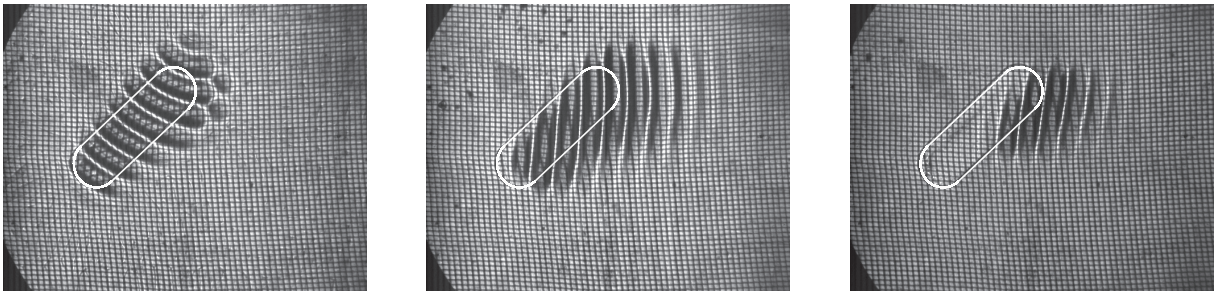

(a) Re = 0.000 Ra_{max} = 2682 (b) Re = 0.012 Ra_{max} = 2696 (c) Re = 0.021 Ra_{max} = 2656

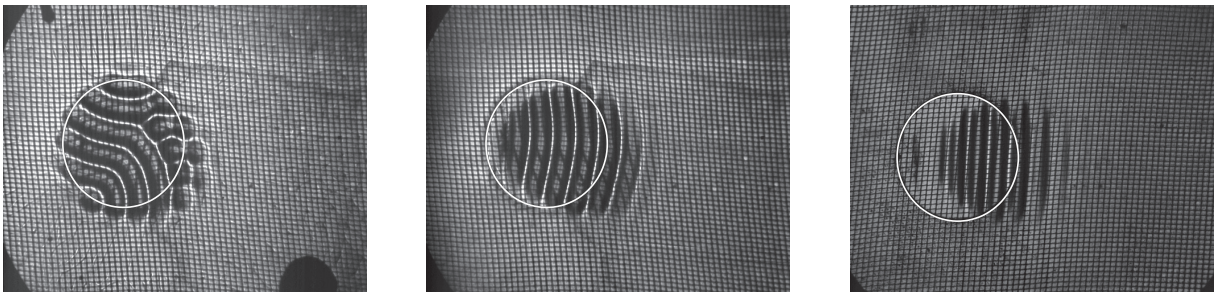

(d) Re = 0.000 Ra_{max} = 2615 (e) Re = 0.009 Ra_{max} = 2542 (f) Re = 0.021 Ra_{max} = 2653

Figure 3.11: Roll structure for oil as the working fluid. The white shape represents the cutout of the added heat resistance (see section 2.3.2).

Figure 3.12 presents results for the same channel configuration but with water (Pr = 6.5) as working fluid. The cutoff difference explains the difference between the Re = 0 images 3.11(a) and 3.12(a) in oil and water which are expected to be substantially similar. The large amplitude pattern observed in 3.12(d) on the other hand is produced by a cellular convection pattern.

Taking into account the different cutoff devices, the water results are sensibly similar to those in oil: as soon as Re > 0, the observed thermo-convective roll pattern consists essentially of $R_\perp$. However, as said before, a direct comparison of amplitudes in oil and water is not possible. Hence, a different arbitrary scale is used for the amplitude contours (red lines), but again it is the same for all sub-images in figure 3.12.

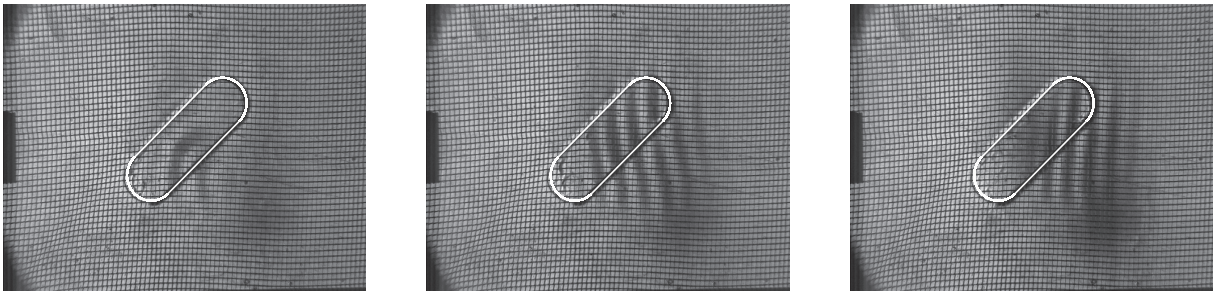

(a) Re = 0.00 Ra_{max} = 3066 (b) Re = 1.1 Ra_{max} = 3389 (c) Re = 1.9 Ra_{max} = 3156

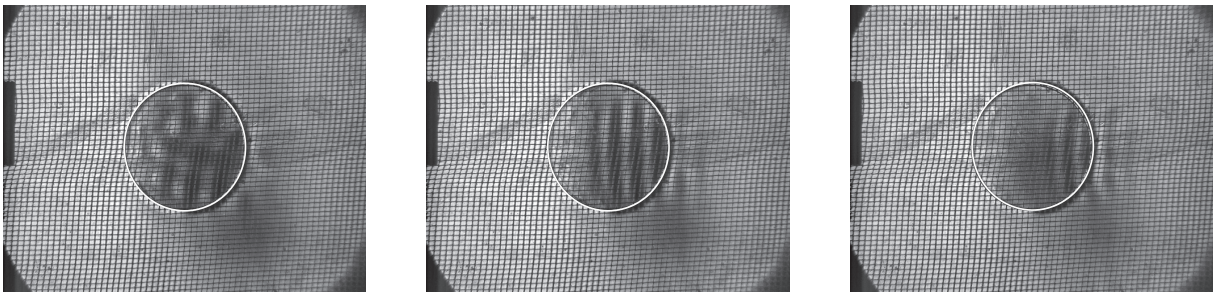

(d) Re = 0.15 Ra_{max} = 3344 (e) Re = 1.2 Ra_{max} = 3191 (f) Re = 2.3 Ra_{max} = 3456

Figure 3.12: Envelope contours and roll structure for water as the working fluid. The white shape represents the cutout of the added heat resistance (see section 2.3.2). Note that the razor blade cutoff only shows $R_\perp$.

3.3.1 Further analysis of global mode amplitudes

To further interpret the roll patterns due to localized heating, the envelope shapes extracted from the measurements by the Hilbert transform technique have been replotted in 3-D in figure 3.13 for oil as working fluid. The dark gray coloring of the envelope indicates where the underlying base state is locally absolutely unstable (see section 2.3.2 for the determination of the absolutely unstable area). The light gray, on the other hand, indicates local convective instability or stability (the two are not distinguished as this would have required the stability analysis of the present setup with realistic boundary conditions). To make the connection to the previous images, the observed roll pattern is replotted underneath the envelopes, with the hole in the thermal resistance plate indicated by the green curve.

Looking first at the two images 3.13(a) and 3.13(d) for Re = 0, the global mode is seen to have the same shape as the hot spot and to be centered on it, i.e. on its locally absolutely unstable region, as expected from the symmetries of the no-flow base state (rotation symmetry for the circular hot spot and reflection symmetries for the rectangle). As soon as the flow is turned on, these symmetries are broken as seen in figures (b),(c), (e) and (f), and the rolls within the global modes are (approximately) aligned in the transverse direction. This is entirely consistent with the facts that a localized global mode is generally associated with an area of local absolute instability and that only $R_\perp$ become absolutely unstable in the RBP system. Specifically, figure 3.13 is in qualitative agreement with the theoretical analysis and the numerical simulations of global modes by Martinand *et al.* [36, 37] (see also section 1.6.3), even though the experimental shape of the hot spot does not exactly correspond to the one used in the numerical simulations.

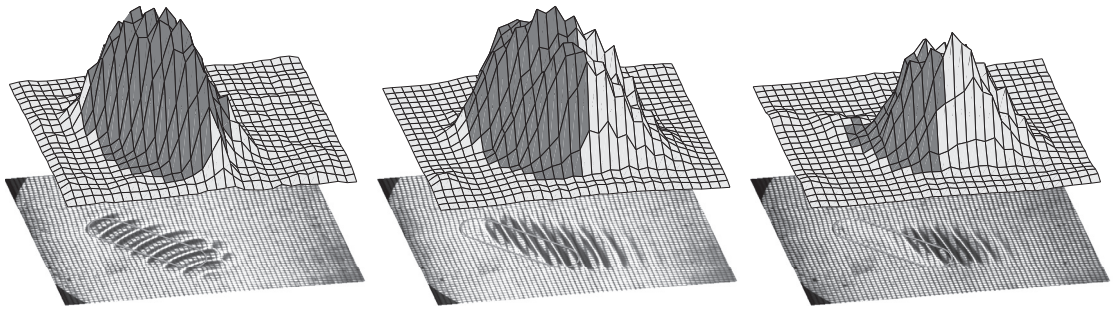

(a) Re = 0.000 Ra_{max} = 2682 (b) Re = 0.015 Ra_{max} = 2635 (c) Re = 0.021 Ra_{max} = 2656

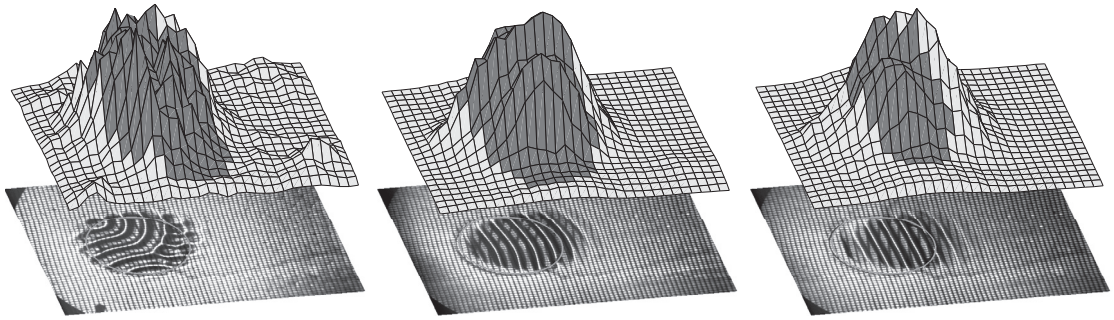

(d) Re = 0.000 Ra_{max} = 2615 (e) Re = 0.009 Ra_{max} = 2542 (f) Re = 0.018 Ra_{max} = 2666

Figure 3.13: Envelope of global modes for Pr = 450, Ra ≈ 2600 and different Re with absolutely unstable area in dark gray. Images are flipped compared to figure 3.11 in order to have the same orientation as the global modes computed by Martinand *et al.* and presented in section 1.6.3.

Of particular interest is the question whether the saturated global modes in the RBP system are the 2-D equivalent of "steep" or "soft" nonlinear global modes first analyzed by Pier *et al.* [53] and reproduced in figure 3.14.

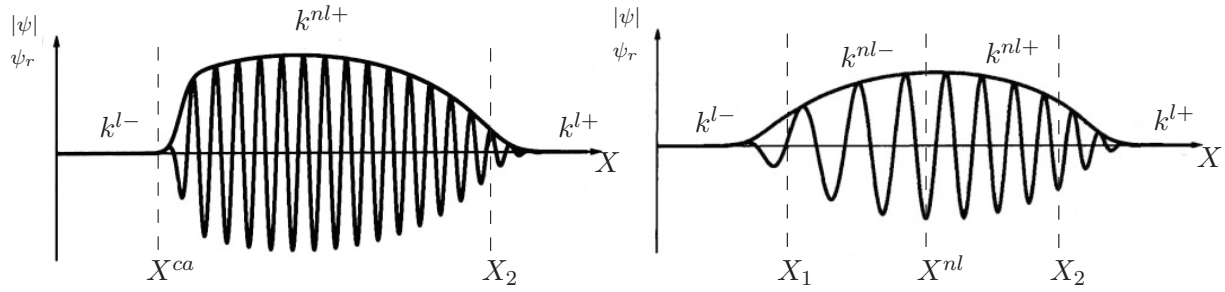

(a) Steep global mode (b) Soft global mode

Figure 3.14: One dimensional steep (a) and soft (b) global mode from DNS of the complex Ginzburg–Landau equation by Pier *et al.* [53]. Each graph shows the envelope $|\psi|$ and the real part ψ_r of the CGL solution as functions of the downstream distance X. $k^{l\pm}$ and $k^{nl\pm}$ are corresponding to the analytically computed linear and nonlinear spatial branches in the complex k-plane, (see details in [53])

Since this question is difficult to answer based on the 3-D plots of figure 3.13, the case of figure 3.13(b) for Pr = 450, Re = 0.015 and Ra = 2635 is reprocessed in figure 3.15. First the original image has been filtered in the streamwise direction at twice the roll wavenumber (neglecting the asymmetry between the rising and falling edges in the Schlieren pictures) in order to increase the signal to noise ratio. Then a streamwise slice approximately through the center of the wave packet was selected. The envelope of this slice, containing about ten rolls, was then computed by Hilbert transform and the result, after a final spline smoothing, is displayed in figure 3.15. This processing clearly brings out the well defined rolls in the front part of the wave packet, but downstream of the wave packet, where rolls are less developed, the Schlieren produces different amplifications for the rising and the falling portions that could not be eliminated without degrading the front part. Again, no amplitude scale is provided in figure 3.15 as no direct calibration of the Schlieren system was possible.

The streamwise slice through the saturated global mode in figure 3.15 clearly shows a difference between the steeper front and the flatter back which is a characteristic of the steep global mode constructed by Pier *et al.* [53] (case (a) in figure 3.14). Note that the difference in length of the wave packets in figures 3.15 and 3.14 is not relevant to the comparison as it only reflects a difference in the length of the absolutely unstable region. What is significant, however, is the location of the steep front: it is seen to be "attached" to the upstream convective-absolute transition (this can also be observed in all the cases of figure 3.13 with Re > 0). This location is consistent with the location of the nonlinear front in the steep global mode of Pier. Hence, all the evidence supports the hypothesis that the saturated global modes of figure 3.13 are indeed 2-D equivalents of steep 1-D global modes. A firm conclusion will however have to wait for the extension of nonlinear global mode theory to 2-D.

3.3.2 Attempt to quantify the Schlieren measurements

To obtain quantitative or at least semi-quantitative results from a Schlieren image, the measured intensity must be converted to refractive index variations ($\propto$ temperature variations). Because of the numerous difficulties associated with both a fully experimental calibration of the Schlieren

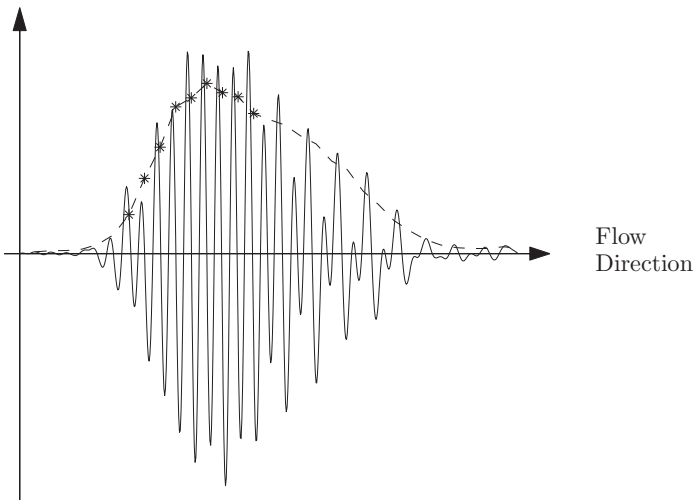

Figure 3.15: Streamwise amplitude profile corresponding to a slice of image 3.13(b). The continuous line is the filtered roll signal (and its first harmonic to improve the envelope detection); − − −: wave packet amplitude with stars indicating locally absolute instability.

system and the complete theoretical determination of the transfer function, the experimental optical system has been simulated using geometrical optics. The output position and direction of regularly spaced beams passing through a 2-D RB cell was calculated with the code Comsol using the thermo-physical properties of oil. The output rays were then sent through a two-lens optical system corresponding to the present experimental setup (focal lengths of 450 and 24 mm respectively). The cutoff aperture diameter was chosen to obtain the same total intensity ratios I/I_0 for both experimental and synthetic signals at different Re. The considered experimental signal is a single pixel line in the Poiseuille flow direction ($\mathbf{e}_x$) for a very small Re (a small flow is necessary to observe $R_\perp$corresponding to 2-D cells).

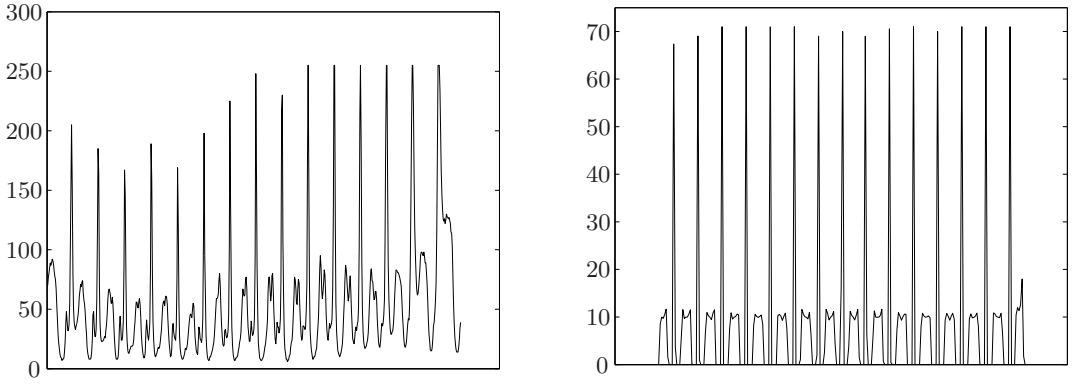

(a) Experimental signal (b) Synthetic signal

Figure 3.16: Experimental and computed Schlieren signal for oil (Pr = 450) with Ra = 2300. The scale of the experimental signal is pixel brightness ranging from 0 to 255 (note that the high bright peaks on the right have saturated the CCD). The scale of the synthetic signal is arbitrary. Several 2-D cells are simulated to partially compensate for the errors due to the finite number of simulated beams (5000).

The results are presented in figure 3.16. The amount of light blocked by the pinhole in the

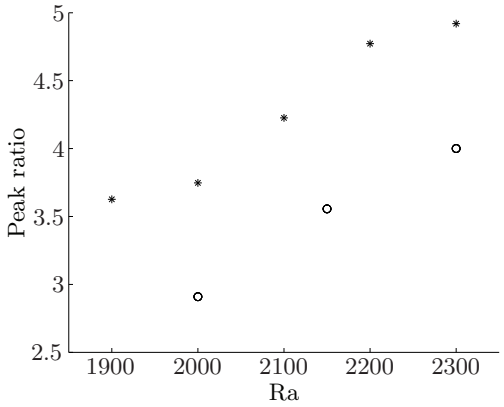

Figure 3.17: Amplitude ratio between large and small peaks for both experimental "∘" and synthetic "∗" Schlieren signals versus Ra.

experiment is unknown, however, the ratio between the large and the small peaks of each signal is independent of the absolute brightness. This ratio is shown in figure 3.17 as a function of Ra for oil. It is seen that the experimental ratio is comparable to the computed ratio - the former is about 30% smaller but shows the same trend with Ra. This difference has numerous potential sources: besides pixel saturation, experimental misalignment and RB cell and synthetic Schlieren simulation errors. Furthermore the simulated optical system is simplified: in the experimental system, the cutoff device is positioned inside the camera lens system, while the simulated system is only modeled with a cutoff between two lenses. Finally, the CCD captor of our camera presents a fill factor[2] of only 75%, the other 25% are non-measuring surface (i.e. blind surface: space around every light sensitive pixel area needed for connectivity) which leads to additional errors in our comparison.

[2]The fill factor of a CCD is the ratio between the surface covered by effectively detected light to the surface covered by incident light.

Chapter 4

Conclusion

The stability of Rayleigh–Bénard–Poiseuille flow has been studied in a large transverse aspect ratio channel fitted with lateral soft walls. Several analytical and numerical results have been experimentally confirmed. Although the comparisons of these results are mostly qualitative because of measurement limitations, all the expected phenomenon have been effectively observed in the system.

Transverse rolls were observed as predicted by the theory for small Reynolds numbers as we were able to dive under the longitudinal rolls state. The onset of transverse rolls is observed for smaller $\mathrm{Ra}_{\mathrm{c}\perp}^{\mathrm{abs}}$ than predicted by the linear theory mainly due to the finite thermal diffusivity of the horizontal walls. However this instability boundary shape is nicely fitted with a quadratic polynomial in a coherent way with the previous analytical and numerical results by Carrière and Monkewitz [9] and Müller *et al.* [41]. Unfortunately the longitudinal rolls being more unstable in the area just above the minimal convection limit, only the absolutely unstable transverse rolls can be observed.

A more detailed investigation of the phase velocity of the transverse rolls should be considered in to order confirm the influence of the thermal diffusivity of the walls. Smaller Re flows or different window materials could provide an experimental confirmation in the absence of computational results taking this aspect into account.

The transition between absolute and convective instability was measured using the impulse response of the system, specifically its response to a short duration laser pulse. This transition was determined by the sign change of the velocity of the upstream edge of the impulse response. The comparison with the onset of the absolutely unstable transverse rolls $\mathrm{Ra}_{\mathrm{c}\perp}^{\mathrm{abs}}$ exhibits good quantitative agreements for both oil and water.

The rest of this PhD work was the observation of the global mode produced by a single localized heating area applied to the lower surface of the channel and its comparison with one dimensional nonlinear global modes computed by Pier *et al.* [53] using DNS of the complex Ginzburg–Landau equation.

The observed two dimensional mode appears under the form of a wave packet composed essentially of transverse rolls. This roll orientation is consistent with the absolute instability generally encountered in localized global modes. The amplitudes extracted from the experimental results are in qualitative agreement with the numerical and theoretical computations of global modes by Martinand *et al.* [36, 37]. A quantitative comparison would require the calibration of the Schlieren system.

The streamwise section of the wave packet is found to correspond to the 1-D "steep" kind of computed global mode (Pier *et al.* [53]), composed of a steeper front that is attached to the spatial location of the convective-absolute transition. However, a two-dimensional extension of the nonlinear global mode theory is not available to confirm this result.

Nomenclature

Roman letters

a	Non-directional wavenumber $a \equiv \sqrt{a_x^2 + a_y^2}$	m^{-1}
a_c	Critical Wavenumber (Nondimensionalization is done with gap height d)	
a_x	Wavenumber in the $\mathbf{e}_x$ direction	m^{-1}
a_y	Wavenumber in the $\mathbf{e}_y$ direction	m^{-1}
$Æ_\parallel$	Longitudinal aspect ratio L/d	
$Æ_\perp$	Transversal aspect ratio l/d	
c_p	Specific heat at constant pressure	$\mathrm{kJ} \cdot \mathrm{kg}^{-1} \cdot \mathrm{K}^{-1}$
c_v	Specific heat at constant volume	$\mathrm{kJ} \cdot \mathrm{kg}^{-1} \cdot \mathrm{K}^{-1}$
d	Gap height of the channel	m
g	Gravity with $\boldsymbol{g} = -g\mathbf{e}_z$	$\mathrm{m} \cdot \mathrm{s}^{-2}$
L	Gap length of the channel	m
l	Gap width of the channel	m
n	Refractive index	
Q	Measured flow rate through the channel	$\mathrm{m}^3 \cdot \mathrm{s}^{-1}$
q_z	Vertical heat flux in the channel per surface unit	$\mathrm{J} \cdot \mathrm{m}^{-2}$
$\mathrm{R}_\parallel$	Longitudinal rolls	
$\mathrm{R}_\perp$	Transversal rolls	
ΔT	Temperature difference between the lower (hot) and the upper (cold) wall	°C
T	Temperature	°C
T_cold	Cold bath temperature	°C
T_hot	Hot bath temperature	°C
T_mean	Mean baths temperature	°C
T_u	Channel upper surface temperature	°C
T_b	Channel bottom surface temperature	°C
$\boldsymbol{u}$	Velocity field in the channel $\boldsymbol{u} = (u, v, w)$	$\mathrm{m} \cdot \mathrm{s}^{-1}$
U_max	Maximal pure Poiseuille velocity in the channel	$\mathrm{m} \cdot \mathrm{s}^{-1}$

U_{mean}	Mean pure Poiseuille velocity in the channel	$\mathrm{m}\cdot\mathrm{s}^{-1}$
u_{r}	Phase velocity of the transverse rolls	$\mathrm{m}\cdot\mathrm{s}^{-1}$

Greek letters

α	Thermal diffusivity $\alpha\equiv \kappa/(\rho c_{\mathrm{p}})$	$\mathrm{m}^2\cdot\mathrm{s}^{-1}$
β	Volumetric thermal expansion coefficient	K^{-1}
κ	Thermal conductivity	$\mathrm{W}\cdot\mathrm{m}^{-1}\cdot\mathrm{K}^{-1}$
κ_{w}	Thermal conductivity of the channel windows	$\mathrm{W}\cdot\mathrm{m}^{-1}\cdot\mathrm{K}^{-1}$
κ_{f}	Thermal conductivity of the working fluid	$\mathrm{W}\cdot\mathrm{m}^{-1}\cdot\mathrm{K}^{-1}$
λ	Linear thermal expansion coefficient	K^{-1}
μ	Dynamic viscosity	$\mathrm{Pa}\cdot\mathrm{s}$
ν	Kinematic viscosity $\nu \equiv \mu/\rho$	$\mathrm{m}^2\cdot\mathrm{s}^{-1}$
ρ	Density	$\mathrm{kg}\cdot\mathrm{m}^{-3}$
ζ	Landau constant	

Dimensionless Numbers

Bi	Biot number
Gr	Grashof number
Nu	Nusselt number
Pe	Péclet number
Pr	Prandtl number
Ra	Rayleigh number
$\mathrm{Ra}_{\mathrm{c}\perp}^{\mathrm{conv}}$	Convective critical Rayleigh number
$\mathrm{Ra}_{\mathrm{c}\perp}^{\mathrm{abs}}$	Absolute critical Rayleigh number
$\mathrm{Ra}_{\perp}$	Rayleigh number for transverse rolls
$\mathrm{Ra}_{\parallel}$	Rayleigh number for longitudinal rolls
Ra_{∞}	Rayleigh number far from the localized heated area
$\mathrm{Ra}_{\mathrm{max}}$	Maximal Rayleigh number into the localized heated area
Ra_{c}	Critical Rayleigh number
$\mathrm{Ra}_{\mathrm{c}\perp}$	Critical Rayleigh number for the transverse rolls
$\mathrm{Ra}_{\mathrm{c}\parallel}$	Critical Rayleigh number for the longitudinal rolls
Re	Reynolds number
Re_{c}	Critical Reynolds number

Mathematical conventions

*	Complex conjugate
i	Imaginary unit
$\|.\|$	Norm
$\mathbf{e}_x$	Streamwise direction
$\mathbf{e}_y$	Spanwise direction
$\mathbf{e}_z$	Vertical direction

Bibliography

[1] *Handbook of Chemistry & Physics*. CRC Press, 2007.

[2] H. Bénard. Les tourbillons cellulaires dans une nappe liquide. *Revue Générale des Sciences Pures et Appliquées*, 11:1261–1271, 1900.

[3] H. Bénard. Les tourbillons cellulaires dans une nappe liquide transportant de la chaleur en régime permanent. *Annales de Chimie et de Physique*, 23:62–144, 1901.

[4] H. Bénard and D. Avsec. Travaux récent sur les tourbillons en bandes: Applications à l'astrophysique et à la météorologie. *Journal de Physique et Le Radium*, 9:468–500, 1938.

[5] C.M. Bender and S.A. Orszag. *Advanced Mathematical Methods for Scientists and Engineers*. McGraw-Hill, 1978.

[6] M.J. Block. Surface tension as the cause of Bénard cells and surface deformation in a liquid. *Nature*, 178:650–651, 1956.

[7] J. Boussinesq. *Théorie analytique de la chaleur, mise en harmonie avec la thermodynamique et la théorie mécanique de la lumière, Tome II: Refroidissement et échauffement par rayonnement. Conductibilité. Courant de convection.* Gauthier-Villars, 1903.

[8] F.H. Busse and N. Riahi. Nonlinear convection in a layer with nearly insulating boundaries. *Journal of Fluid Mechanics*, 86:243–256, 1978.

[9] P. Carrière and P.A. Monkewitz. Convective versus absolute instability in mixed rayleigh-bnard-poiseuille convection. *Journal of Fluid Mechanics*, 384:243–262, 1999.

[10] P. Carrière and P.A. Monkewitz. Transverse-roll global modes in a Rayleigh–Bénard–Poiseuille system with streamwise variable heating. *European Journal of Mechanics - B/Fluids*, 20:751–770, 2001.

[11] P. Carrière, P.A. Monkewitz, and D. Martinand. Envelope equations for the Rayleigh–Bénard–Poiseuille system. part 1. spatially homogeneous case. *Journal of Fluid Mechanics*, 502:153–174, 2004.

[12] S. Chandrasekhar. *Hydrodynamic and Hydromagnetic Stability*. Oxford University Press, 1961.

[13] S. Chandrasekhar. *Liquid Crystals*. Cambridge University Press, 1977.

[14] C.J. Chapman, S. Childress, and M.R.E. Proctor. Long wavelength thermal convection between non-conducting boundaries. *Earth and Planetary Science Letters*, 51:362–369, 1980.

[15] R.M. Clever and F.H. Busse. Instabilities of longitudinal rolls in the presence of Poiseuille flow. *Journal of Fluid Mechanics*, 229:517–529, 1991.

[16] S.H. Davis. Convection in a box: linear theory. *Journal of Fluid Mechanics*, 30:465–478, 1967.

[17] R.P. Davis-Jones. Thermal convection in an infinite channel with no-slipe sidewalls. *Journal of Fluid Mechanics*, 44:695–704, 1970.

[18] P.G. Drazin and W.H. Reid. *Hydrodynamic Stability*. Cambridge University Press, 2004.

[19] K.S. Gage and W.H. Reid. The stability of thermally stratified plane Poiseuille flow. *Journal of Fluid Mechanics*, 33 part I:21–32, 1968.

[20] A.V. Getling and O. Brausch. Cellular flow patterns and their evolutionary scenarios in three-dimensional Rayleigh–Bénard convection. *Physical Review E*, 67, 2003.

[21] P. Huerre and P.A. Monkewitz. Absolute and convective instabilities in free shear layers. *Journal of Fluid Mechanics*, 159:151–168, 1985.

[22] D.T.J. Hurle, E. Jakeman, and E.R. Pike. On the solution of the Benard problem with boundaries of finite conductivity. *Royal Society of London Proceedings Series A*, 296:469–475, 1967.

[23] P. Idrac. Sur les courants de convection atmosphérique et leur rapport avec le vol à voile et la formation des bandes nuageuses. *Comptes Rendus de l'Académie des Sciences*, 171:42–44, 1921.

[24] N.K. Ingle and T.J. Mountziaris. The onset of transverse recirculations during flow of gases in horizontal ducts with differentially heated lower walls. *Journal of Fluid Mechanics*, 277:249–269, 1994.

[25] M. Jammer. *The conceptual development of quantum mechanics*. McGraw-Hill, 1966.

[26] H. Jeffreys. The stability of a layer of fluid heated from below. *Philosophical Magazine*, 1926.

[27] H. Jeffreys. Some cases of instability in fluid motion. *Proceedings of the Royal Society of London, Serie A*, pages 195–208, 1928.

[28] K.F. Jensen, E.O. Einset, and D.I. Fotiadis. Flow phenomena in chemical vapor deposition of thin films. *Annual Review of Fluid Mechanics*, 23:197–233, 1991.

[29] Y. Kato and K. Fujimura. Prediction of pattern selection due to an interaction between longitudinal rolls and transverse modes in a flow through a rectangular channel heated from below. *Physical Review E*, 62:601–611, 2000.

[30] E.L. Koschmieder. *Bénard Cells and Taylor Vorticies*. Cambridge University Press, 1993.

[31] E.L. Koschmieder and S.G. Pallas. Heat transfer through a shallow, horizontal convecting fluid layer. *International Journal of Heat and Mass Transfer*, 17:991–1002, 1974.

[32] A.R. Low. On the criterion for stability of a layer of viscous fluid heated from below. *Proceedings of the Royal Society of London. Series A, Containing Papers of a Mathematical and Physical Character*, 125(796):180–195, 1929.

[33] J.-M. Luijkx. *Influence de la présence de parois latérales sur l'apparition de la convection libre, forcée et mixte*. PhD thesis, University of Mons (Belgium), 1983.

[34] J.-M. Luijkx, J.K. Platten, and J.C. Legros. On the existence of thermoconvective rolls, transverse to a superimposed mean Poiseuille flow. *International Journal of Heat and Mass Transfer*, 24:1287–1291, 1981.

[35] D. Martinand. *Détermination analytique des modes globaux tridimensionnels en écoulement de convection mixte du type Rayleigh–Bénard–Poiseuille*. PhD thesis, Université Lyon I Claude Bernard, 2003.

[36] D. Martinand, P. Carrière, and P.A. Monkewitz. Envelope equations for the Rayleigh-Bénard-Poiseuille system. part 2. linear global modes in the case of two-dimensional non-uniform heating. *Journal of Fluid Mechanics*, 502:175–197, 2004.

[37] D. Martinand, P. Carrière, and P.A. Monkewitz. Three-dimensional global instability modes associated with a localized hot spot in Rayleigh-Bénard-Poiseuille convection. *Journal of Fluid Mechanics*, 551:275–301, 2006.

[38] H.W. Müller. *Thermische Konvection in horizontaler Scherströmung*. PhD thesis, Universitt des Saarlandes, Sarrebrück (Germany), 1990.

[39] H.W. Müller, M. Lücke, and M. Kamps. Convective patterns in horizontal flow. *Europhysics Letters*, 10:451–+, 1989.

[40] H.W. Müller, M. Tveitereid, and S. Trainoff. Rayleigh–Bénard problem with imposed weak through-flow: Two coupled Ginzburg–Landau equations. *Physical Review E*, 48:263–272, 1993.

[41] Müller, H.W. and Lücke, M. and Kamps, M. Transversal convection patterns in horizontal shear flow. *Physical Review A*, 45, 1992.

[42] A.C. Newell and J.A. Whitehead. Finite bandwidth, finite amplitude convection. *Journal of Fluid Mechanics*, 38:279–303, 1969.

[43] X. Nicolas. Revue bibliographique sur les écoulements de Poiseuille–Rayleigh–Bénard. *International Journal of Thermal Sciences*, 41:961–1016, 2002.

[44] X. Nicolas, J.M. Luijkx, and J.K. Platten. Linear stability of mixed convection flows in horizontal rectangular channels of finite transversal extension heated from below. *International Journal of Heat and Mass Transfer*, 43:589–610, 2000.

[45] A.V. Oppenheim and R.W. Schafer. *Discrete-Time Signal Processing*. Prentice-Hall International, Inc, 1989.

[46] M.T. Ouazzani, J.P. Caltagirone, G. Meyer, and A. Mojtabi. Etude numérique et expérimentale de la convetion mixte entre deux plans horizontaux á température différentes. *International Journal of Heat and Mass Transfer*, 32:261–269, 1989.

[47] M.T. Ouazzani, J.K. Platten, and A. Mojtabi. Etude expérimentale de la convection mixte entre deux plans horizontaux à températures différentes. II. *International journal of heat and mass transfer*, 33(7):1417–1427, JUL 1990.

[48] M.T. Ouazzani, J.K. Platten, and A. Mojtabi. Intermittent patterns in mixed convection. *Applied Scientific Research*, 51(4):677–685, DEC 1993.

[49] M.T. Ouazzani, J.K. Platten, H.W. Müller, and M. Lücke. Etude de la convection mixte entre deux plans horizontaux à temperatures différentes - III. *International Journal of Heat and Mass Transfer*, 38:875–886, 1995.

[50] E. Palm. On the tendency towards hexagonal cells in steady convection. *Journal of Fluid Mechanics*, 8:183–192, 1960.

[51] J. R. A. Pearson. On convection cells induced by surface tension. *Journal of Fluid Mechanics*, 4:489–500, 1958.

[52] B. Pier and P. Huerre. Fully nonlinear global modes in spatially developing media. *Journal of Physics D: Applied Physics*, 97:206–222, 1996.

[53] B. Pier, P. Huerre, and J.-M. Chomaz. Bifurcation to fully nonlinear synchronized structures in slowly varying media. *Physica D Nonlinear Phenomena*, 148:49–96, 2001.

[54] B. Pier, P. Huerre, J-M Chomaz, and A. Couairon. Steep nonlinear global modes in spatially developing media. *Physics of Fluids*, 10:2433–2435, 1998.

[55] J.K. Platten and M. Lefebvre. A preliminary experimental investigation of the stability of flows with an imposed temperature gradient. *Physica*, 51:330–332, 1971.

[56] L. Rayleigh. On convection currents in a horizontal layer of fluid when the higher temperature is on the under side. *Philosophical Magazine*, 32:529–546, 1916.

[57] H. Schlichting and K. Gersten. *Boundary Layer Theory*. Springer, 2003.

[58] R.J. Schmidt and S.W. Milverton. On the instability of a fluid when heated from below. *Proceedings of the Royal Society of London. Series A*, 152:586–594, 1935.

[59] L.A. Segel. Distant side-walls cause slow amplitude modulation of cellular convection. *Journal of Fluid Mechanics*, 38:203–224, 1969.

[60] G.S. Settles. *Schlieren and Shadowgraph Techniques*. Springer, 2001.

[61] P.L. Silveston. W"armedurchgang in waagerechten Fl"ussigkeitsschichten. *Forschung im Ingenieurwesen*, 24:59–69, 1958.

[62] H.B. Squire. On the stability for three-dimensional disturbances of viscous fluid flow between parallel walls. *Proceedings of the Royal Society of London. Series A*, 142:621–628, 1933.

[63] K.C. Stengel, D.S. Oliver, and J.R. Booker. Onset of convection in a variable-viscosity fluid. *Journal of Fluid Mechanics*, 120:411–431, 1982.

[64] J. K. Sveen. An introduction to matpiv v.1.6.1. Eprint no. 2, **ISSN** 0809-4403, Dept. of Mathematics, University of Oslo, 2004. http://www.math.uio.no/~jks/matpiv.

[65] S.P. Trainoff. *Rayleigh-Bénard Convection in the Presence of a Weak Lateral Flow*. PhD thesis, University of California, Santa Barbara, 1997.

[66] I. C. Walton. The effect of a shear flow on convection in a layer heated non-uniformly from below. *Journal of Fluid Mechanics*, 154:303–319, May 1985.

[67] F.M. White. *Viscous Fluid Flow*. McGraw-Hill, 1974.

Curriculum Vitæ

Contact Information

Emeric Grandjean	October 17$^{\text{th}}$, 1978	
Avenue de la Harpe 10	*Mobile:*	+41(0)78 823 9942
1007 Lausanne	*Work:*	+41(0)21 693 5312
Switzerland	*E-mail:*	emeric.grandjean@a3.epfl.ch

Education

2003 – 2008 PhD. at the Ecole Polytechnique Fédérale de Lausanne (EPFL), Switzerland, Laboratory of Fluid Mechanics (LMF).
Title: "Experimental Investigation into Localized Instabilities of Mixed Rayleigh–Bénard–Poiseuille Convection"
Advisor: Prof. P.A. Monkewitz

1997 – 2003 MSc. at the Ecole Polytechnique Fédérale de Lausanne (EPFL), Switzerland, Laboratory of Fluid Mechanics (LMF).
Title: "Molecular Dynamics Simulation of the Flow Inside a Rotating Cylinder"
Advisors: Prof. P.A. Monkewitz and Dr. N. Borhani

Scientific Contributions

Grandjean E., Borhani N. and Monkewitz P.A., "Experimental Investigation of Pattern Instabilities in the Rayleigh-Bénard-Poiseuille System". *6th EUROMECH Fluid Mechanics Conference*, KTH Mechanics, Stockholm, Sweden, June 26–30, 2006.

Grandjean E., Borhani N. and Monkewitz P.A., "Experimental Study of Instability Patterns in a Non-uniformly Heated Rayleigh–Bénard–Poiseuille Cell". *60th Annual Meeting of the APS Divison of Fluid Dynamics*, Salt Lake City, Utah, USA, November 18–20, 2007,